NOTA: anche questa pagina bianca fa parte del blocco di pagine della tesi

NOTA: tagliare il blocco di pagine della tesi (stampata fronte-retro) lungo le due linee qui tracciate prima di effettuare la rilegatura

POLYTECHNIC INSTITUTE OF TURIN

Master's degree course in Environmental and Land Engineering

Master Thesis

Coarse Woody Debris carbon stock estimation at the seashore of San Rossore regional park, in Italy, Tuscany (PI); through geomatics tools

Supervisors

Prof. Carlo CAMPOREALE

Ph.D. Elena BELCORE

Candidate

Elisa CACCAMO

July 2023

Summary

In the context of Climate Change, among the requirements for global emission reports is demanded to estimate the quantity of carbon in dead organic matter as a significant carbon reservoir in natural environments.

The expression Large Woody Debris, LWD, or Coarse Woody Debris, CWD, refers to dead trees and the remains of branches lying on the ground, usually in forests or river wetlands. Until now, few studies have focused on the coastal marine ecosystem and wood accumulation at the seashore due to storm surges and on their role in being a significant carbon stock and influencing the carbon stock in soil, undergoing decomposition and humidification processes.
The biological relevance of such wood deposits is also related to their contribution to characterising the geo-eco-morphodynamics of the coastal natural environment. They act as modulators of sediment transport across the backshore and as control and base structures for developing and maintaining dunes. This case study analyses the CWD carbon stock and the beach dynamics in two targeted areas along the backshore in San Rossore Regional Park, Italy, Tuscany (PI).

Table of contents

1. Introduction and contextualisation

Evidence of human interference with the planet's climatic balance emerged in the last century. The so-called climatic changes have consequences on ecosystems and natural resources worldwide.
The most evident change in climate of the last 100 years is the increase in the global average temperature. After some debate in the past decades, it is now primarily acknown the correlation between this temperature raising and anthropogenic greenhouse gas emissions, among which CO_2 causes the greenhouse gas effect.

Consequently, the United Nations Framework Convention on Climate Change (UNFCCC) and the Kyoto Protocol established Intergovernmental Panel on Climate Change (IPCC) Guidelines for National Greenhouse Gas Inventories. Nations signing are encouraged to quantify carbon fluxes and pools in natural environments.
Climate change mitigation and adaptation measures need to be taken. Both strategies are necessary to compensate for the continuous emissions of greenhouse gases potentially leading to irreversible effects on the climate.

The attention is on eco-engineering strategies that preserve natural terrestrial carbon sinks, for example, the vegetation, the ocean, and the soil. This approach tends to compensate for the loss of natural CO_2 sinks and reservoirs that results, in around 12÷20% human-caused greenhouse gas emissions (Le Quéré et al. 2009)

The world's forests are mainly considered (IPCC 2003) both living trees and dead wood. However, measurements of dead wood in forests are not as established in National Forest Inventories (NFI) as measurements of alive trees (Tomppo et al. 2010; Woodall et al. 2009). In fact, among the requirements for global emission reports is demanded to estimate the quantity of carbon in the form of dead organic matter as a significant carbon reservoir in the natural environment.
Even less attention is paid to coastal areas and vegetated marine ecosystems that are instead of great interest both for their role in CO_2

emissions mitigation but equally important in adaptation to sea-level rise, increasing wave energy, sea storms, and coastal erosion (Duarte et al. 2013).
Related to the capacity of the marine ecosystem to act as carbon stock, but even less mentioned than marine vegetated areas, is the role of Large Woody Debris, LWD, deposits on the seashore.

The expression Large Woody Debris or Coarse Woody Debris generally refers to dead trees and the remains of branches lying on the ground, usually in forests or river wetlands. Until now, few studies have focused on CWD accumulation on the seashore in coastal areas due to storm surges and on their essential contribution in characterising the geo-eco-morphodynamics of such natural environments. In addition to being a carbon stock, LWD acts as a modulator of sediment delivery across the backshore and as a control and base structure of the development and maintenance of sand dunes.

Traditional methods to study CWD have relied on field data collection, which can be expensive, time-consuming, and limited by accessibility to sampling sites. However, with advancements in high-speed computing of large amounts of data and remote sensing, automated solutions have been developed to identify and measure CWD structures and components using aerial and satellite imagery.

This work aims at developing a case study on a CWD deposit at the seashore in San Rossore Regional Park, in Italy, Tuscany (PI). Integrating data collected during an in-site survey, remotely sensed aerial data, and using geomatics techniques and software, the goal is to indirectly estimate the volume of the wood accumulation in two large areas and consequently to retrieve an evaluation of the carbon stock associated.

2. Literature review

2.1. Atmospheric carbon increase

In recent years, awareness for what concerns the environmental impact associated with Climate Change is rising. Temperature increase, heatwaves, wildfires, more frequent and intense extreme events such as floods or drought, rising sea levels, and melting glaciers are some of the most relevant impacts of climate change. This expression refers to a modification in the state of the climate that can be identified, for example, through statistical tests, by changes in the mean and/or in the variability of its properties, which persists for an extended period, typically decades or longer. All these changes affect ecosystems, cities, animals and humans' health, food, and water resources.

One of the most relevant impacts of Climate Change is global warming. Such expression refers to the increase in the mean global temperature, related to the increment of greenhouse gasses (GHGs) emissions due to anthropogenic activities. These gases are water vapour, carbon dioxide, methane, nitrous oxide, ozone, fluorinated gases, and others. Most are naturally present in the atmosphere in such concentrations to prevent significant thermal variations between day and night. Without considering the presence of these gases, the global energy balance Earth's surface temperature result, of about 18° C, would drop to around -15°C. The different behaviours of GHGs address this phenomenon to the electromagnetic radiation considered in the energy balance. An exhaustive scheme of the global energy balance is shown in Figure 1.

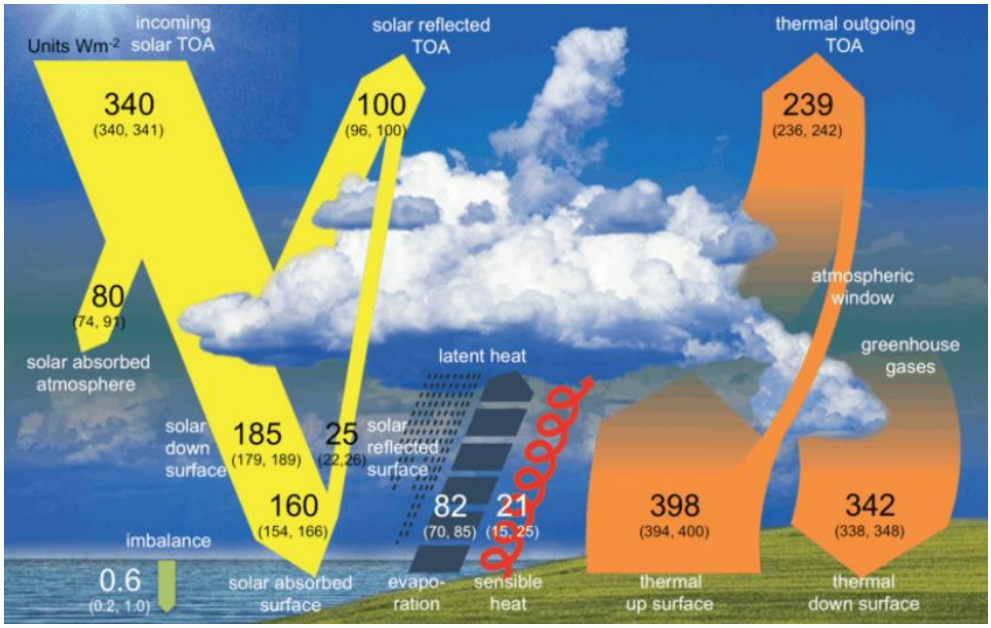

Figure 1. Earth's global mean energy balance (Wild et al. 2013).

While GHGs are transparent to wavelengths corresponding to the visible range, they are opaque to lethal ultraviolet and infrared radiation. To better analyse the interaction between gas and radiation is shown the absorption spectrum for each gas is in Figure 2.

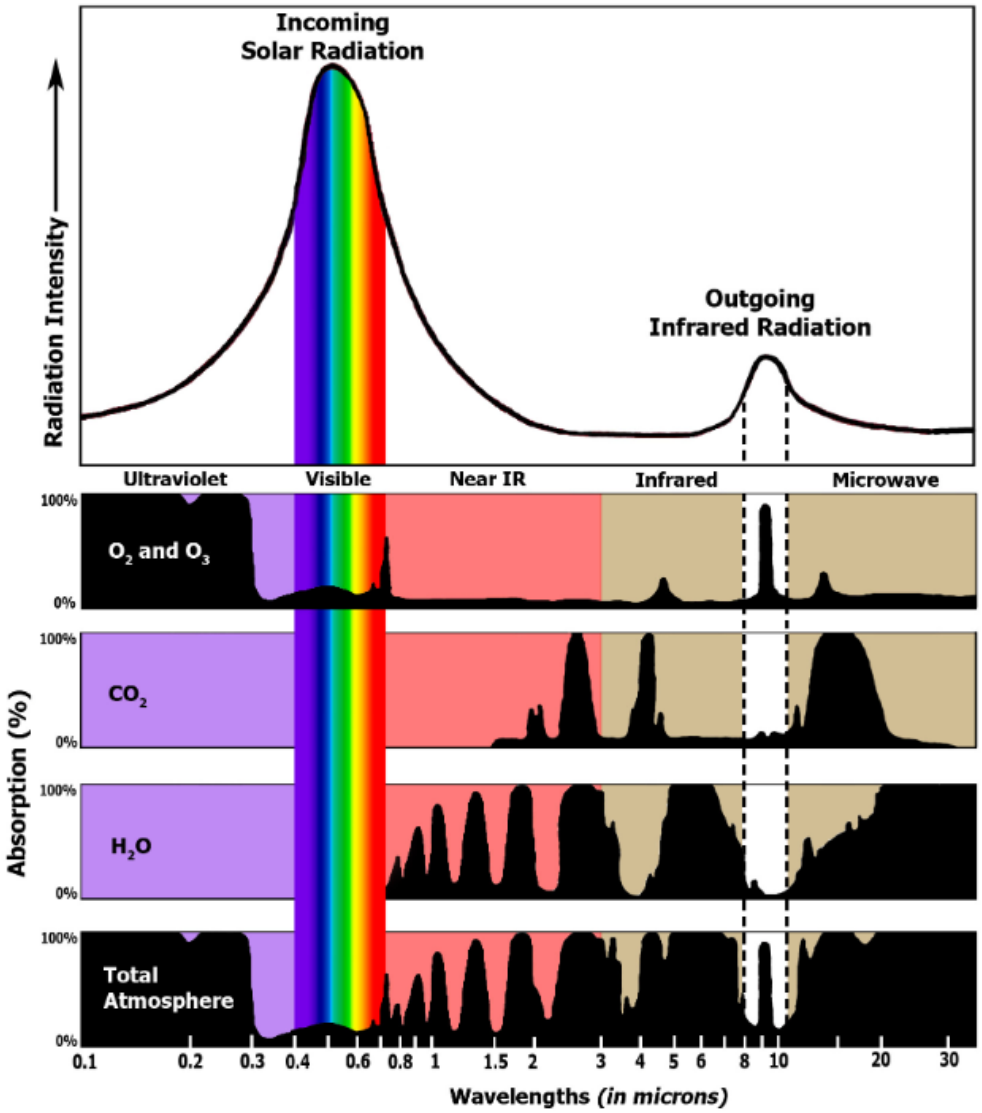

Figure 2. The absorption spectrum of different GHGs and the atmosphere (Højgård-Olsen 2020).

Among GHGs, is CO_2, which strongly absorbs energy with a wavelength falling in the infrared radiation region of the spectrum of around 15µm, corresponding to the thermal energy re-emitted by the Earth's surface. This way, solar radiation with a much shorter wavelength penetrates the

atmosphere. According to Wien's law, the Earth's surface absorbs sunlight and re-emits part of the absorbed energy as infrared radiation.

$$\lambda_{max} = \frac{2897}{T} \text{ [1]}$$

Considering the Earth's temperature, T, around 300 K, is obtained a wavelength, $\lambda_{max,}$ in the thermal infrared range.

Therefore, this energy remains trapped in the atmosphere due to the overall absorbing characteristics of GHGs. It corresponds to an atmospheric temperature increase and, consequently, to a rise in the Earth's temperature.

This warming is visible from the global mean temperature time series illustrated in Figure 3.

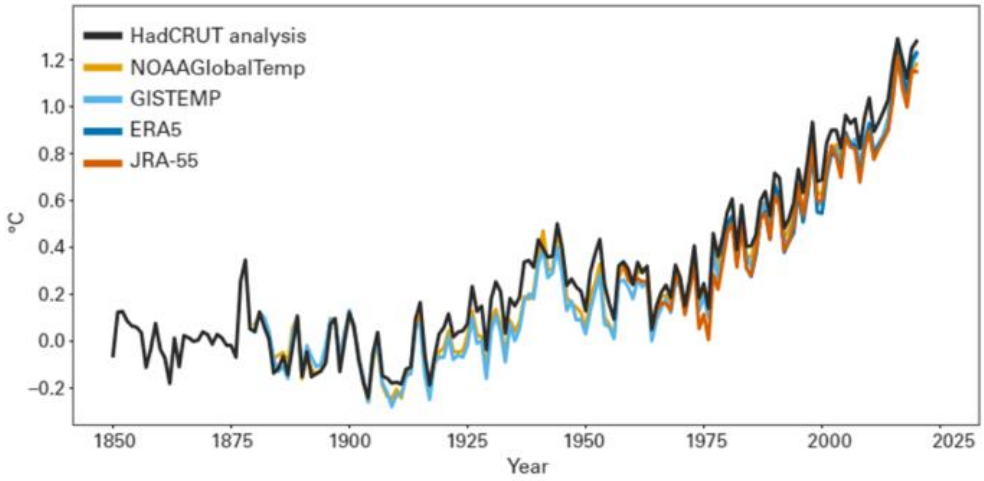

Figure 3. Global annual mean temperature difference from pre-industrial conditions (1850–1900) for five global temperature datasets (Kennedy et al. 2021).

In the last century, the global average temperature is increased by about 1° C. Even if carbon dioxide is not the only GHG nor the one with the highest Global Warming Potential (GWP) index, the exponential increase in its atmospheric concentration due to human activities and the inability of terrestrial organisms to metabolise it at such high rates denote it as the most responsible gas for the greenhouse effect. Starting from the

twentieth century, the use of hydrocarbon combustion as the primary source of global energy production, and the increase of transportation and industrial processes, have meant a steep growth of CO_2 concentration, visible from the graph in Figure 4.

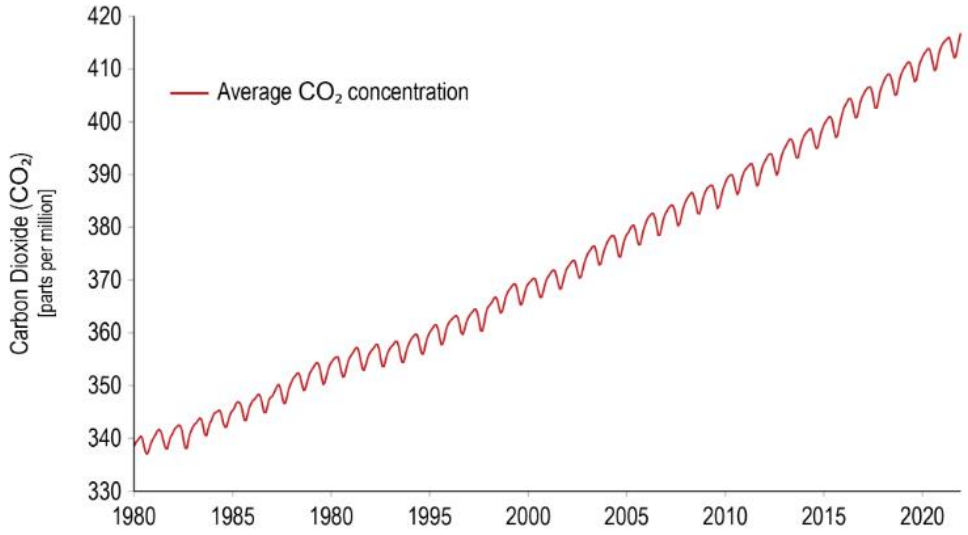

Figure 4. Time series of the global average of carbon dioxide concentration [ppm] (Brewer 2022).

The preindustrial CO_2 level was approximately 280 ppm, with an annual increase of about 2 ppm, was reached more than 400 ppm in 2019. Following this trend, the IPCC suggests that a constant concentration of CO_2 alone at 550 ppm would cause an average increase in Earth's temperature of ~3°C. Such global temperature variation would lead to risks associated with long-lasting irreversible changes, such as the loss of specific ecosystems. Limiting the temperature increase to 1.5°C and maintaining atmospheric CO_2 concentrations around 450 ppm is considered a safeguard threshold.

In this scenario, the climate change mitigation framework consists of all the policies and actions to anticipate, prevent and minimise the causes and the adverse effects of climate change, including the greenhouse effect and its implications. For example, climate change mitigation means preserving and restoring natural ecosystems, using new green

technologies, producing renewable energies, making older equipment more energy efficient, or changing management practices and consumer behavior to reduce GHG emissions. However, more than emitting less will be needed to achieve the climatic objectives established at the International Climate Conference held in Paris in 2015.

Therefore, new strategies in the field of climate change mitigation are increasingly being studied to capture and remove greenhouse gases, mainly CO_2, from the atmosphere.

Innovative technologies may have a valuable role to play. The so-called Negative Emissions Technologies (NET) intervene in the earth's carbon cycle, directly addressing the root cause of climate change and permanently removing carbon dioxide from the earth's atmosphere. However, they are expensive, and they require encouragement with appropriate policies and support from research at a global scale. Instead, among the mitigation possibilities, a cheap, safe, and easy one is related to protecting, conserving, and restoring vegetated ecosystems that act as carbon sinks through eco-engineering solutions.

2.2. Carbon cycle and sinks

To understand the role of natural carbon sinks is important to focus on the modifications in time of the natural exchange of carbon and nutrients among land, ocean, freshwater bodies, and the atmosphere.

Essential elements for life are constantly delivered through the spheres of the climate system. In this global biochemical cycle, carbon is included as the main character because it constitutes the base for molecular structures of living organisms.

Commonly the carbon cycle is intended as the vertical motion of such elements that involves the atmosphere, the vegetation on land, and the ocean.

However, carbon transport is not only a vertical exchange in gaseous form between land and atmosphere; but also a lateral transfer across various ecosystems of the aquatic continuum, which connects all

water bodies, rivers, streams, lakes, reservoirs, estuaries, and coastal zones, to the open ocean. (Regnier et al. 2013). This second direction of the carbon flux and its importance have been known for decades; however, it has been underrated since recent times. The magnitude of this phenomenon is not negligible even if, at present, lateral carbon transport is not included in reports assessing the CO_2 global budgets published by the IPCC.

Indeed, understanding the mechanism driving the carbon cycle and, consequently, the quantitative estimation of lateral carbon flux is highly complex, especially because it cannot be taken as an invariant (Ver et al. 1999).
Anthropogenic perturbations, such as land-use changes, soil erosion (Quinton et al. 2010), liming, the use of fertilisers and pesticides, sewage-water production, damming of water courses, water withdrawal, and human-induced climatic changes have a relevant impact on this global cycle.

Data to build a boundless carbon cycle model are too sparse (Battin et al. 2009). The current Earth system models include the carbon cycle in the physical climate system but ignore the lateral carbon flow. A significant challenge is identifying the drivers of the human impact, predicting their evolution, and including anthropogenic forcings in Earth system models (Collins et al. 2011).

Let us go deeper into analysing the different terms in the estimate of lateral carbon fluxes developed by Regnier et al. in 2013.
Three different elements of the aquatic continuum are taken into account:

- inland waters;
- estuaries;
- coastal ocean and beyond.

Figure 5. is created to illustrate a simplified schema of the lateral carbon transport.

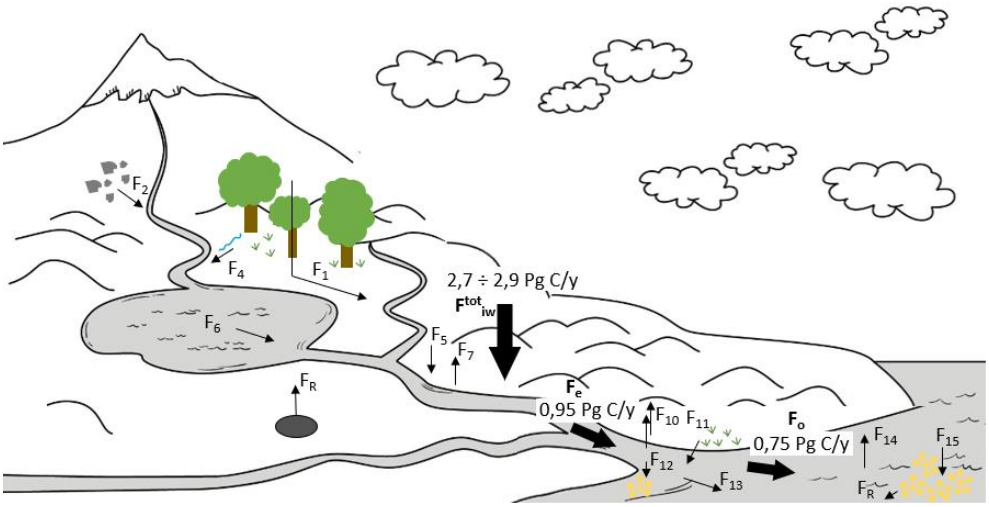

Figure 5. Lateral carbon flux.

Starting from inland waters, the following carbon fluxes are the main ones considered:

- F_1 is the soil-derived carbon, which is fixed in the terrestrial biosphere by photosynthesis processes (Ittekkot et al. 2004);
- F_2 represents the chemical weathering of inorganic carbon from rocks (Hartmann et al. 2009);
- F_4 is one of the sewage water originating from biomass consumption (Prairie et al. 2007);
- F_5 is the net photosynthetic carbon fixation from terrestrial organic matter decomposition;
- F_R represents the part of the carbon physically eroded, resistant to mineralisation (Copard et al. 2007);
- F_6 is from lakes and some rivers as CH_4 (Mendonça et al. 2017);
- F_7 is emitted to the atmosphere as CO_2 (Bastviken et al. 2011).

These presented fluxes result in a total carbon input in inland waters, F^{tot}_{iw}, of 2,7 ÷ 2,9 Pg C/y the efflux is compensated (Battin et al. 2009, Tranvik et al. 2009). This numerical estimation has to be taken with medium-low confidence because of the uncertainties due to the lack of direct flux measurements, the incomplete spatial coverage of the

sampling location, and the not negligible difficulty in effectively establishing the surface covered by inland waters.

Follows the aquatic continuum portion of estuaries. Its carbon flux, F_e, is estimated at 0,95 Pg C/y. It considers the carbon:

- F_{10} exchanged from estuaries to the atmosphere (Laruelle et al. 2010, Cai et al. 2011);
- F_{11} from vegetated ecosystems, like salt marshes, mangroves, seagrass, and macroalgae to estuaries (McLeod et al. 2011, Breithaupt et al. 2012);
- F_{12} buried in sediments;
- F_{13} from estuaries to the ocean (Duarte et al. 2005).

The last term, F_o, is 0,75 Pg C/y, and it is related to the export from the coastal to the open ocean (Borges et al. 2005), resulting from:

- F_{14} air-sea CO_2 fluxes (Cai et al. 2006, Wanninkhof et al. 2012));
- F_{15} sediments sequestration (Krumins et al. 2013, Dunne et al. 2007);
- F_R physical weathering (Blair et al. 2012).

Again the number proposed has to be taken with low confidence.

To these natural fluxes presented, the anthropogenic perturbation effect should be considered due to the impact of human activities on inland waters, estuaries, and the ocean. To give some examples, deforestation and land use change have led to an increase in the export of carbon from inland waters. Regarding estuaries, an increase in carbon export has been observed since preindustrial times due to man-caused perturbation in water drainage. Lastly, the nutrients supply to the ocean has been enhanced. As a consequence, it may increase coastal productivity and carbon burial while also raising the air-to-sea carbon flux.

An accurate quantitative estimation of these fluxes is challenging. Indeed, it is possible to state that the lateral transport of carbon, and the vertical one, have been considerably modified by atrophic

activities, resulting in an excess carbon delivery to the aquatic continuum of around 1,1 Pg C/y.

Extremely relevant is the contribution as carbon sinks of inland waters, estuaries, and coasts, sequestering around 50% of the excess carbon flux. The remaining is exported to the open ocean and emitted into the atmosphere.
These considerations are a step forward in building a boundless global carbon cycle model.

In this context, reminding the importance of carbon sinks and stocks seems unnecessary.

2.3. Coastal carbon stock

The marine ecosystem includes all those natural elements present along the coast.
Right at the backshore are present marine vegetated habitats, which include seagrasses, saltmarshes, macroalgae, and mangroves, and occupy 0.2% of the ocean surface. In the past 50 years, more than a quarter of these areas have been lost due to different factors, such as the increasing nutrients input, heat waves, transformations of the coast, and land use (Waycott et al. 2009, Orth et al. 2006, Adam 2002, Reush et al. 2005, Marbà et al. 2010, Wernberg et al. 2011, Jordà et al. 2012). Even though the percentage of the entire Earth's surface covered by this ecosystem is small, its contribution to carbon burial is enormous. It is responsible for almost 50% of carbon burial in marine sediments (Duarte et al. 2005, Nellemann et al. 2009).

The role of vegetated marine ecosystems as carbon sinks is related to two main factors:

- the community's primary production that, in general, exceeds respiration;
- the ability to trap carbon particles from the water flow and to deposit and store them in the soil.

Despite the extent of marine vegetation being less than 3% of terrestrial forests, its enhanced carbon burial capacity results in the two ecosystems storing a similar amount of organic carbon over millennia (Kennedy et al. 2010). This percentage corresponds to a global store of 10 PgC in the 1m layer of topsoil (Donato et al. 2011). Still an order of magnitude lower contribution than the terrestrial forests but large enough to play a key role in the carbon cycle.

Furthermore, the presence of wood accumulations on the coast also contributes to the carbon stock behaviour of the marine environment. CWD deposit at the seashore is related to the natural deadwood transport from land, either by rivers or directly produced in mangroves, which is drifted from river estuaries to the open ocean, where it is subject to oceanic current mechanisms. Understanding and quantifying this flux is difficult due to the lack of related information on the input and the variability and the complexity of the oceanic circulation. The following paragraph goes deeper into analyzing the carbon content of dead wood.

2.4. CWD carbon content quantification

The interest in the role of carbon stock of coarse woody debris (CWD) in the global carbon cycle is growing. Indeed tree mortality is increasing as a consequence of climatic variability and disturbances (Hartmann et al. 2022). To quantify the carbon present in CWD is necessary to have an accurate estimation of its density, the concentration of carbon (Harmon et al., 2020; Maas et al., 2020), and the decomposition mechanism and rate of the dead wood.

2.4.1. CWD density estimation

The density calculation is not immediate because dead wood in the marine ecosystem undergoes degradation processes.

To knowledge, few studies deal with wood decay at sea (Freschet et al. 2012, Fojutowski et al. 2014). Such a process is influenced by environmental factors, such as oxygen concentration, water temperature, and salinity, and by the chemical and structural characteristics of the wood itself.

Charles et al. in 2016 observed that, as wood decays, density decreases independently from the initial state of the wood. Their experiment uses standardized wood blocks of known initial density that are oven dried for 5 days and then weighted. Logs are kept up to more than a year in seawater under measured temperature and salinity conditions and are randomly sampled to determine the mass loss in time. The sampling procedure involves the freeze drying, cleaning, and weighting of a wood block. In this way, the decay is expressed in terms of mass loss, which is mainly due to biological degradation caused by the presence of wood-boring species activity. The study shows how mass loss dynamics have a flat phase followed by a rapid decrease in mass loss and a final slowing down stage, reaching 48% by the end of the simulation time. It is estimated a daily mass loss of up to 0,38%. This datum is significant. Knowing the initial density of LWD according to the tree species allows an approximate estimation of the mass loss of wood in time.

At this point, the average density of the sampled logs can be assumed to be representative of non-sampled logs. A critical aspect is the applicability of estimation density methods to sites that present different tree species of dead wood or that have an uneven distribution of CWD along the area.

LWD density estimation can be performed with various methods, like the decay classification, the knife test, and the use of penetrometers (Larjavaara and Muller-Landau 2010). Each method follows an inventory step, during which samples are chosen with the line intersect method (Warren and Olsen 1964).
The decay classification is done by visually examining a log at a time and assigning it to a decay class associated with a mean density. The first decay class is the one of lowly degraded wood, whereas the last is related to the high friability of logs (Brown 2002).
To avoid the subjectivity of the previous technique, the knife test is performed. A knife is pressed into a log and classified according

to the penetration (Rouvinen et al. 2002). Also, with this method, repeatability is not assured because of the influence of penetration of the knife type, its sharpness, the applied force, and the location and orientation of the blade relative to the wood fibres.

Finally, penetrometers are used, which are not specifically designed to study dead wood, but in the field of soil science or for living trees. Having a standard instrument allows the involvement of multiple people in the data collection, shortening time requirements.

There are still unknowns on how the wood degradation rate changes when the CWD passes from weather agents, such as air and water, to conditions in the sand and on whether the carbon is maintained unmodified also with respect to CWD's position with respect to the aquifer (above or below).

2.4.2. Carbon in CWD

CWD come from living trees, and like all plants, during their photosynthesis, they take atmospheric CO_2 and fix carbon into their ligneous structure. In particular, lignin has a considerably higher carbon concentration than cellulose and hemicellulose, making dead wood a greater carbon stock than other vegetation kinds.

The questions that arise are:

- how much carbon is embedded in living trees?
- how much carbon is lost during wood decomposition?

Figure 6. shows the carbon fraction in dead wood compared to living trees, using data from the global carbon fraction database. The two curves are similar, although the curve regarding dead wood is shifted to the right with respect to the other.

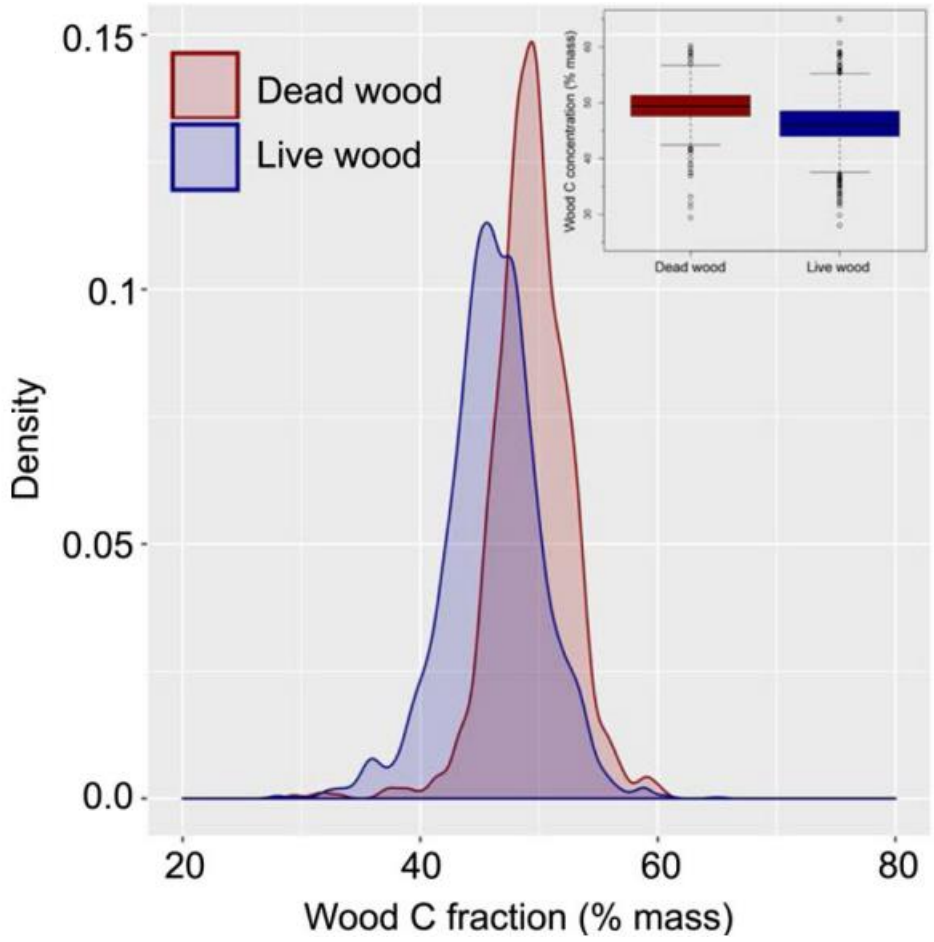

Figure 6. Carbon fraction in dead wood compared to carbon fraction living trees. Data source global carbon fraction database (Martin et al. 2021).

Carbon quantitative estimation in CWD is strongly related to the relationships between wood density and moisture content of CWD. It is known that during wood decomposition, carbon is released. To elaborate a predictive model of this phenomenon, information on decay class, wood density, moisture, and initial carbon content is required (Fukasawa 2021, Martin et al. 2021).

A study conducted by Shorohova et al. in 2021 on CWD degradation due to fungi and invertebrates and carbon concentration points out that:

- during decomposition, the highest variation in density decrease occurs in the first decay class;
- the density decrease is negatively related to wood moisture content. Such aspect was also observed in other studies (Přívětivý and Šamonil 2021, Rinne-Garmston et al. 2019);
- moisture in wood is higher in advanced decay classes than earlier ones;
- moisture variation is independent of the decay class;
- decomposition is independent from CWD proximity to the ground and high air humidity in the study sites;
- the mean C concentration in wood was 46.5%. It did not change with the decay class.

Carbon concentration calculation is effectively conducted by Köster et al. in 2015. Their study focuses on a hemiboreal forest; however, the procedure is valid regardless of the natural environment analysed.
Standardised samples are cut after the fieldwork of collecting CWD pieces and dividing them into decay classes. In the laboratory, the volume of each disc was estimated by multiplying the cross-section area by the average disc thickness, and dry masses of samples are determined in the laboratory after oven drying the samples for 48 h, at 80°C, to a constant mass. Consequently, the basic density is estimated. To analyse the carbon concentrations in CWD, wooden material is grinded from half of the collected discs. An elemental analyser is used to express carbon concentration as a percentage of the weight, compared to the total weight of each sample. Results show that:

- there are significant differences in density and consequently in carbon concentration of dead wood among tree species;
- it is confirmed that the CWD density decreases from the decay class for all tree species;
- there is no significant difference in wood density between moisture categories.

Weggler et al. in their study published in 2012, estimate wood carbon content by comparing four different cases based on the same approach. The parameters considered are the volume maintained the same for all cases, carbon concentration, and the density of CWD that vary. The first uses the 50% default value settled by the IPCC and the average wood density of living trees. The second is based on specific carbon concentration values of tree species and default density values. The third applies carbon concentration values again according to the tree species but average values of CWD density are specific for species and decay class. The fourth and last method uses species-specific CWD carbon concentration and species and site-specific CWD density values as predicted by climate-based regression models. The sensitivity analysis done to compare the four methods shows that by improving the accuracy of the CWD carbon concentration, the carbon quantified reduces. Nevertheless, by improving the CWD density, the carbon concentration estimated reduces consistently. It means that a lower accuracy of the carbon concentration and the wood density inputs leads to overestimating the carbon.

A relevant aspect to point out is the influence that Climate change has and will have on carbon stock in LWD, on the dead wood origin, and transportation rate along the lateral carbon cycle. Deadwood volume loss depends on climatic variables such as temperature, precipitation and relative humidity (Oettel et al. 2023). Considering, as an example, precipitation patterns variation, more intense precipitation events in a specific area could lead to more rapid degradation of trees falling and being drifted by the water. Moreover, precipitation could break logs down more rapidly, speeding up the carbon release in the atmosphere.

2.5. CWD role in dunes geomorphology

Taking CWD's presence at the seashore for granted, let us focus on its role in influencing the coastal ecosystem and sustaining its biodiversity.

The coast is continuously threatened by erosion and modifications due to waves during storm events. As a consequence, the LWD matrix is periodically reorganised. The superficial exposed wood traps the sand blown by the wind reducing the forward sediments delivery. This leads to the burial of the superficial wood accumulation and the constant evolution of the complex dunes system. On the contrary, intense precipitation events may cause the unburial of wood.

Grilliot et al., in their study of 2019, define foredunes as "vegetated shore-parallel ridges of sand built by aeolian sand delivery across beaches". From this description arises the concept that oceanic and aeolian mechanisms, such as sea storms and sea spray, strongly influence the dunes complex. It results from a strong, complex interaction among the atmosphere, sea, vegetation, and coarse woody debris accumulation.

It is an accretion-erosion cycle effectively illustrated by the conceptual model in Figure 7. From case 1 to case 4, the presence of CWD becomes dominant. The transition from one state to another may be rapid depending on wind and wave conditions.

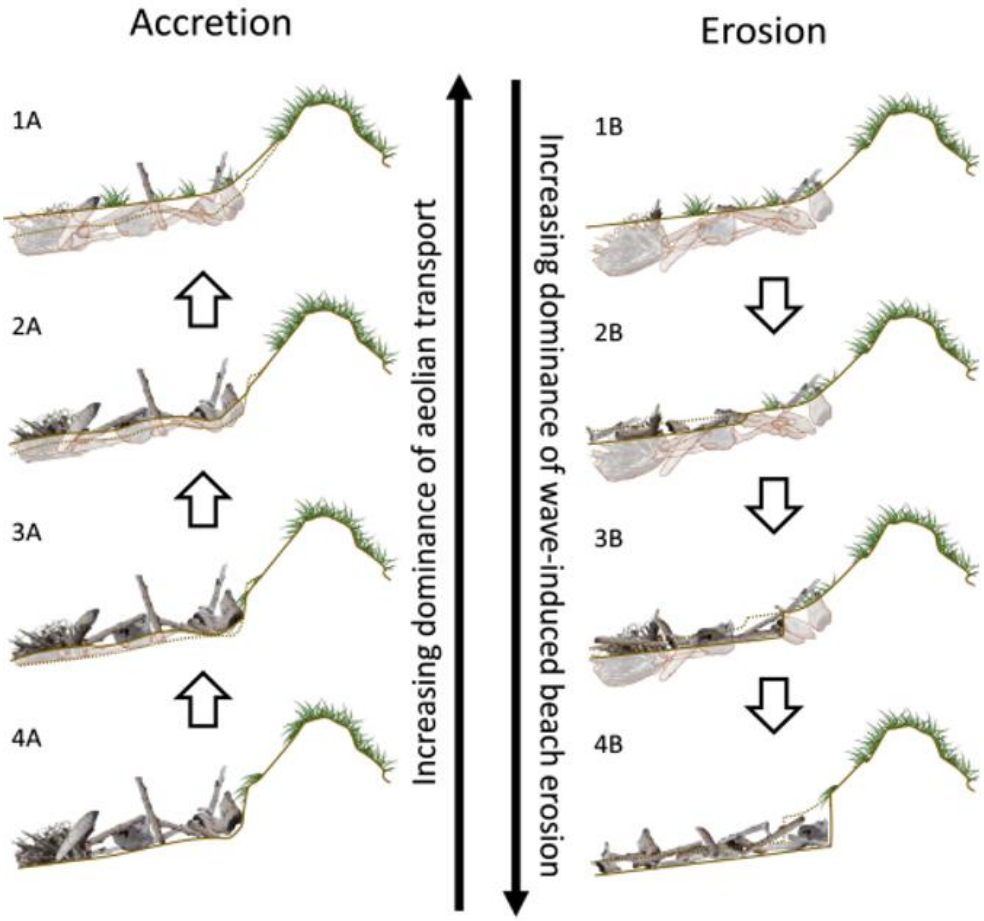

Figure 7. CWD burial-unburial cycles (Grilliot et al. 2019).

Dunes geo-morphology, large or small dimension, continuous or discontinuous, and permanent or ephemeral features, depends on control elements, among which:

- vegetation type, growth rate, density, and distribution (Keijsers et al. 2015, Hesp et al. 2013, 2017);
- the presence of rough elements on the sand, for example, woody debris (Grilliot et al. 2018);
- sand characteristics and supply (de Vries et al. 2014.

An important aspect to point out is the frequency and magnitude of the storm surge. Each time the coast is eroded and the CWD deposit is reworked, it is impacted its ability to modulate waves and function as dune basal structure evolution, and so its role in sediments store and transport to the dunes.

The effect of the LWD matrix on foredune erosion, recovery, and growth varies according to the characteristics of the wood accumulation, such as density, apparent porosity, average diameter of logs and orientation with respect to the direction of incoming airflow. Moreover, it is also influenced by the intensity and timing of the aeolian sediment transport regime and by sea-related factors, such as the nature of the wave and the water level dynamics.

In particular, when the LWD matrix is exposed, the incident wind speed is reduced because of the alteration of turbulence characteristics in the boundary layer. In such a way, sediment deposition is enhanced compared to a flat terrain profile. Furthermore, a denser wood accumulation means greater ground roughness, reducing short-distance sediment transport.

To have a bigger picture, Figure 7 has to be integrated with the impact of wood accumulation on this complex interaction between the beach and the dunes complex, which is modelled in Figure 8.

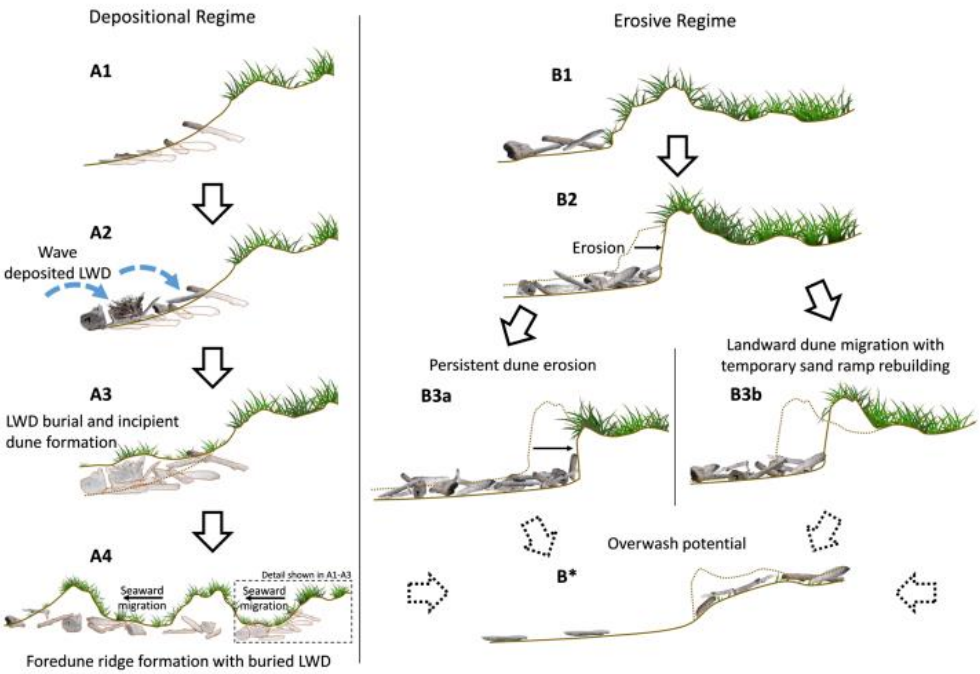

Figure 8. Scenarios of beach dunes evolution (Grilliot et al. 2019).

The *A* regime, on the left, shows the deposition of CWD, which acts as a skeleton for the progression of the dunes. In the middle, the *B* regime describes the inverse process of regression of the dune system due to the erosion of the sandy trap and the transport of the wood debris elsewhere. The variation of the geometric features of the coast could occur seasonally, influenced by meteorological conditions. Studies on the topic should distinguish short-term fluctuations from trends over a long-term time period.

2.6. Geomatics tools for environmental applications

Geomatics is defined as *a systemic, multidisciplinary, integrated approach for selecting the instruments and the appropriate techniques for collecting, storing, integrating, modelling, analysing, retrieving at will, transforming, displaying, and distributing spatially georeferenced data from different sources with well-defined accuracy characteristics and continuity in a digital format* (Gomarasca 2010).

For this study, among the techniques and disciplines constituting geomatics is important to highlight:

- Global Navigation Satellite System (GNSS) to locate objects with high precision, reaching a few centimetres. A GNSS is based on a radiofrequency signal emitted from proper satellite constellations, for example, the Global Positioning System (GPS), which is collected by a ground receiver. Knowing the position of the satellite with respect to the Earth and calculating the distance satellite-receiver, it is possible to define the position of a point. This distance is indirectly retrieved by measuring the time or phase of the signal emitted by the satellite and received by the receiver;
- Geographical Information Systems (GIS) are complex systems to store, manage, analyse, process, and visualise geographic data. It allows combining instruments able to receive, record, represent, and process georeferenced spatial data;
- Photogrammetry, which from images allows the reconstruction of tridimensional models and determines intrinsic characteristics and their position in space;
- Laser scanning or Light Detection and Ranging (LiDAR) systems use incident electromagnetic radiation in the optical frequencies (0,3÷15 μm) to determine the position of objects and measure their distance with respect to the emitter. Laser scanners are of two main types: static or terrestrial and mobile mapping. They both first work emitting laser pulses and, by

measuring the distance from the device to a target, acquire *X, Y, Z* coordinates of numerous points on land. In particular, the laser scanner in mobile mapping modality is not static, meaning it can be mounted on a mobile device to gather high-resolution and high-precision data on a large area in a short time (Vosselman and Maas, 2010).

This survey technique is particularly significant because it gives a high-precision, complete, three-dimensional image of the object or the surface of interest.

Moreover, photogrammetric and laser scanner tools have significantly expanded their support to a wide range of research activities from when the limitations of using these technologies in terrestrial or traditional aerial mode were overcome. Uncrewed Aerial Systems (UASs) were introduced to have versatile and flexible investigations on natural or anthropogenic environments. Several types of small UASs are on the market that can be carried by a single person and offer a high cost/benefit ratio. This approach allows to acquire images from low altitudes, enabling highly detailed reconstruction of 3D features. The necessary components to perform aerial surveys effectively using UASs include:

- Camera capable of capturing high-resolution images. The camera has different specifications, such as resolution, lens type, and image stabilisation features;
- GNSS receiver to determine their precise location and enable georeferencing of the captured imagery;
- Inertial Measurement Unit (IMU) used to measure the UAS orientation and acceleration. It provides data on the UAS roll, pitch, yaw angles, and linear accelerations. This information helps stabilise the UAS and improve the accuracy of the results;
- Wireless communication system to establish a connection with a ground control station. This link allows real-time monitoring of the UAS flight status, receiving commands,

and transferring data between the UAS and the ground station;
- On board small computer processor that manages various tasks, such as image processing, data storage, flight control algorithms, and communication with other components.

For photogrammetry, even a low-cost non-metric camera can be mounted on the drone and following the Structure from Motion, SfM, methodology, which involves capturing a series of overlapping images, and processing, a 3D scene is reconstructed (Iglhaut et al. 2019). By employing a highly automated processing strategy, researchers can process the acquired images and generate dense point clouds representing the 3D geometry of the surveyed area. Remarkably, the spatial and temporal resolutions achieved through SfM can be exceptionally high, and the positional accuracy of the reconstructed features can be surprisingly precise. The point clouds obtained from best practices in close-range photogrammetry can exhibit spatial resolutions and accuracies comparable to those obtained through terrestrial laser scanning. As a result of these advancements, a significant number of scientific papers in recent literature highlight the successful applications of photogrammetric methodologies, particularly employing SfM, in various research fields.

This same workflow is followed to process the photogrammetric data of the case study presented. More information is given in paragraph 4.1.2. of the Methodologies chapter.

The LiDAR sensor as well can be mounted on a UAS system. It collects millions of points of which is known the position, automatically converting energy from a primary form into laser light, a monochromatic and coherent electromagnetic radiation with high intensity. In several cases, photogrammetry and LiDAR techniques are combined to harness each method's strengths and enhance the results' overall quality. By integrating data from both sources, researchers can benefit from the high-resolution and accuracy of point

clouds derived from photogrammetry and the dense and detailed 3D representations obtained from laser scanning (Room et al. 2022).

The applications extend beyond traditional geomatic disciplines. Specifically, these technologies are proven invaluable in studies related to archaeological investigations, infrastructure assessment, natural resource management, environmental monitoring, and many other areas. In particular, in the last decade, geomatics is essential in environmental studies and forecasting, also as a consequence of the Global Earth Observation System of Systems (GEOSS) established in 2005 (Christian 2005). Its purpose is to incentive and engage all participating nations in producing and managing information in a way that benefits both humans and the environment.

2.7. Beach-dunes evolution and coastal monitoring

Until the introduction of UASs, coastal change monitoring was based on 2D information related to the shoreline position evolution supported by perpendicular shore profiles. These data could not fully capture rapid natural coastal modifications after severe events or just regularly. The transition was from quantifying change based on a beach profile every km or so to using photogrammetry and LiDAR technologies, which give a result with tens of millions of points every km, increasing the resolution of the analysis and its efficacy. The weather, particularly wind and rain conditions, may be a potential challenge when operating light UASs in coastal areas. Possible wind and precipitation can significantly impact the stability and manoeuverability of UASs, potentially affecting their flight performance and the quality of data collected. However, there are strategies to mitigate these challenges. Firstly the careful planning of the aerial survey during more favourable low wind hours (< 25 km/h), such as in the early morning, related to the specific UAS capability.

Overall, the integration of low-cost non-metric cameras for photogrammetry, UASs, SfM technology, and complementary techniques such as LiDAR laser scanning and satellite imaging has

revolutionised the capabilities of geomatics. It has provided researchers and geoscientists with flexible tools to efficiently investigate and analyse natural and anthropogenic phenomena while achieving high-resolution and accurate three-dimensional reconstructions.
For example, recent studies examine dune morphological changes using DEMs from various data acquisition methodologies, such as LiDAR, digital photogrammetry, or topographic surveys using laser total stations or GPS (Woolard and Colby, 2002; Mitasova et al., 2005, Anthony et al. 2006; Reitz et al. 2010).

Harmonising information from diverse disciplines and multiple sources to describe coastal morphological vulnerability poses a significant challenge, as Bonaldo et al. (2019) highlighted. Assessing changes in coastal regions and understanding key physical processes occurring at different temporal and spatial scales requires the integration of shoreline geometry and position data. These fundamental indicators enable a quantitative analysis of shoreline evolution, offering insights into the erosion and accretion process (De Serio et al. 2018; Katz and Mushkin 2013; Thébaudeau et al. 2013; Oyedotun 2014). Researchers have explored and applied various statistical methods for estimating shoreline change rates to address this.

2.7.1. Aerial photogrammetry

In general, the potential of UASs photogrammetry has already been proven by several studies from different perspectives (Barry and Coakley 2013, Gülch 2011, Haala et al. 2009, 2011, 2012, 2013, Küng et al. 2011, Vallet et al. 2011, Rosnell and Honkavaara 2012).
Among the advantages, it is relevant to mention the relatively low cost of both the system and the operations, the automation of the survey and its high repeatability, and the high resolution of the final product. Instead, disadvantages are related to the processing phase.

Specifically, the concept behind the application of photogrammetry for coastal monitoring is relatively easy (Gonçalves and Henriques 2015, Jaud et al. 2019, Scarelli et al. 2017). Regardless of the UAS and the chosen camera, regular flights over a few years are performed. An appropriate camera to detect even objects of small dimension and volumetric and morphological beach changes might acquire images with around 10 cm Ground Sampling Distance (GSD) from which retrieve a Digital Surface Model (DSM) or Digital Elevation Model (DEM) with vertical accuracy of approximately 20 cm (Gonçalves et al. 2010, 2011).
The GSD [m] depends on the flight height, H [m], the focal length, f [mm], the sensor's dimension, and on image's dimension. It is a simple geometric ratio that can be estimated through calculators, for example, the PIX4D calculator.

After using a photogrammetric processing software based on the SfM approach, the 2D DSM and the orthomosaic are retrieved. Then, the model can be georeferenced. This procedure can be performed through direct photogrammetry, which is possible thanks to the GNSS receiver embedded in the UAS, whose accuracy is as good as the GNSS signal. Another possibility for the georeferencing of the model is the use of known-coordinate points, called Ground Control Points (GCPs). They can be represented by natural elements detectable from the collected images or markers placed on the ground, for this specific purpose, before the survey.

Specifically, the photogrammetric methodology is suitable to be applied to the study of dunes dynamics. A topographic change is detected by subtracting elevation coordinates, Z, of the same point belonging to two different DEMs retrieved from two photogrammetric campaigns performed in two time periods. In this way, the volumetric change related to CWD deposition, is computed for each cell location. The resulting volume may be positive, negative, or zero and is subsequently interpreted in deposition, erosion, or no change phenomena. Just by summing

these cell values, it is possible to have the desired information over the entire study area (Yoo and Oh 2016).

2.7.2. Aerial LiDAR

Given the increasing use of LiDAR in environmental applications and the high potential they have to be integrated with other remote sensing techniques, particularly in studying the coastal ecosystem, it is relevant to develop a straightforward methodology.
Primarily the acquisition of high-resolution 3D models was related to airborne LIDAR because, with respect to photogrammetry, the processing of the final product is automated (Baltsavias, 1999), Other studies have already provided information on the LiDAR data acquisition and processing and have proved the effectiveness in assessing coastal evolution in response to natural forcings, assess sand-dune volume modifications (Brock et al. 2002, Mitasova et al. 2004, 2009, Sallenger et al. 2003, Saye et al. 2002, Shrestha et al. 2005, White and Wang, 2003 and Woolard and Colby 2002).

Particularly interesting is a study conducted by Eamer and Walker in 2010. It examines coastal CWD accumulations' morphology and sand storage capacity on northeastern Graham Island, British Columbia, Canada. Using coincident high spatial resolution LiDAR data and digital orthophotos, they are able to retrieve DEMs for different ground cover classes, distinguishing sand from wood. These DEMs were then used to quantify the relative storage capacities of LWD.

This approach is quite similar to the one intended to be applied in this study because it uses remote sensing high-resolution data to look at changes in the volume and morphology of the beach-dune complex. In this specific case, digital aerial photography data are used to perform a supervised classification, which assigns the land coverages, sand, and CWD to different classes. The choice to perform the supervised classification is related to the similar

spectral signatures of the elements willing to be distinguished. Consequently, the algorithm training phase is highly critical and done manually. Then, this procedure is transferred to the LiDAR datum, retrieved during an in-site survey, considering that a point in a specific location in the LiDAR point cloud will be in the same class as the same point in the aerial photo already classified. In this step, the LiDAR point cloud is rasterised and to points in the orthophoto UTM (Universal Transverse Mercator) coordinates are assigned. As a result, the original LiDAR points contain UTM coordinates, elevation, and ground cover class information.

Follows the DEM generation for sand and woody debris through gridding and Kriging interpolating the data with a 2 cm surface spatial resolution. To calculate the volume of the portion including CWD buried under the sand and the sand, are defined:

- *HHWMT* [m], highest high water mean tide, a horizontal baseline above which sand transport and deposition are governed by the wind and not by the waves;
- *MSL* [m], mean sea level.

At this point, it is possible to conclude that *HHWMT* is above the mean sea level of a quantity equal to *HHWMT-MSL*. The volume of the sand surface DEM, C_e, is calculated from that baseline. In this way, it is possible to predict the amount of wood that acts as a structure of the current dunes complex. The volume of the wood visible above the sand surface, C_p, is considered as a potential for the further evolution of the dunes system. Figure 9 allows to picture the reasoning behind the entire study.

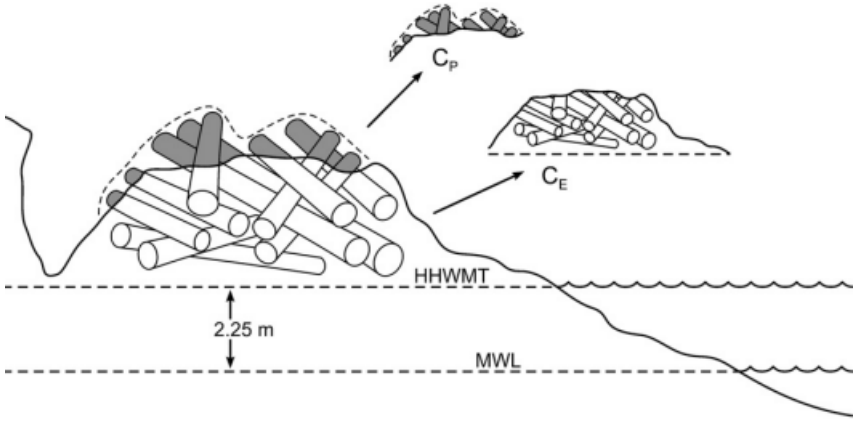

Figure 9. Model of CWD deposit. C_e is the volume occupied by both CWD and sand transported and deposited due to the wind, while C_p is the volume of superficial wood potentially buried in the future (Eamer and Walker 2010).

2.7.3. Satellite imaging

Using satellite optical remote sensing technology can greatly enhance ecosystem management, providing synoptic and frequent coverage of large coastal areas that offers valuable information for decision-makers and researchers. Indeed, satellite optical remote sensing allows for monitoring environmental dynamics, such as shoreline changes, coastal erosion, and sediment transport. By regularly analysing satellite imagery, it is possible to identify areas at risk, track coastal evolution and implement appropriate management strategies. Thanks to their capability of capturing multispectral data, they enable the detection and monitoring of specific components of coastal habitats like coral reefs, seagrass meadows, mangrove forests, and wood deposits. Moreover, satellite imaging use is promoted by the great advantage of free access to data sources. Comprehensive and up-to-date information is available and can be combined with other kinds of data, such as ground-based observations or with data from other data sources, to obtain a more complete understanding of the coastal ecosystem and its dynamics (Kachelreiss et al. 2014; Pettorelli et al. 2012, 2014).

According to the level of detail desired for a specific application, the choice of the data source is based on the trade-off among the satellite sensors' characteristics: spatial resolution, spectral resolution, and temporal resolution. Some sensors prioritise higher spatial resolution but may have lower temporal resolution or limited spectral bands. Others may prioritise frequent revisits and spectral diversity but have a coarser spatial resolution.

Bergsma and Almar, 2020, underline that for specific environmental applications such as coastal monitoring, Sentinel-2 data belonging to the European Copernicus constellation are effective. In fact, high-frequency Sentinel 2 data are able to cover coastal areas and describe coastal, physical, and biological processes. Sentinel 2 based methods are capable of having a large spatial scale DEM for mid- to high-latitude coastal zones and sporadic spots for lower latitudes where 2 orbit swaths overlap and coastal bathymetries. According to the location of the site surveyed, the European Sentinel-2 satellite has a spatial resolution from ~ 10 to 60 m depending on the band, spectral bandwidths from 10 to 60 nm, and a revisit period of ~ 2÷3 days (McCarthy et al. 2017).

However, some open challenges are still associated with the interpretation of satellite data for beach-dunes evolution and coastal analysis. They include cloud coverage and the presence of light-absorbing aerosols in the marine environment. To address the atmospheric effects from satellite imagery, such as scattering and absorption by gases and aerosols, advanced atmospheric correction techniques specific to the coastal zone may be required (McCarthy et al. 2017).

Furthermore, the number of studies using satellite imaging to gather field information specifically about wood deposits in different natural environments is increasing. In fact, the possibility of having access to very high resolution (<1 m) satellite data makes detecting CWD over large areas real. In this case, an additional issue is related to automatically extracting wood with respect to other natural elements present in the images, because

of the similarity in spectral characteristics, for example, of CWD with sand or vegetation; especially since information on the spectral signature of different wood deposit types in natural depositional environments is scarce.

The study of Sendrowski and Wohl, 2012, is relevant to be reported to fill this gap. Their objective is to apply the classification workflow shown in Figure 10 to automatically individuate five CWD accumulation types in three natural riparian environments in North America. The wood deposits have different spatial heterogeneity, distribution, and orientation characteristics.

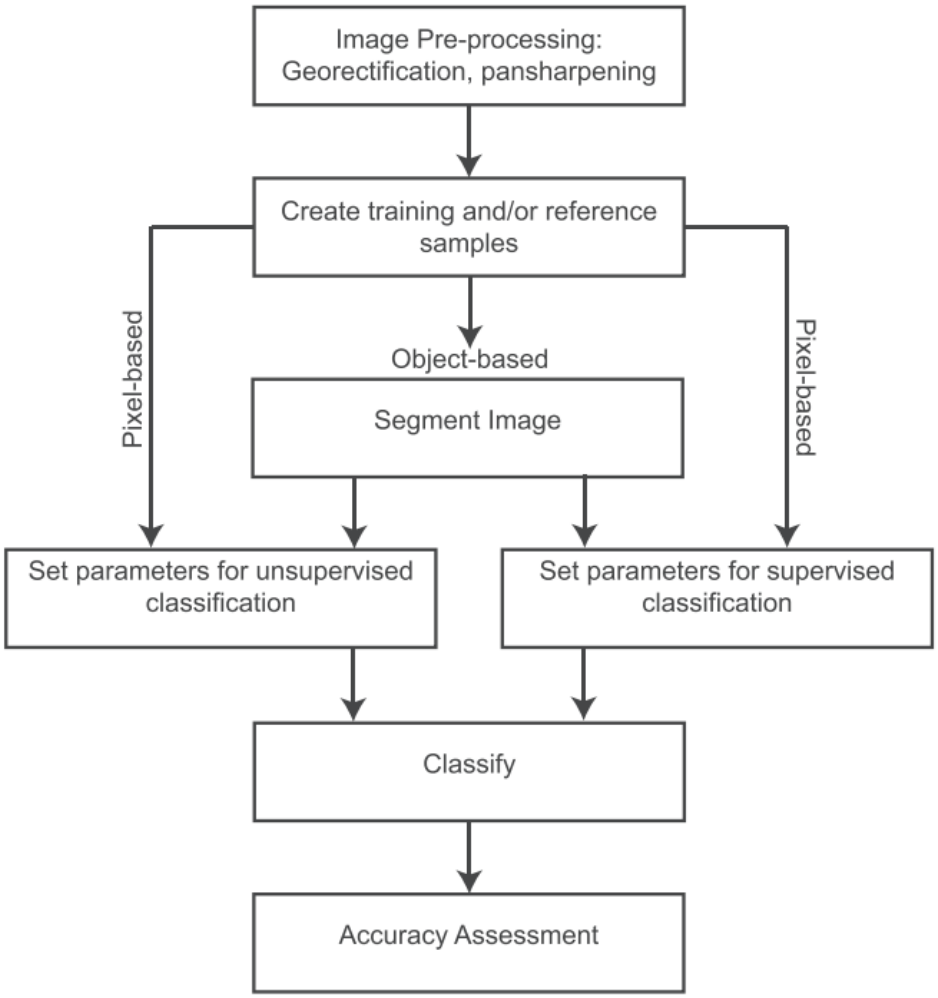

Figure 10. Workflow for image analysis and classification (Sendrowski and Wohl, 2012).

For the study purpose, cloud-free multispectral images are used, with low water levels, to avoid LWD being submerged and corresponding to peak vegetation greenness to bypass spectral confusion.

Object-based and pixel-based image analysis classification results with supervised (support vector machine, SVM) and unsupervised (ISO clustering) approaches are compared. The labelled classes are vegetation, water, sand, and wood. In the supervised classification process, 100 training samples were manually selected for each

class. These training samples serve as representative examples of the different categories in the image. By having a sufficient number of training samples, the classification algorithm learns and differentiates between the various classes accurately. For both approaches, the accuracy of the classification procedures is verified by looking at the confusion matrix; overall are achieved accuracies of 65÷99%, proving that the automated image classification is valuable in CWD analysis. Supervised classification has led to more accurate wood maps, even in dispersed deposition areas. However, it is important to consider that the classification outcomes can vary significantly across different environments, particularly due to the spatial arrangement of wood in the landscape.
In fact, the conclusion is that LWD deposits show variable responses across environments.

The Mackenzie River Delta case study presents a recent example of wood deposit detection and carbon estimation from high-resolution satellite imagery (Sendrowsky et al. 2023). This area is considered "the world's biggest cumulative logjam mapped in the N.T.K.," with more than 400,000 superficial caches of wood, resulting in 3.4 million tons of carbon. To understand the significance of this carbon stock, such quantity is "equivalent to a year's worth of emissions from 2.5 million cars." The research also analyses the origin of all this wood, concluding that dead trees in the forest are drifting because of the snow melting into rivers and getting transported to the target site.

This study highlights the validity of satellite imagery in this field and once again recalls the importance of carbon stocks and the relevancy of the lateral carbon cycle.

The significant limitation of satellite imagery is that it only maps what is visible. No information is retrieved on what is hidden below living vegetation or buried underground. From what concerns the previous case study presented, considering buried biomass, it is possible that the river delta stores twice as much carbon than what is calculated.

2.8. Spatial Statistics for environmental applications

Caution needs to be exercised when quantifying and interpreting volumetric changes and related geomorphic responses from DEMs because uncertainties and errors related to surveying and interpolation methods affect their precision and accuracy. Furthermore, to detect volumetric changes, DEMs are subtracted, adding an uncertainty associated with the comparison of DEMs with their uncertainties already.

Complementary to geomatics, spatial statistics have the potential to identify and quantify spatial and temporal trends in landscape morphodynamics with the application of the Local Indicators of Spatial Association (or Autocorrelation) method.

The end-point rate (EPR) method, proposed by Genz et al. (2006), is one of the simple, straightforward approaches for estimating shoreline movement by calculating the distance between the oldest and most recent shorelines divided by the time elapsed. Foster and Savage (1985) introduced the average of rates (AOR) method, which computes separate end-point rates for various combinations of shorelines. Another approach is the linear regression rate-of-change (LRR) statistic, which involves fitting a least-squares regression line to all shoreline points along a transect to determine the rate as the slope of the line (Dolan et al. 1977). The jackknife (JK) method, as implemented by Dolan et al. (1991), utilises an iterative linear regression by omitting one shoreline point in each iteration. Furthermore, the weighted linear regression (WRL) method (Genz et al. 2006) assigns greater weight or emphasis to more reliable data, as determined by the variance in measurement uncertainty.
However, concerns arise regarding the suitability of linear models in this field, given that shorelines often exhibit non-uniform patterns of recession and accretion (Douglas and Crowell, 2000; Thieler and Danforth, 1994 a, b). Other studies have used parabolic curve fitting

and other regression models that are more representative (Armenio et al. 2017b, 2019, Short and Trembanis 2004, Blossier et al. 2015).

Furthermore, recent research conducted by Eamer and Walker in 2013 aims at detecting a change, in time and space, in the beach-dunes profile, such as erosion or deposition, applying local Moran's I_i statistics on data retrieved from topographic surveys and airborne LiDAR. It distinguishes positive and negative spatial autocorrelation according to a location's attribute value in relation to its neighbours' values (Nelson and Boots, 2008).

Their study is an evolution of a previous work (Eamer et al. 2013), which uses a simplified student's t distribution method (Wheaton et al. 2010). More in detail, data airborne data collected are integrated and compared to more frequent laser total station surveys to generate DSMs. Then DEMs subtractions are performed, generating interval maps of topographical change normalised against the initial LiDAR surface to show seasonal trends in volumetric change at the study area. At this point, the local Moran's I_i is implemented, using the GeoDa™ software, to filter the DSMs subtraction with the local Moran's method. The results demonstrate the utility and the validity of Moran's I_i method in detecting and quantifying significant volumetric changes and associated morphodynamic patterns in the coastal dunes complex.

There are evident advantages of incorporating spatial statistics into a geomorphic study, among which:

- the investigation is statistically grounded rather than largely observational or arbitrary;
- the analyses are spatially guided or based on the variation of an attribute of interest within a spatial neighbourhood.
- the potential to provide new insight into underlying process-response relations in ecosystems through computational pattern recognition.

2.9. Gap and research questions

From the analysis of existing literature, a knowledge gap is perceived.

Is it possible to develop an indirect method using geomatics tools for volumetric CWD estimations?
Which dataset, between photogrammetric and LiDAR, is able to represent the area better?
Which tool among the presented ones is better for volumetric estimation?
Is there a correlation between the geometrical characteristics of the photogrammetric and LiDAR point clouds and the physical properties of the wood?
Is there a correlation between the LiDAR dataset's characteristics and the physical properties of the wood?
Is it possible to representatively model a large area having information on subsampled small regions?

This work aims at answering those research questions with the case study developed in Chapter 3.

3. Case study: San Rossore Regional Park, sand dune habitat and ecosystem

The Natural Park of San Rossore, Migliarino, Massaciuccoli is a protected area that covers 23.000 hectares, to which is added the Protected Marine Area Secche della Meloria. As Figure 11 illustrates, this area is located in Italy, in the northern part of the region of Tuscany (latitude,43.6-43.9° N; longitude, 10.2-10.5° E; altitude,5 m.a.s.l.). It stretches from the sea to the inland, between the Italian provinces of Pisa, Lucca and Livorno.
The ARPAT (Agenzia Regionale per la Protezione Ambientale Toscana) reports that this area has a sub-humid Mediterranean climate with an Annual Average Temperature of >15°C and Annual Average Rainfall of around 800 mm.

The landscape is characterised by the meeting between land and sea, which creates a large variety of flora and fauna, habitats, and ecosystems. 34 km of coast evolves in two main components:

- a complex dune system along the backshore;
- woods in the inland.

The park was officially established in 1979, and in the last decades, it has been included in projects activated and implemented to follow purposes of territorial protection and governance for this area, among which:

- the protection and environmental recovery of wetlands and dunes;
- the ecological balance of the area;
- the safeguarding, qualification and strengthening of agro-forestry-cultural activities in line with the destination of the area;
- the cultural and recreational use of the environment by citizens.

These design paths are mainly dedicated to conserving and redeveloping natural areas, especially those of particular environmental importance, such as wetlands, woodlands, and dunes.
In fact, there is the alternation of open access parts for bathing and recreational purposes, such as trekking, sports, laboratories, and other activities, with an integral natural reserve not accessible to the public. Natural reserves cover 10% of the territory itself and refer to areas with a high level of protection, to preserve the ecosystems and their peculiarities as much as possible, safeguarding all the species hosted by the park.

In particular, the ISPRA (Istituto Superiore per la Protezione e la Ricerca Ambientale) reports that San Rossore is included among the sites in the national program for the restoration of the coastal-marine ecosystem through natural engineering strategies, thanks to its peculiar three dunes complexes. The dune systems, consisting of a mosaic of natural habitats, are composed of the typical sequence: embryo dune, mobile dune, fixed dune, and back dune, with sparse vegetation and pine forests.

This study focuses on two large test areas, *A2* and *A3*, located in San Rossore Regional Park. San Rossore is one of the 16 natural reserves

within the park territory, at the seashore of the Tyrrhenian Sea, a few kilometers from the center of Pisa. From the sea to the interior, it is characterized by beaches, dunes, forests, marshes and waterways, agricultural landscapes, and urban areas. As a consequence, it is full of biodiversity. Among the easily observable animals, are the fallow deer, the wild boar, and a high presence of birdlife. In addition, there is a large variety of vegetation, with more than 500 species of vascular plants.

A2 and *A3* are shown, delimited respectively in yellow and in red, in the zooming-in satellite map below, in Figure 11.

Figure 11. San Rossore Regional Park location and zoom in the study areas *A2*, in yellow, and *A3*, in red (Ciccarelli et al. 2010).

Further zooming in, the two areas are shown in more detail in Figure 12. Both are rectangularly shaped, around 115 m^2 wide. Looking at the true color images, it is possible to distinguish different landscape elements clearly. From left to right:

- the sea is colored greenish;
- the beach and the dunes system in beige tones, with the darker part representing the accumulated mixture of woody debris and other materials;
- the vegetated part, from small shrubs to thick maritime pine wood.

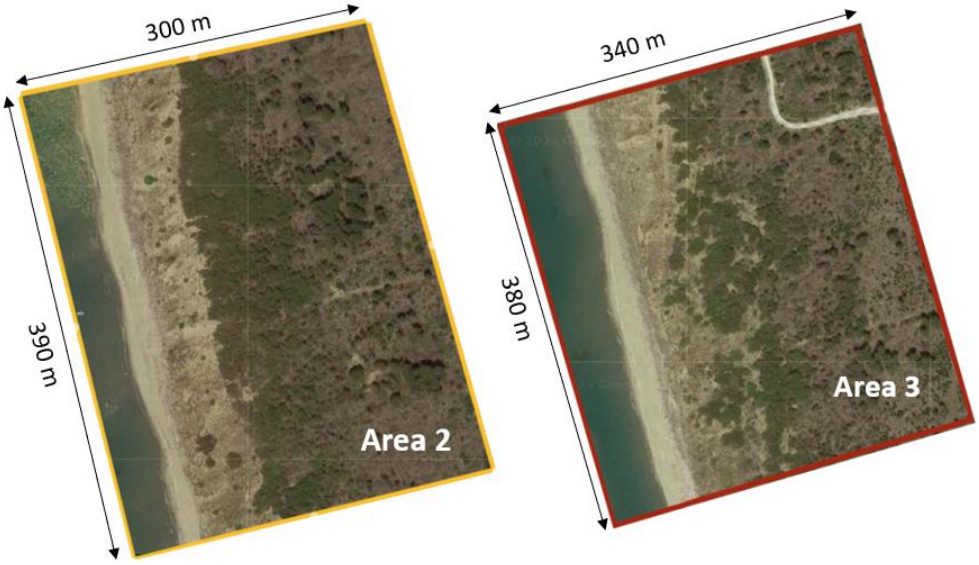

Figure 12. Zooming in *A2* and *A3*.

The woody debris deposit all along the coast is the target of this case study. Figure 13 illustrates two photos of the wood accumulation in *A2* and *A3*, taken during the site survey in May. It is possible to notice the abundance of logs and debris smoothed by the seawater. The accumulation extent goes all along the beach in length and around 10m wide.

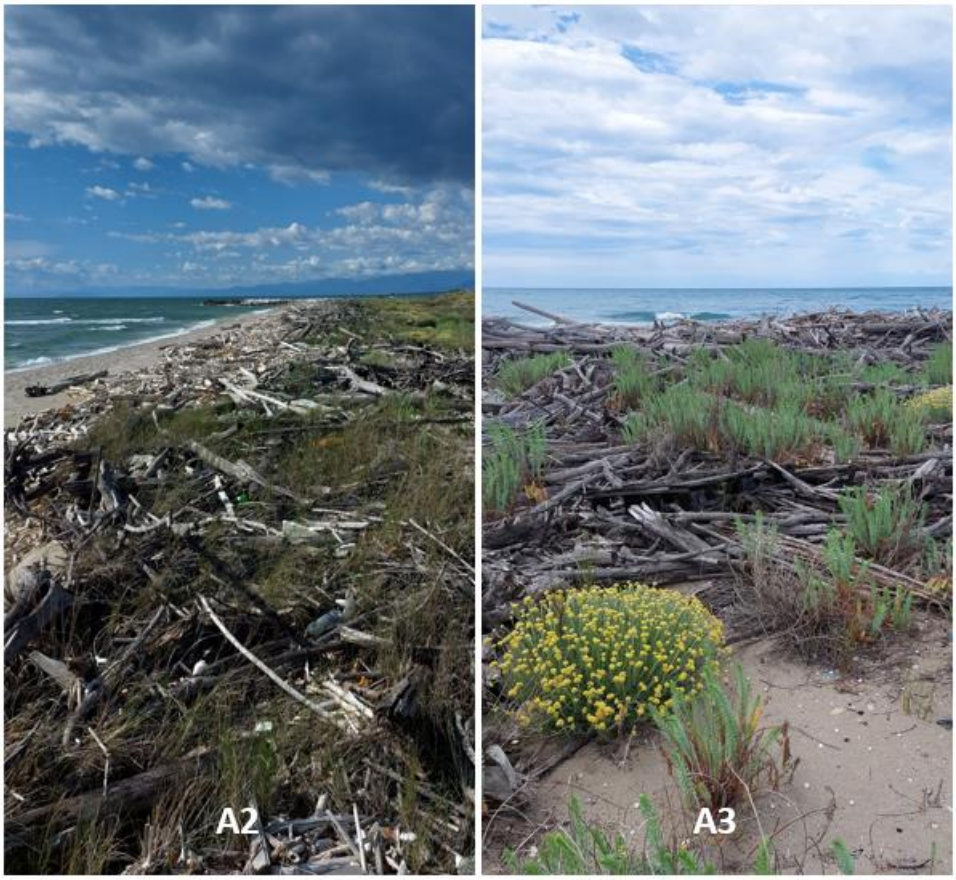

Figure 13. Photos of the coarse woody debris accumulation in *A2* and *A3*.

4. Methodologies

The methodologies applied are illustrated for each of the tasks reported below:

1. Data collection
2. CWD volume calculation scenarios for the subareas *A2a, A2b, A3a, A3b*;
3. CWD volume calculation method choice and CWD density calculation;
4. Total CWD Weight in *A2* and *A3*;
5. Conversion from weight to carbon stock;
6. Statistical analysis of the photogrammetric and LiDAR datasets.

In addition, the flow chart in Figure 14 summarizes the steps of the methodology followed.

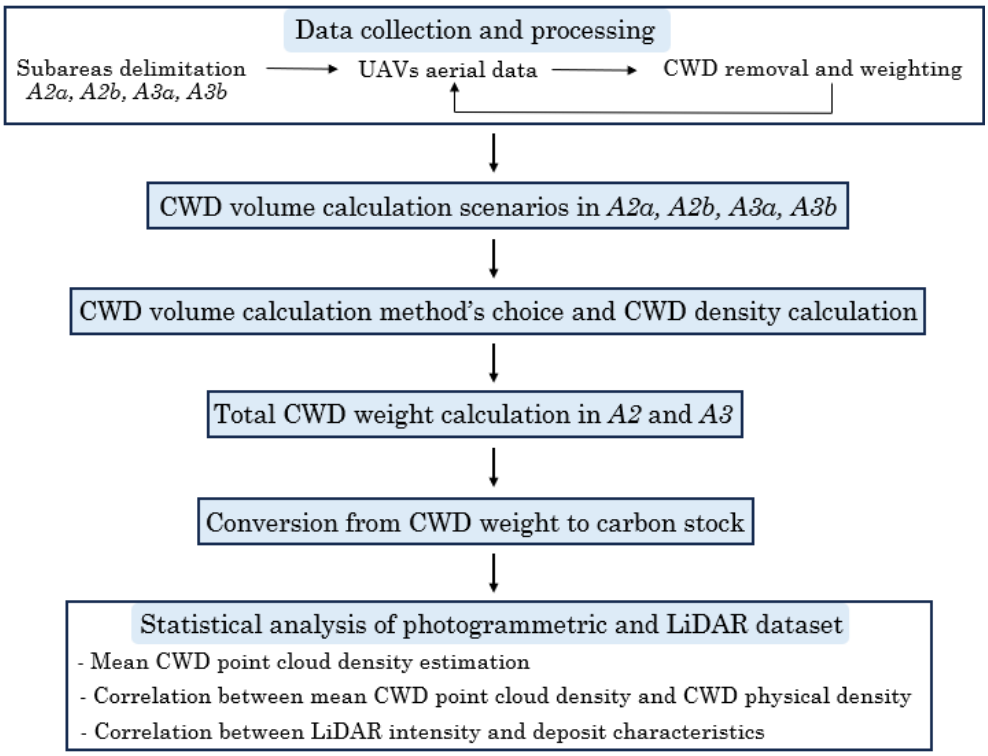

Figure 14. Methodology flow chart.

4.1. Data collection

The data collection was performed during a survey in May for both *A2* and *A3*, structured in the following steps:

1. Subareas delimitation *A2a, A2b, A3a, A3b*
2. UAS flights and data processing
3. Removal and weighting of CWD (Coarse Wood Debris)

4.1.1. Subareas delimitation *A2a, A2b, A3a, A3b*

This paragraph explains the delimitation procedure of two small subareas for each large area. For this purpose, a warning tape and a measuring tape are required. These four portions of the large areas are chosen after an in situ visual inspection. The idea is to have at least a sample characterised by more sparsely distributed large logs and a sample with a dense accumulation of smaller woody debris. The deposit density has to be considered more as an apparent porosity, meaning the presence of voids filled with sand among logs and woody debris of different dimensions. In addition, for each subarea, coordinates of a central point are stored using the GNSS dual frequency receiver in Network Real Time Kinematic (NRTK) technique; such coordinates are shown in Table 2.

4.1.2. UASs flights and data processing

UAS flights with high-efficiency instruments are performed. In particular, photogrammetric and LiDAR flights are performed with the DJI M300 RTK (Real Time Kinematics) drone. For the photogrammetric flight, the DJI_P1 sensor is used (https://enterprise.dji.com/zenmuse-p1). It integrates a 45 MP full-frame sensor with interchangeable fixed-focus lenses on a 3-axis stabilised gimbal. While, the LiDAR data are collected with the DJI_L1 sensor (https://enterprise.dji.com/zenmuse-l1), which integrates a Livox Lidar module and a high-accuracy IMU on a 3-axis stabilised gimbal. Both sensors are shown in Figure 15.

Figure 15. DJI_P1 and DJI_L1 sensors, mounted on the DJI M300 RTK drone, respectively, for photogrammetric and LiDAR flight.

The objective is to retrieve a 3D model of the study area with respect to the global reference system. For this purpose, from seven to ten GCPs are placed in each test area. They have to be well distributed around the area, adequately fixed on the ground, and put in such a place as to be visible from an aerial survey. The GNSS receiver is used in NRTK modality, reaching a few centimeter accuracies.

Figure 16. GCP settling.

Then, two flights with each system are performed for each area. In particular, a first flight is done right after the subarea delimitation described in step 1 to obtain a DSM. A second one follows step 3 to get a Digital Terrain Model, DTM, of the delimited subareas.

These data acquired are processed to obtain the final product, which is a high-resolution georeferenced orthomosaic (EPSG: 32632) with a 2cm GSD. The processing was realized by the researchers from the geomatics lab of the Department of

Environment, Land and Infrastructure Engineering (DIATI) of Politecnico di Torino.

Although a full explanation of such processing steps is not the purpose of this study, adding a little information about point cloud generation is important.

Starting from the photogrammetric dataset, P1, standard structure from motion, SfM, the photogrammetric workflow has been applied using Agisoft Metashape Software (AM) (Girod et al. 2017); the reports of the processing can be found in Annex 1. This procedure is shown in the flow chart in Figure 17. It produces a georeferenced DEM and an orthomosaic giving as inputs imagery and geolocation data (Westoby et al., 2012; Kääb et al., 2014; Ouédraogo et al., 2014 Nolanet al., 2015; Eltner et al., 2016). The information related to the camera intrinsic parameters, such as sensor and optics, the relative camera location and angles, the camera position during the survey, and GCPs, is all combined to produce a reconstruction of the terrain through stereo matching.

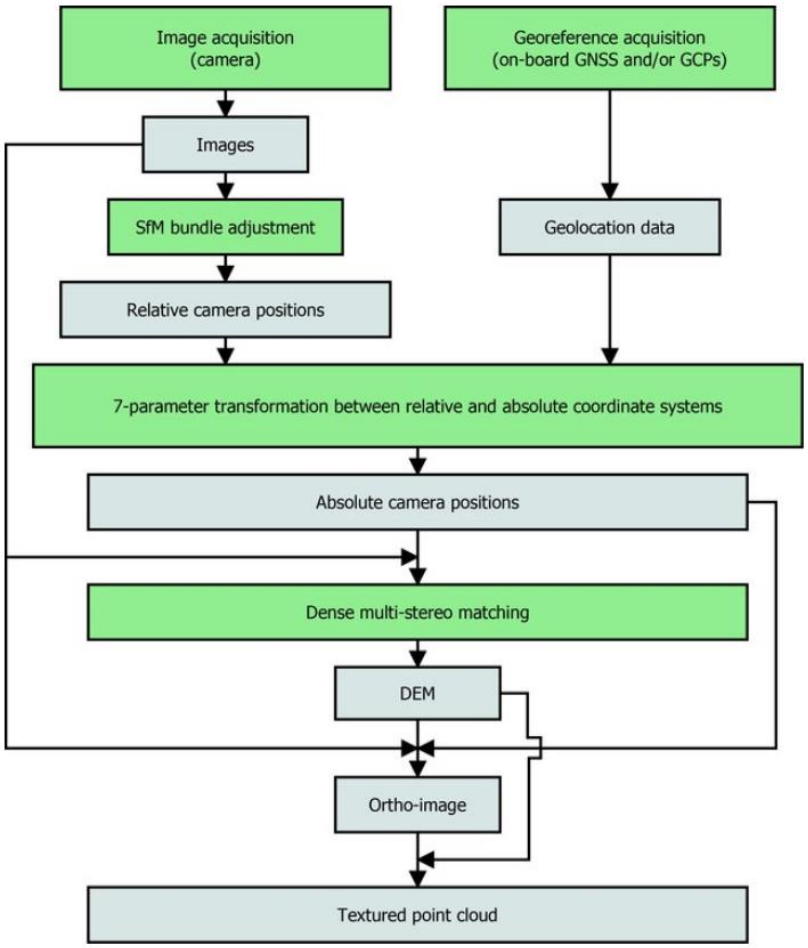

Figure 17. Standard SfM photogrammetry processing workflow. Green boxes are processing steps, and grey boxes are products. (Girod et al. 2017)

The characteristics of the resulting DEM from the photogrammetric data are reported in the following Table 1.

Photogrammetric dataset				
DEM	**Radiometric information**	**Resolution [cm/pix]**	**Point density [pt/cm^2]**	**Total points number [pt]**
A2_PRE	RGB	2,92	0,118	491.334
A2_POST		2,98	0,113	230.322
A3_PRE		3,40	0,087	634.791
A3_POST		2,89	0,12	1.683.429

Table 1. P1 processing results report.

Moreover, for what concerns the LiDAR dataset, the DJI Terra proprietary software was used for the point cloud processing.
The UAS data are opened in the proprietary software DJI Terra. The following setting parameters are applied:

4.2. point cloud density → high;
4.3. optimize point cloud accuracy → yes;
4.4. output coordinate system → WGS84;
4.5. reconstruction output → PNTS, LAS.

At this point, the point cloud is exported in the chosen format, which records additional attributes for each point as the RGB color, the signal intensity, and other information (Štroner et al. 2021).

4.1.3. Removal and weighting of CWD

This paragraph illustrates the wooden material's removal and weighting in the previously delimited targeted subareas.

Working gloves, a pair of work trousers, a chainsaw, a suspension balance, and a rubble bag with a metal hook are used for this step.

Considering a delimited subarea, sized around 2m x 3m or 3m x 3m, loads of superficial wooden pieces are picked up and placed in the rubble bag. Particular attention is paid to evaluating and leaving aside what is outside the limit and what is covered by sand. Logs are cut using the chainsaw, taking all the required precautions when necessary. Follows the calibration of the suspension balance and the weighting, lifting the bag manually, and reading the value on the screen.

Figure 18. Wood weighting.

For example, Figure 19 below shows two delimited subareas in *A2* before and after the removal and weighting of the coarse woody debris.

Figure 19. *A2*a and *A2*b delimited subareas before (*A2_PRE*) and after (*A2_POST*) the wood removal and weighting.

The same procedure is performed in *A3*.

Table 2 sums up the LWD weighting output. In particular, the total net weight already considers the tare subtracted.

Area	Coordinates			Total net weight [kg]
	Longitude	Latitude	Orthometric height	
A2a	602332,669	4846840,971	2,515	59,30
A2b	602321,220	4846897,073	2,477	49,80
A3a	602817,459	4842807,891	2,486	226,24
A3b	602860,160	4842682,197	2,846	190,74

Reference System: wgs84/utm32n

Table 2. Total net weight for each subarea.

A relevant aspect observed is that the wood accumulation is not only superficial. Digging a 40 cm deep hole in the sand, it was still possible to find wooden pieces, as shown by the photo in Figure 20. This aspect is strictly related to the complex dune structure.

Figure 20. CWD was found digging a 40 cm deep hole in the sand.

4.2. CWD volume calculation scenarios for the subareas *A2a*, *A2b*, *A3a*, A*3b*

One of the goals of this study is to use an indirect method to estimate the total volume of the large woody debris in *A2* and *A3* to retrieve an estimation of the carbon stock. Thus, the photogrammetric and the LiDAR point clouds are considered. In this specific case, the photogrammetric point cloud is more accurate than the LiDAR data because this last one has a sparser point cloud distribution; probably due to a too high flight height.

Such an aspect is observable just by zooming in on the two images and focusing on the points distribution in space.

For example, Figure 21 illustrates the same region in *A2* represented by the photogrammetric dataset on the left and by the LiDAR dataset on the right using the same zoom of the working space. The point cloud density difference is evident. In particular, the white rectangle highlights a reddish plastic debris easily detectable in the image on the left, correspondent to the photogrammetric dataset. In contrast, it is almost unrecognizable in the LiDAR point cloud on the right.

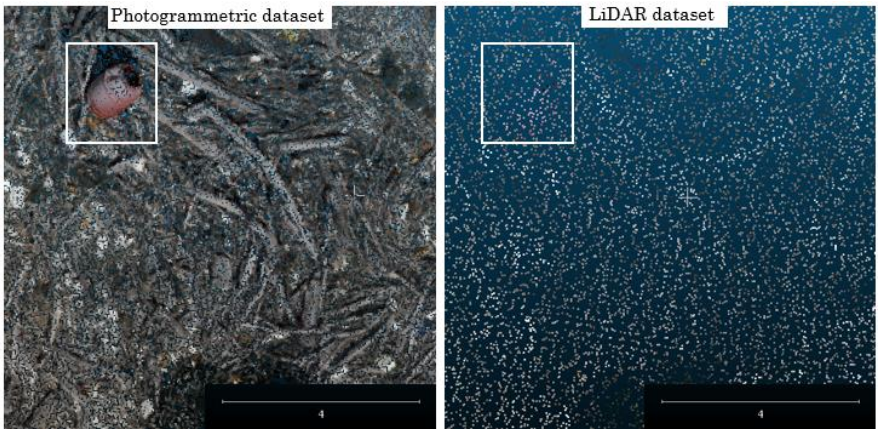

Figure 21. Photogrammetric and LiDAR point cloud densities comparison.

For the photogrammetric and the LiDAR datasets are available a *_PRE point* cloud with the target subareas delimited and a *_POST*

point cloud resulting from a UAS flight performed after the wood removal and weighting. In both cases is followed the same procedure.

The two, *_PRE* and *_POST* 3D point clouds, are loaded in the processing software CloudCompare. Using the segmentation tool are segmented the subareas: *A2a_PRE, A2b_PRE, A3a_PRE, A3b_PRE* and *A2a_POST, A2b_POST, A3a_POST, A3b_POST*. Moreover, Cloud Compare is able to create raster files, which are then loaded into QGIS software to work on geospatial data. It is important to set the same, correct reference system both in the workspace and for the files, WGS 84/UTM zone 32N.

Three different methods are applied to perform the volume calculation:

1. Automatic method applied on the point cloud;
2. Automatic method applied on the raster files;
3. Manual method applied on the raster files.

Volume calculation scenarios according to the input data type and the software used are summarised in Table 3 below.

Data type	Software	Volume Calculation Method
Point Cloud	CloudCompare	1. Automatic method applied on the point cloud
Raster file	QGIS	2. Automatic method applied on the raster file
		3. Manual method applied on the raster file

Table 3. Volume calculation method according to the data type in input and the software used.

4.2.1. Automatic method applied on the point cloud

Directly in CloudCompare, there is a tool called "Volume" that needs in input a DSM ("Cell/After") and a DTM ("Ground/Before") to which respect calculate the volume. In this case, respectively are inserted the segmented subareas *_PRE* and *_POST* from the two flights. The segmentation of the subareas is shown in Figure 22 for *A2* working on the photogrammetric dataset. Showing the

cut of the LiDAR data is not effective due to the sparse point cloud density distribution already pointed out in Figure 21.

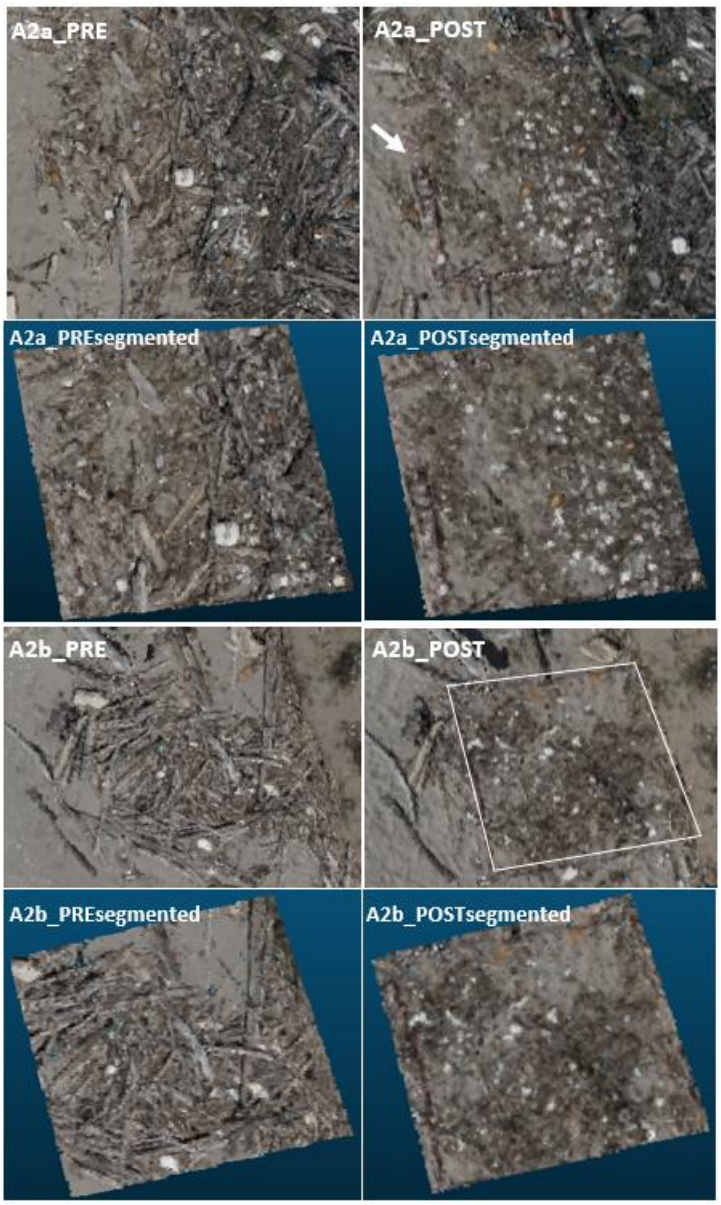

Figure 22. Segmentation of *A2a, A2b* from the photogrammetric dataset.

Looking closely at Figure 22, the white arrow helps to notice the warning tape that delimits the subarea *A2a*. The white polygon highlights the wood removal area in *A2b*.

The same procedure is followed also for *A3a* and *A3b* and is illustrated in Figure 23.

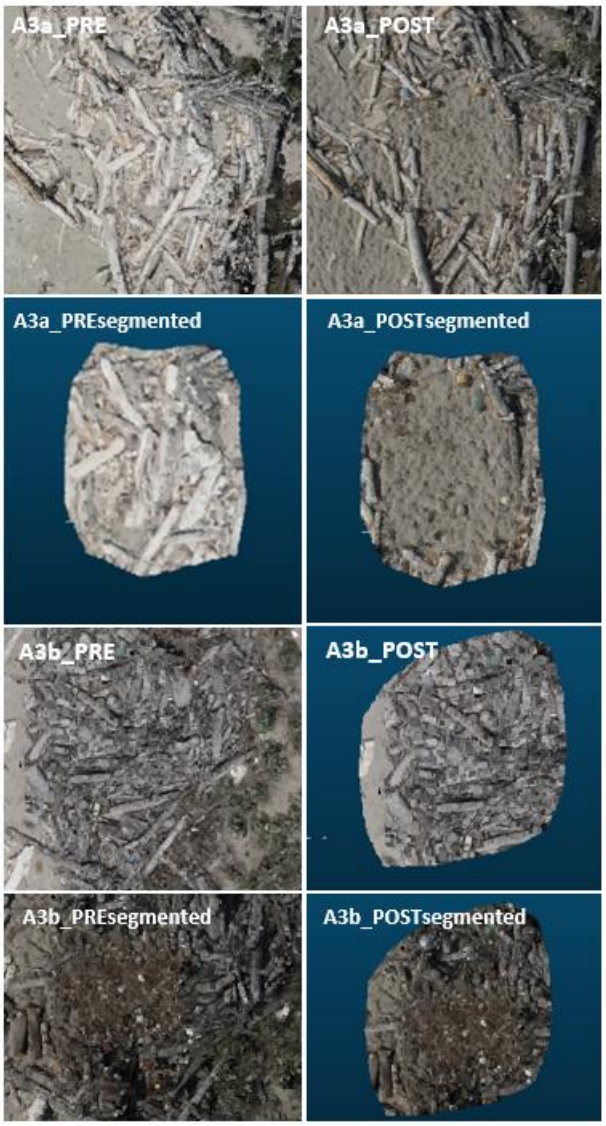

Figure 23. Segmentation of *A3a, A3b* from the photogrammetric dataset.

4.2.2. Automatic method applied on the raster files

In Cloud Compare, the command "Rasterize" generates a raster grid based on the following generation parameters in input:

- the desired grid step → 0,02 m;
- the projection direction → Z;
- the height to store among the ones of all points falling in that cell → maximum height.

No interpolation is done to fill the empty cells at this point. Once the base parameters are properly settled, and the "Update grid" button is clicked, CloudCompare computes and displays the grid.

The raster files *_PRE* and *_POST* just created are used in QGIS software. The "Volume Calculation Tool" is downloaded from the Plugin and is then shown in the curtained window "Raster," from where it is selected. The identification of a polygon to apply the calculation is required; as a consequence, a new shapefile layer is generated.
At this point, with a sampling step size of 0,02m, the tool calculates the volume of a *_PRE* area with respect to the correspondent reference layer *_POST*.

4.2.3. Manual method applied on the raster files

The raster files *_PRE* and *_POST* are loaded in QGIS software and is used the "Raster Calculator" to create a new raster, performing the operation:

$$V_{cell} = \Delta H_{(PRE-POST)} \times 0{,}02^2 \text{ [2]}$$

The height is multiplied by the cell's area for each cell, so the result is the added volume of wood for each cell.

To get the total volume of wood over the subarea, the sum of all these volumes per cell is calculated. In the Processing Toolbox is selected the "Raster Statistics" that allows to read a sum, which represents the total volume:

$$V_{tot} = \sum_{cell} V_{cell} \text{ [3]}$$

4.3. CWD volume calculation method choice and CWD density calculation

Among these methods, 4.1.1. Automatic method applied on the point cloud is chosen to retrieve the density of the wood deposit because it does not require the rasterisation of the data, instead works directly on the photogrammetric point clouds.
Then, the density is calculated as:

$$\rho = \frac{W}{V} \text{ [4]}$$

Where W is the weight in Table 2 measured during the survey, following the procedure explained in Chapter 4.1.3. ; and V the volume calculated. The formula calculates an apparent density for each of the two subareas, ρ_{A2a}, ρ_{A2b}, $\rho_{A3a,}$ and ρ_{A3b}. A partial mean density for each large area is computed ρ_{A2} and ρ_{A3}. This choice is based on considerations concerning geography, location, and the different visual characteristics of the deposit. In fact, is observed that *A2a* and *A2b* are characterised by a dense accumulation of smaller

woody debris, whereas in *A3a* and *A3b,* bigger logs spaced out by sandy voids are present. Two details are reported in Figure 24 to understand the difference in deposit.

Figure 24. *A2* wood is denser but smaller than *A3* logs.

4.4. Total CWD weight in *A2* and *A3*

Working on the entire large areas is performed the same process backwards. Having the densities ρ_{A2} *and* ρ_{A3} and applying method 1. Automatic method applied on the point cloud is chosen to calculate the volume of the large woody debris accumulation, the weight in kg of wood is estimated according to the equation:

$$W = \rho \times V \text{ [5]}$$

For what concerns the large areas is not directly available a *_POST* image. Therefore, the DTM is created, in CloudCompare, from the photogrammetric point cloud, visually classifying the ligneous pile and manually segmenting out those portions. This is illustrated, for the photogrammetric dataset, in Figure 25.

The decision is made to perform the classification manually instead of using an automatic classification algorithm. A first trial applying the CSF (Cloth Simulation Filter) does not lead to an accurate and relevant result despite changing the input parameters, such as the cloth resolution. The spectral response of wood is very similar to the

one of sand, and only RGB data are available. Therefore, CWD classification is performed manually.

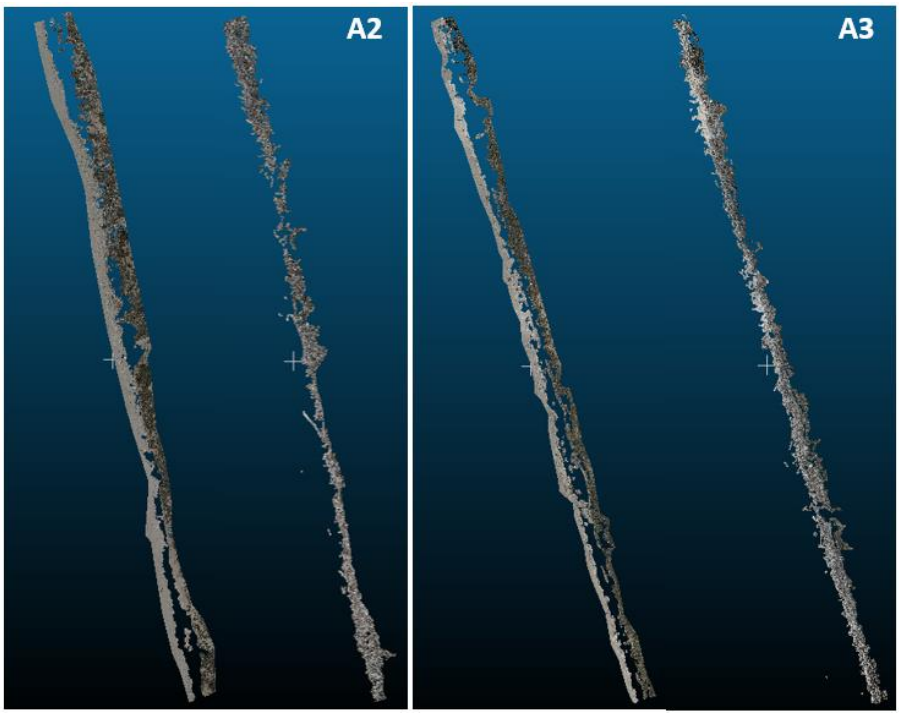

Figure 25. Segmentation of the CWD for *A2* and *A3* photogrammetric point clouds.

For both areas, on the right the CWD segmented out is shown. The remaining portion of sand and vegetation is placed aside, on the left. For the remaining terrain, a point cloud is created from the command "rasterise," filling the empty cells with the interpolated value.

Based on the segmentation of the photogrammetric dataset, the LiDAR dataset is segmented. Its visual classification is challenging as a consequence of the low point cloud density.

4.5. Conversion from weight to carbon stock

At this point, knowing the LWD weight along the large areas, a simple linear relationship taken from the literature is applied to convert the wood's weight into carbon stock.

$$C_{stock} = 50\% \times W \text{ [6]}$$

The operation is performed two times, one for each dataset.

4.6. Statistical analysis of the photogrammetric and LiDAR datasets

The willing is to verify whether there is a relationship between a spatial statistics variable and a physical parameter. In particular, only the part including CWD is considered for the entire area.
Starting from the photogrammetric dataset, as the spatial variable is taken, the point cloud density and the apparent density of the wood deposit as the physical parameter. The point cloud density is computed in CloudCompare going in "Tools - Geometric features," fixing a radius (r = 0,09m). The number of neighbours, surface density, and volume density are loaded. These three are just different ways to express the same quantity. The number of neighbours [pt] estimates for each point the number of points N in a neighbourhood of radius r. Surface density [pt/m^2] and volume density [pt/m^3] are the number of neighbours, respectively, divided by the surface and volume containing the neighbours. Switching from RGB visualisation to Scalar Field, it is possible to display the point cloud density histogram.

Of this distribution, an approximate mean point cloud density is computed in Matlab by downloading the .txt file that stores the point cloud density values, among other data such as the point coordinates (X,Y,Z) and radiometric information.

Secondly, the same analysis is performed with the LiDAR dataset.

For both datasets, the ratio between the approximate surface density [pt/m^2] and the maximum surface density is computed as a representative value of the point cloud density. Such normalisation is necessary to compare areas in time and space.

In addition, for what concerns the LiDAR dataset, the correlation between intensity and wood density is analysed. The goal is to distinguish wooden pieces of different dimensions or parts of the accumulation with different characteristics, one from another.

5. Results

This chapter illustrates the results corresponding to the tasks methodologies already developed in Chapter 4.

5.1. CWD volume calculation scenarios for the subareas *A2a*, *A2b*, *A3a*, A*3b*

The concept behind the three methods applied for the wood volume calculation is the same; however, the outcomes differ slightly. This could be due to the different approximations that the software algorithms compute.

5.1.1. Automatic method applied on the point cloud

The Volume Calculation tool used in CloudCompare requires a grid step that is settled equal to 0,1m. Such a grid is loaded on the right space of the tool window, and it is reported as an example for the photogrammetric dataset in Figure 26. It highlights in red the relative height that represents the volume of wood removed from the *_PRE* image. The relevant volumetric result of this method for the photogrammetric dataset is also reported in Figure 26.

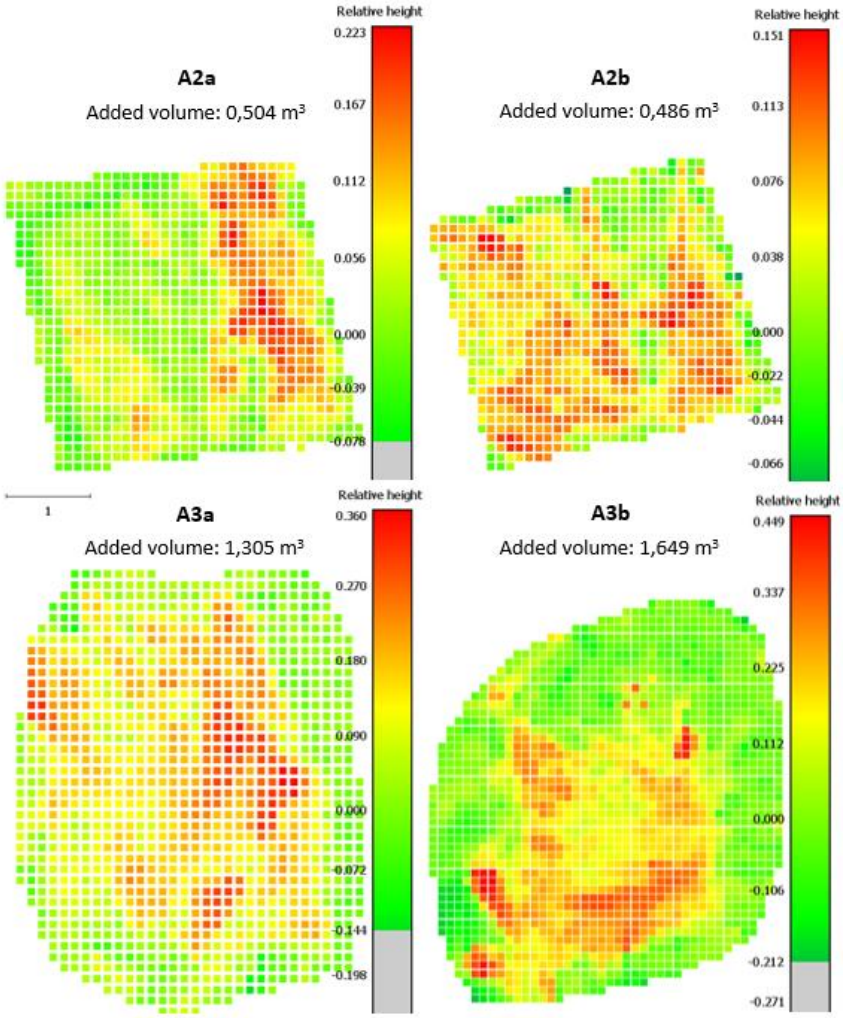

Figure 26. Relative height in the Volume Calculation tool for the photogrammetric segmented subareas.

The same methodology is used for the LiDAR data, for which results are directly reported in the summary Table 4.

5.1.2. Automatic method applied on a raster file

After the settling of the input parameters, as it is illustrated in paragraph 4.1.2.; the raster volume calculation tool is launched. On the right of the tool window, it is possible to read the inputs height layer *_PRE* and base layer *_POST*, used as DEM. This is illustrated in Figure 27 for the photogrammetric data. In addition, the volume results are pointed out by the red arrow.

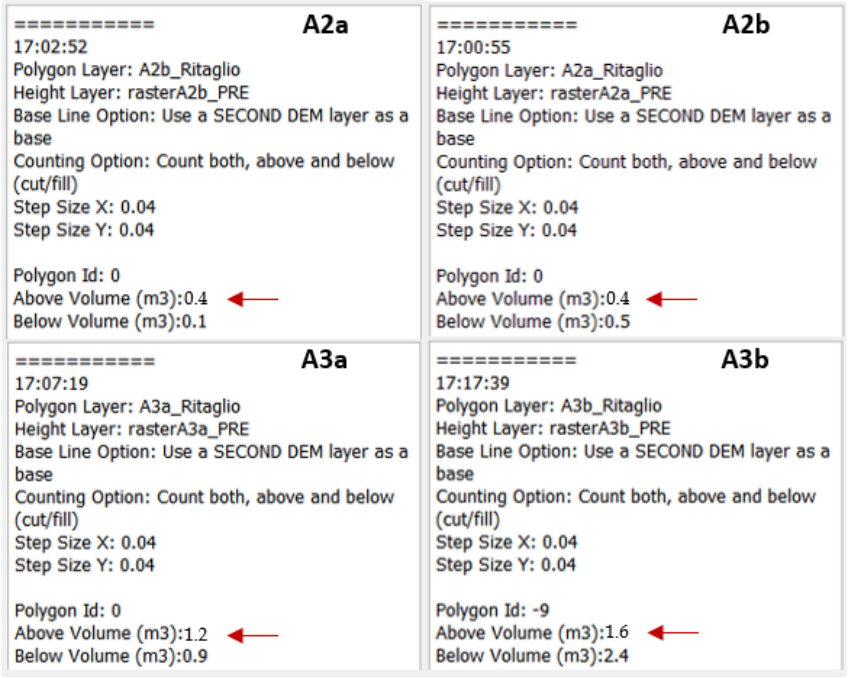

Figure 27. QGIS Volume calculation tool results log for the photogrammetric segmented subareas.

Results with the LiDAR data are directly reported in the summary Table 4.

5.1.3. Manual method applied on a raster file

The methodology illustrated in paragraph 4.1.3. is applied.

Figure 28 shows the significant volume raster file retrieved from the photogrammetric data. Each image contains the removed volume of wood in the *_POST* raster, with respect to the *_PRE* one. Indeed, the reddish parts are wood cumuli. Darker the color in a part of the image, the greater the volume of CWD in that area.

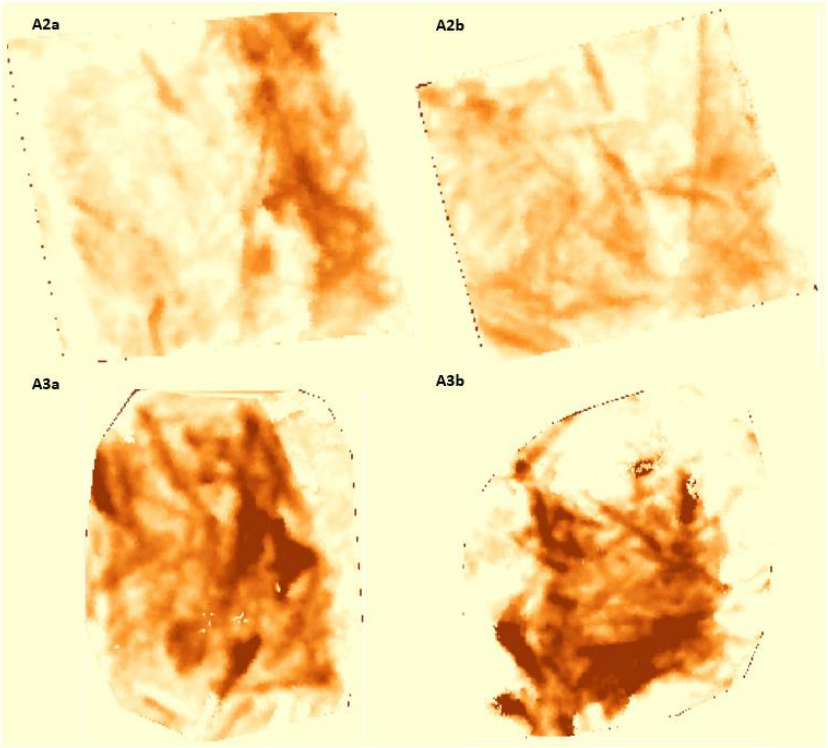

Figure 28. Raster file from the photogrammetric data showing the CWD.

Performing the summation over all cells, the result of the current method is directly illustrated in Table 4, for the photogrammetric and the LiDAR data.

CWD volume calculation results for each method applied and for each subarea are summarised in Table 4.

Photogrammetric dataset				
METHOD	V_{A2a} [m^3]	V_{A2b} [m^3]	V_{A3a}[m^3]	V_{A3b}[m^3]
1.	0,504	0,486	1,305	1,649
2.	0,400	0,400	1,200	1,600
3.	0,364	0,359	1,072	1,309
LiDAR dataset				
METHOD	V_{A2a} [m^3]	V_{A2b} [m^3]	V_{A3a}[m^3]	V_{A3b}[m^3]
1.	0,374	0,103	0,681	0,832
2.	1,300	2,600	4,800	3,400
3.	1,145	1,425	2,842	2,648

Table 4. The volume of CWD in [m^3] calculated in *A2a*, *A2b,* and *A3a*, *A3b* according to methods: 1. Automatic method applied on the point cloud; 2. Automatic method applied on the raster file; 3. Manual method applied to the raster file. Results are shown for the photogrammetric and the LiDAR data.

5.2. CWD volume calculation method choice and CWD density calculation

In Table 4, the highlighted lines correspond to the chosen method's volumetric results calculated with the photogrammetric and the LiDAR data. Consequently, the density is retrieved from the volume and weight of the CWD.

The motivation behind the volume calculation method choice is reported in the discussion in Chapter 6.2.

Useful data for this calculation are all reported in Table 5.

Photogrammetric dataset				
RESULTS	**A2a**	**A2b**	**A3a**	**A3b**
Weight [kg]	59,30	49,80	226,24	190,74
Volume [m^3]	0,504	0,486	1,305	1,649
Density [kg/m^3]	98,810	122,016	173,364	115,670
Partial mean density [kg/m^3]	110,413		144,517	
LiDAR dataset				
RESULTS	**A2a**	**A2b**	**A3a**	**A3b**
Weight [kg]	59,30	49,80	226,24	190,74
Volume [m^3]	0,374	0,103	0,681	0,832
Density [kg/m^3]	143,516	575,728	332,217	229,255
Partial mean density [kg/m^3]	359,622		280,736	

Table 5. Weight [kg], Volume [m^3] Density [kg/m^3] for *A2a, A2b, A3a,* and *A3b,* and Partial Mean Density [kg/m^3] for *A2* and *A3.* Results are shown for the photogrammetric and the LiDAR data.

5.3. Total CWD Weight in *A2* and *A3*

Having the partial mean densities previously calculated, ρ_{A2} and ρ_{A3}, the total volume of CWD in *A2* and *A3* are computed in CloudCompare with method 1.

The total weight resulting is tabled in Table 6.

Photogrammetric dataset			
Area	**Partial mean density [kg/m^3]**	**Volume [m^3]**	**Weight [kg]**
A2	110,413	812,867	89.751,084
A3	144,517	701,865	101.431,424
LiDAR dataset			
Area	**Partial mean density [kg/m^3]**	**Volume [m^3]**	**Weight [kg]**
A2	359,622	409,311	147.197,240
A3	280,736	836,484	234.831,172

Table 6. Total CWD weight [kg] calculated from the photogrammetric and LiDAR data in *A2* and *A3.*

5.4. Conversion from weight to carbon stock

Applying 50% as the conversion factor, the resulting carbon stock is illustrated in Table 7.

Photogrammetric dataset	
Area	**Carbon stock [kg]**
A2	44.875,539
A3	50.715,728
LiDAR dataset	
Area	**Carbon stock [kg]**
A2	73.598,620
A3	117.415,586

Table 7. Carbon stock [kg] calculated from the photogrammetric and LiDAR data in *A2* and *A3*.

5.5. Statistical analysis of the photogrammetric and LiDAR datasets

For the photogrammetric and the LiDAR dataset, the point cloud density histogram is plotted and shown in Figure 29 for *A2* and *A3*. Volume density and surface density are taken as representative of the density to compare values. Comparing the output with the one resulting from CloudCompare, from the photogrammetric point, cloud density low values seem to correspond to the borders of the segmentation. As a consequence, the data file is reduced, eliminating values lower than a threshold. Similarly, the LiDAR dataset is subsampled because high values correspond to the sandy or vegetated parts, which are not of interest.

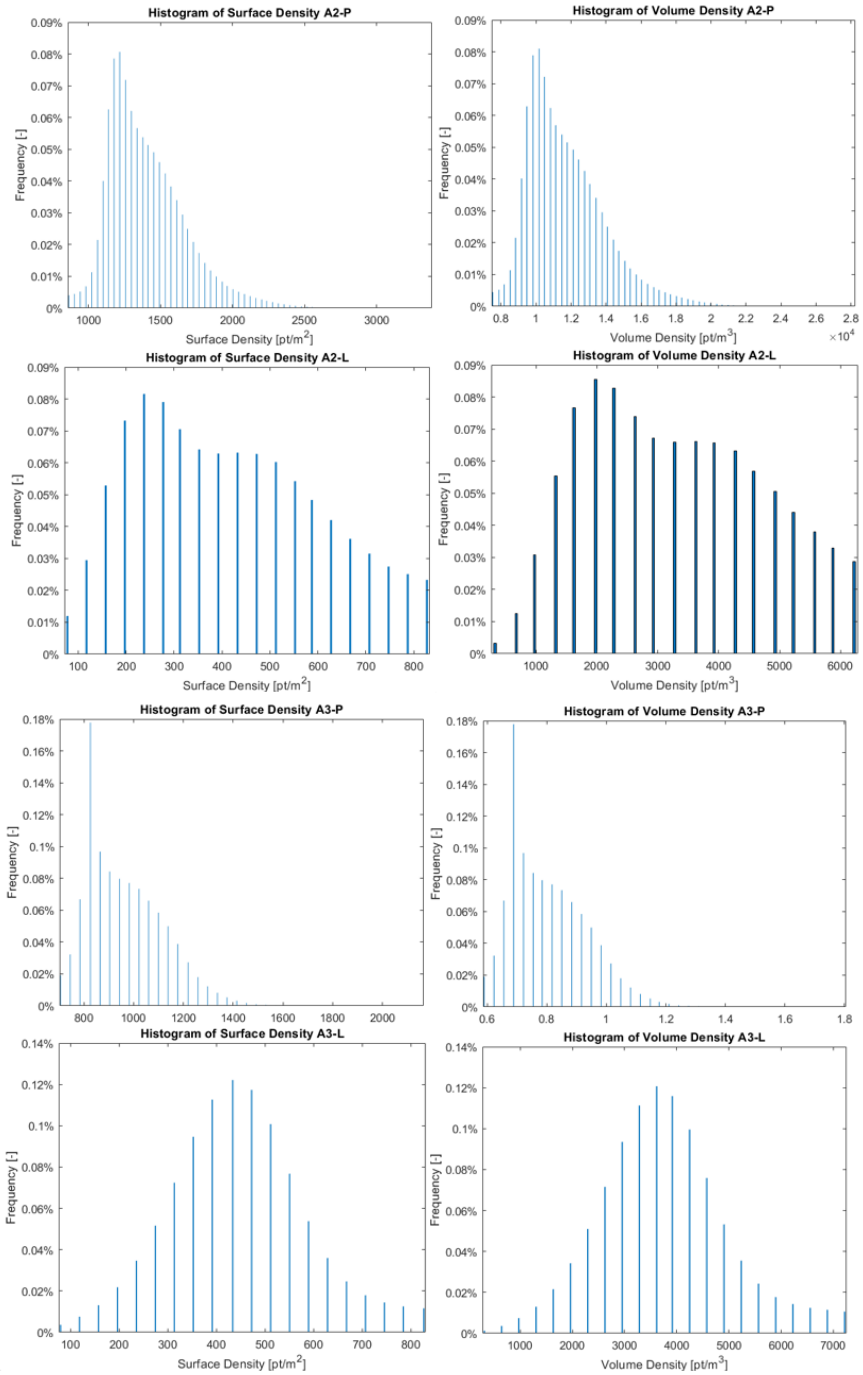

Figure 29. Point cloud density histogram.

The approximate mean is evaluated as the sum of the relative frequencies of each histogram's bar, calculated as the mean value of the histogram's bar time, the bar's frequency, divided by the sum of all the frequencies. Results are reported in Table 8.

POINT CLOUD DENSITY APPROXIMATE MEAN				
	Photogrammetric dataset		LiDAR dataset	
Area	Surface density [pt/m^2]	Volume density [pt/m^3]	Surface density [pt/m^2]	Volume density [pt/m^3]
A2	1403,3	11202,0	416,4	3291,8
A3	962,0	8021,2	474,2	3748,7

Table 8. Point clouds approximate mean.

To verify the correctness of the result, this approximate mean is compared to the mean value. It follows Table 9 with the same structure as the previous Table 8 but contains the mean value computed as the sum of all numbers divided by the total number of data in the sample.

POINT CLOUD DENSITY MEAN VALUE				
	Photogrammetric dataset		LiDAR dataset	
Area	Surface density [pt/m^2]	Volume density [pt/m^3]	Surface density [pt/m^2]	Volume density [pt/m^3]
A2	1403,7	11716,0	416,0	3292,2
A3	962,5	8020,7	445,9	3749,0

Table 9. Point clouds mean value.

In Table 10 is reported the surface density normalised for both datasets and areas.

NORMALIZED SURFACE DENSITY		
Area	Photogrammetric dataset	LiDAR dataset
A2	0,4153	0,5046
A3	0,4452	0,5421

Table 10. Normalized surface density for the photogrammetric and the LiDAR data.

Furthermore, the intensity histogram of the LiDAR data is plotted for *A2* and *A3* and illustrated in Figure 30.

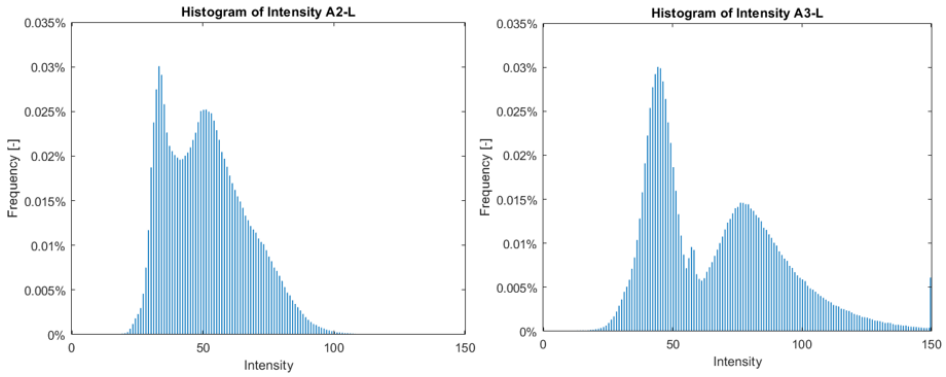

Figure 30. LiDAR intensity histogram.

6. Discussion

6.1. CWD volume calculation scenarios for the subareas *A2a*, *A2b*, *A3a*, A*3b*

To visualise the results, from data in Table 4, are constructed the plots in Figure 31, for the photogrammetric data and in Figure 32, for the LiDAR data. The three different symbols characterize each of the methods applied for the CWD volume calculation. Method 1. Automatic method applied on the point cloud is represented by the cyan star; method 2. Automatic method applied on the raster file, by the magenta triangle and method 3. Manual method applied on the raster file by the green plus.

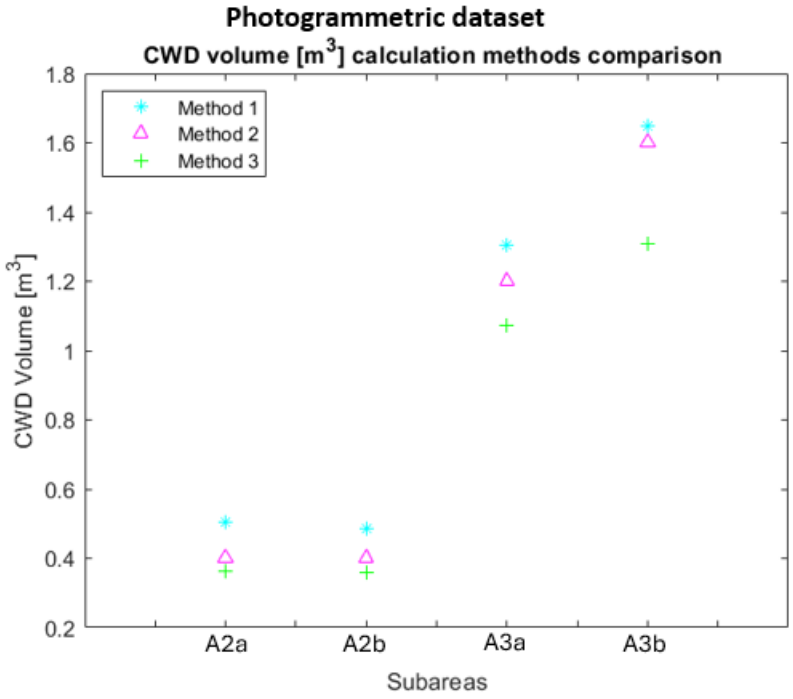

Figure 31. Photogrammetric dataset CWD volume [m^3] methods comparison for the subareas *A2a*, *A2b* and *A3a*, *A3b*. The cyan star represents method 1. Automatic method applied on the point cloud; the magenta triangle illustrates method 2. Automatic method applied on the raster file, and the green plus is method 3. Manual method applied to the raster file.

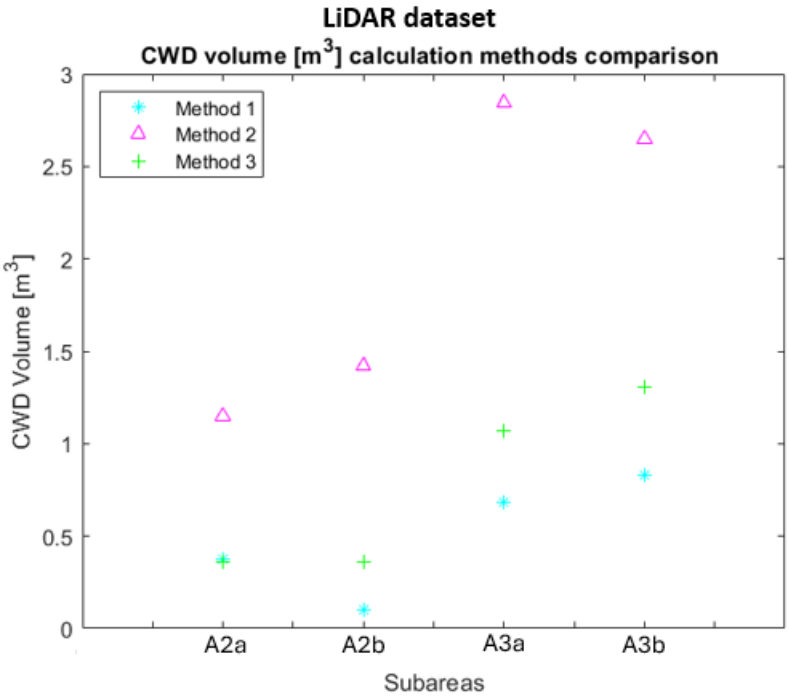

Figure 32. LiDAR dataset CWD volume [m³] methods comparison for the subareas *A2a*, *A2b* and *A3a*, *A3b*. The cyan star represents method 1. Automatic method applied on the point cloud; the magenta triangle illustrates method 2. Automatic method applied on the raster file, and the green plus is method 3. Manual method applied to the raster file.

Focusing first on the photogrammetric dataset CWD volume methods comparison in Figure 31, it is noticeable that the volume of CWD in the subareas calculated with the three methods 1, 2, and 3 is slightly different but still comparable.

The numbers obtained applying 1 and 2 are similar but still not coincident from one to the other. Indeed, both use an automatic volume calculation tool; however, belonging to different software, CloudCompare, and QGIS software.

Method 3, the manual method applied on the raster file, is rejected for multiple reasons. Starting from the evidence that its result diverges from the other two. In particular, it tends to underestimate the volume with respect to the other two methodologies. This is

related to the fact that through the rasterisation procedure, information is inevitably lost. Following by the fact that method 3 requires additional software compared to method 1, which uses only CloudCompare and a longer computational time than 1 and 2, which are instead automatic approaches.

For what concerns the LiDAR dataset the CWD volume methods comparison is shown in Figure 32. It is important to point out once again that the sparse nature of this point cloud leads to a quantitative LWD volumetric estimation that must be taken cautiously. In the computation of method 1, it appears the warning "At least one of the point clouds is sparse! You should fill the empty cells," however, even interpolating, the result remains approximate. Indeed, the behaviour among the methodologies does not coincide with the one of the photogrammetric data. Method 2 tends to overestimate with respect to the others.

It is possible to conclude that both the point cloud density used in the computation and the algorithm applied impact the result obtained.

6.2. CWD volume calculation method choice and CWD density calculation

Summing up the considerations of the previous chapter 6.1.; method 1, the automatic method applied on the point cloud is chosen because:

- it is easily applicable;
- it is automatic, consequently computational time is shorter than a manual method;
- it uses CloudCompare as the only software, whereas the other two require also QGIS software;
- it works directly on the point cloud without losing information during the rasterization procedure.

The density calculation depends on weight data retrieved during the in situ survey and on volume calculation performed through geomatics tools.
The weighting procedure, explained in detail in the methodologies chapter 4.1.3., is strictly related to the visual, subjective evaluation of the CWD to be taken into account. There were logs completely or partially submerged by the sand and deciding which to consider superficial was equivocal.
Moreover, even trying to precisely remove the sand from wood pieces, it is unrealistic to think that the sand was eliminated, given the roughness of the wood itself and the humid terrain.

For what concerns the volume calculation, it is performed from point clouds and even if minimal, also the reconstruction procedure accuracy of the could affect the final result.

Figure 33 compares the results obtained by applying the chosen LWD volume calculation method 1 using the photogrammetric and the LiDAR data. In the graph, blue dots represent the CWD volume obtained from the photogrammetric data, whereas the red cross marks illustrate the LiDAR results.

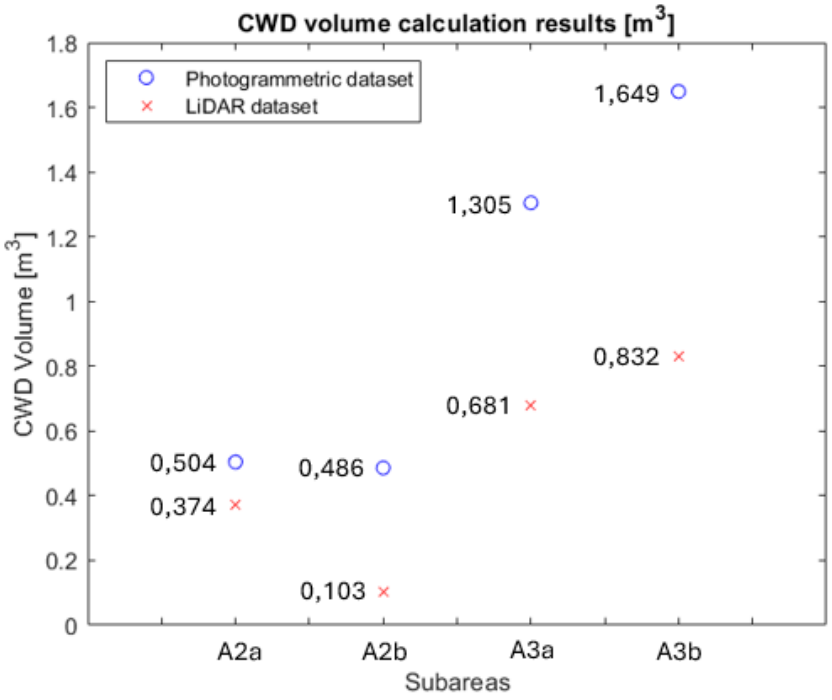

Figure 33. The volume of CWD in [m³] calculated in *A2a*, *A2b,* and *A3a*, *A3b* according to method 1. Automatic method applied on the point cloud 2. Automatic method applied on the raster file; 3. Manual method applied to the raster file. Results are shown for the photogrammetric and the LiDAR data.

In general, it is noticeable that the distribution of the point cloud affects the wood volume estimation. In a sparse point cloud such as the LiDAR punctual information is lost, and CWD pieces could not be recognised, especially in subareas characterized by a deposit of smaller wooden material; especially because method 1 does not apply further operations on the input data.

The weight measured, the volume calculated and consequently the density values retrieved, shown in Table 5 are quite different from one subarea to another. The LWD accumulation in the subareas are visually dissimilar, as Figure 22 and Figure 23 show. In particular, in *A2a* and *A2b* the woody material is of smaller dimension and quite concentrated. Instead in *A3a,* there are bigger logs interspersed with

sand. *A3b* is similar to *A3a* but has fewer and smaller voids among logs.
Intuitively, whether the weight is high and the volume still low, the density results in a high value. As a consequence, going back to Table 5 to look at the numbers, the value of the apparent density in *A3a* is the greatest. On the contrary, especially in *A2a,* the apparent density results are low because both weight and volume are low.
As expected, it is possible to conclude that wood density depends on the deposit characteristics.

No information is available on the tree species of the coarse woody debris accumulation in the study areas targeted. It is assumed this parameter would not significantly affect the density result as well as knowing from where the wood is coming.

The results obtained in this study are compared to previous studies from the literature. Even though scientific articles on woody accumulation on the coast are rare, it is still possible to consult those based on biomass in other natural environments such as forests. Intuitively it is expected to find a lower density value for CWD at the seashore, given that the degradation process of the wood will be in different, more severe, conditions.
It is peculiar how the density value is strongly related to the degree of degradation expressed in terms of decay class, whose evaluation is not straightforward nor univocal. In all studies, the density is around 280 kg/m^3 considering a mean among decay classes two, three and four (Larjavaara and Muller-Landau 2010, Charles et al. 2016, Shorohova et al. 2022, Köster et al 2015).

A critical aspect to highlight is that it is not possible to know the exact CWD volume and consequently the site-specific wood density with the procedure applied in this study. The potential of indirectly retrieving these results is evident, however, such estimations are not validated through other procedures rather than the in situ visual inspection of the targeted area. It could be possible to expand the study evaluating the LWD density on-site through a specific procedure, among visual

decay classification, knife test, spring penetrometer, or dynamic penetrometer. This last method is considered to be the one that works best (Larjavaara and Muller-Landau 2010). Another possibility is to evaluate the density of wood samples in the laboratory.
Furthermore, it could be interesting to monitor the decay of standardized logs in the laboratory to build a quantitative description of CWD mass loss in time.

6.3. Total CWD Weight in *A2* and *A3*

In this step, an important aspect to point out is that to create the DTM of the two large areas, a manual classification of what is wood is performed from what is not in the photogrammetric image.
A possibility to get a more precise DTM is to increase the accuracy of the classification of woody debris from other materials such as sand, vegetation, or plastic. This could be done by trying to use other automatic classification tools.
Indeed, a major challenge in the application of remote sensing techniques is the lack of a fundamental understanding of materials' behaviour along the spectrum to incident electromagnetic radiation, the so-called spectral signature. As a consequence, future development of this study could include the training of the sensor in the laboratory in extracting wood from sand or other vegetation that have all quite similar spectral signatures.

Nevertheless, these first results show that other information can be included in the classification procedure. For example, considering the intensity of the LiDAR point cloud could help in classifying CWD. Moreover, improving the accuracy of the point clouds by performing high-resolution flights, with low flight height and low flight speed, could help in better describing the geometry of the LWD.

Furthermore, the choice of taking two partial mean densities is related to the fact that from visual analysis of the areas, from the two photogrammetric point clouds, it is observable that in *A2* the CWD deposition seems to be more dispersed and mixes with other materials, for example plastic debris, whereas in *A3* is more

continuous and localized. Indeed the resulting weight is higher in *A3* than in *A2*.

A possible upgrade to improve the result's precision could be classifying CWD in classes according to the CWD size and associating a specific density value to each class. It is noticed that the dimension of the logs present influences wood density values among the four subareas. Areas with CWD of greater dimensions are linked to a higher LWD density.

6.4. Conversion from weight to carbon stock

In the step from wood weight to Carbon content is taken 50%, which is the default conversion factor representing the average carbon content in biomass according to the IPCC. In general, this percentage of carbon in biomass ranges between 35÷65% of the dry weight.
Although studies (Martin et al. 2018, 2021) suggest that this number overestimates carbon, the 2019 Refinement to the 2006 IPCC Guidelines for National Greenhouse Gas Inventories included no updates to this default dead wood carbon fraction.
This conversion factor is not a constant. It should vary significantly among decay classes, wood type characteristics, and location of the case study.

Returning to Table 7 and comparing the carbon obtained in both areas from the photogrammetric data to the one retrieved from the LiDAR data values are almost doubled. Overall, the results obtained from both datasets agree on the *A3* LWD deposit being a greater carbon pool.

6.5. Statistical analysis of the photogrammetric and LiDAR datasets

In this specific case, the photogrammetric point cloud density is higher than the LiDAR one. Such a thing was discussed previously and shown in Figure 21.

This leads to the question of which aspect influences such parameters. For sure flight characteristics have a crucial role, among which the flight height. Increasing the flight height, the density of the resulting point cloud decreases.

Just looking at the plots in Figure 29, it is noticeable how photogrammetric and LiDAR point cloud densities distributions are different in shape and value ranges. Despite the LiDAR point cloud density of *A3* that looks like a gamma distribution, the behaviour of the fitting curves is not directly related to one of the common probabilistic models.
Moreover, comparing the scalar field point cloud density and the RGB image, there is no correlation between the point cloud density and the physical density of the LWD. This comparison is performed only with the photogrammetric dataset because the LiDAR image has a point cloud density so low that it is not possible to well recognise objects visually.
As an example, Figure 34 illustrates a portion of the *A2* photogrammetric dataset. In the RGB image, on the right, is highlighted in white a big log which is not detectable for the scalar field showing the Volume Density of the same part of the area, reported on the left. Further studies would be necessary to conclude whether or not a correlation between the density of the photogrammetric or the LiDAR point cloud and the density of the wooden deposit is present.
Up to now, it does not seem so.

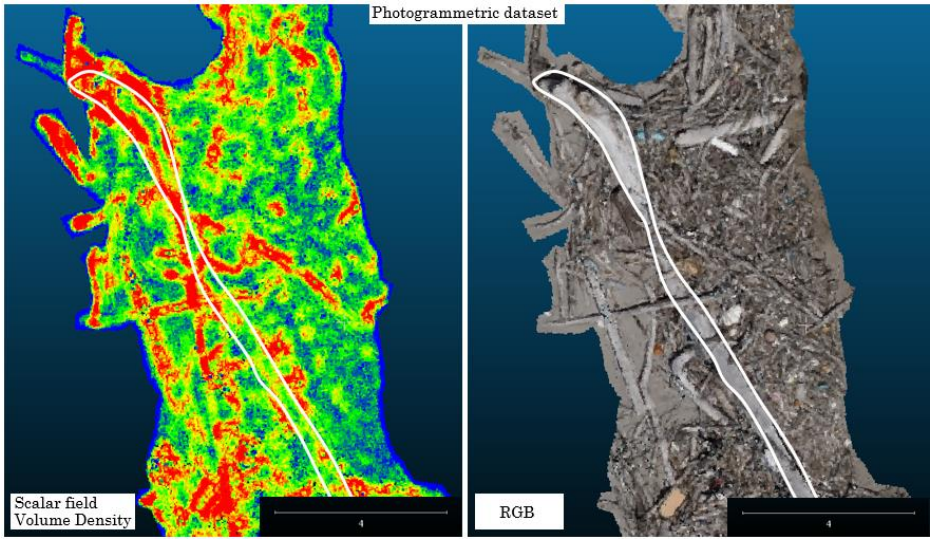

Figure 34. Volume Density and RGB comparison.

Worth noticing from Figure 34 is that the borders of the CWD accumulation are all characterized by the blue colour, meaning that the Volume Density is low in that region. This is probably a consequence of the segmentation procedure. This leads to the choice of discarding very low point cloud density values in the histogram and, consequently, in the evaluation of the approximate mean point cloud density.

As expected, a greater point cloud density may correspond to higher elevation points in space. Alternatively, it might be the lateral part of a log, which is not visible from the sensor since no oblique images were collected.

In Table 8, the approximate mean calculated confirms that the photogrammetric dataset is more accurate and its point cloud density is more than three times the one of the LiDAR dataset. Table 10 includes the normalized surface density for the photogrammetric and the LiDAR data. The two areas, A2 and A3, have comparable values. It means that considering a data collection technique, photogrammetry or LiDAR, the spatial arrangement of points in the two point clouds is similar. Potentially, these values could be relevant for comparison with further studies.

In addition, for the LiDAR dataset also the intensity distribution is plotted.
It is relevant to observe that a correlation between intensity value and log characteristics is possible.
In CloudCompare, visually looking at the scalar field intensity image and at the RGB one, for both *A2* and *A3* point clouds, to higher intensity values logs of bigger dimensions are related. On the contrary, low-intensity values correspond to voids among CWD cumuli, so basically sand or vegetation. An intermediate-range represents areas that have a more or less dense accumulation of small woody debris.
Regulating saturation from the image properties window in Cloud Compare, the portion of LiDAR point cloud in Figure 35 well represents what has been just explained. For example, on the bottom left, there is a circular shaped sandy part, among logs, clearly coloured blue. While the log on the top left is coloured in red.

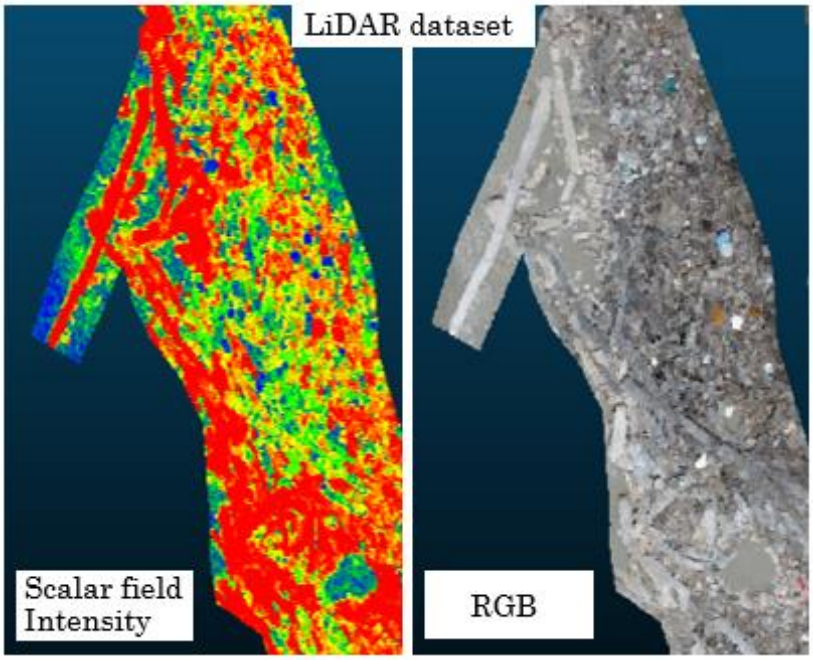

Figure 35. LiDAR intensity and RGB comparison.

In particular, Table 11 summarizes the intensity ranges coloured differently, which are analogous for *A2* and *A3*.

LiDAR intensity	Scalar field observation	RGB observation	A2 and A3 Intensity values
High	RED	Big logs, dense areas	**Intensity > 70**
Intermediate	GREEN	Woody debris, less dense areas	**50 < Intensity < 70**
Low	BLUE	Sand, vegetation	**Intensity < 50**

Table 11. LiDAR point cloud intensity correlation to CWD deposit characteristics.

Moreover, the RGB is shown in the left image of Figure 36. In the image, there is a visible blue plastic piece which is not particularly recognised as a different material in the left image that describes again the scalar field intensity of the LiDAR camera. This aspect is noted all over the image whether there is debris of different nature rather than wood. Such observation may lead to the conclusion that the properties of the two objects as a response to incident electromagnetic radiation are not so different one from the other.

All considered this correlation between LiDAR intensity and CWD deposit characteristics could be used in the future to build a more accurate and realistic volumetric model, better recognising sandy portions among logs in the accumulation.

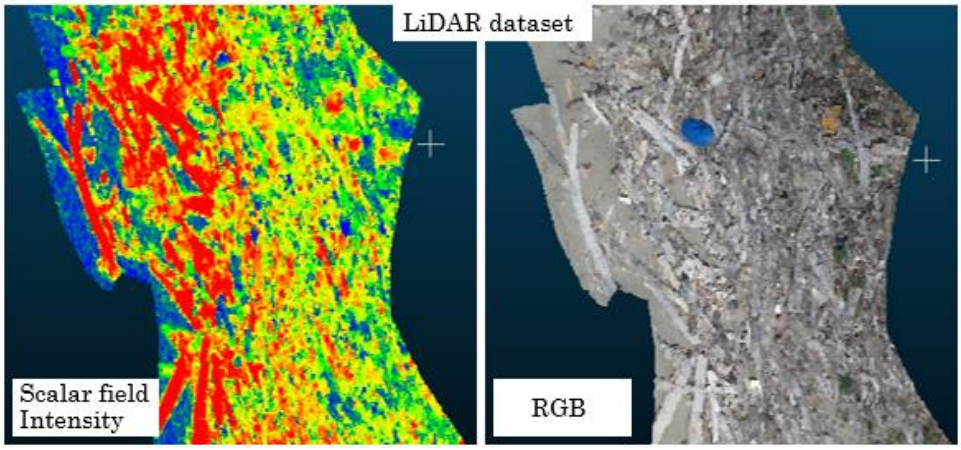

Figure 36. LiDAR intensity and RGB comparison, detail on plastic debris.

7. Conclusions

This study analyses the role of coarse woody debris both as the base structure for dynamic coastal dunes systems and as relevant carbon stock. Understanding the global carbon cycle is impossible without estimates of carbon stocks in coastal marine ecosystems. In fact, not only CWD itself is an important carbon pool but, it also significantly influences the carbon stock in soil undergoing decomposition and humidification processes. To assess the dead wood contribution to the total coastal carbon pool, it is necessary to convert dead wood volumes into biomass by using density values.

This case study analyses the CWD carbon stock in *A2* and *A3* areas along the backshore in San Rossore Regional Park, in Italy, Tuscany (PI). During a field survey in the larger areas *A2* and *A3*, four subsampled areas are delimited, *A2a, A2b* and *A3a, A3b*. A first aerial photogrammetric and LiDAR campaign is performed. Then, CWD is weighted and removed from the subsampled areas, and a second aerial photogrammetric and LiDAR campaign is conducted. CWD volumes are calculated using geomatics tools thanks to the 3D reconstructions of the areas modelled before and after the wood removal. Three different indirect methods (Table 3) are applied to work on the photogrammetric and the LiDAR point clouds in Cloud Compare and QGIS. The automatic volume calculation method applied on the point cloud is chosen among these. With weight and volume for each subarea, is calculated the density. To retrieve a density result for *A2* and *A3* two partial mean densities (Table 5) are estimated. The CWD resulting volume in *A2* and *A3* (Table 6) is retrieved by applying the same volume calculation method used for the subsampled areas. This time the creation of the DTM is needed, which is performed through visual segmentation of the CWD region, cutting out whatever is sand or vegetation.
With density and volume, the total LWD weight in the large areas *A2* and *A3* is calculated, and subsequently, it is converted into carbon content by applying the 50% average conversion factor from biomass to carbon (Table 7).

The conclusion is that it is possible to develop and use geomatics tools for volumetric estimations in natural environments.

Moreover, the quality and accuracy of the photogrammetric and the LiDAR dataset are analysed. The volumetric estimates using the photogrammetric point cloud are confirmed to be more reliable by comparing the mean point cloud densities. Indeed, the photogrammetric point cloud density results are significantly higher than the LiDAR dataset, which is sparser (Table 8, Table 9). This statistical information of the datasets is correlated with the physical density of the CWD deposit. It seems that there is no correlation between point cloud density and the physical apparent density of the wood accumulation.
Instead, a good correlation between the LiDAR datum's intensity and the CWD's characteristics is visible. In particular, logs of bigger dimensions are related to higher intensity values. On the contrary, low-intensity values correspond to voids among CWD cumuli, sand, or vegetation. An intermediate range represents areas that have a more or less dense accumulation of small woody debris (Table 11).

As a whole, the study shows promising results. It is a starting point of a continuative much larger research.

8. Future developments

After the analysis of existing literature and the research conducted in this work, potential future developments that arise are to:

- improve the accuracy of the point cloud performing high-resolution flights (low flight height and low flight speed) to better describe the geometry of the LWD;
- build a more accurate and realistic volumetric model. Better extract wood from sand and vegetation, using the observed correlation between LiDAR intensity and CWD deposit characteristics;
- improve the precision of the result by classifying CWD in classes according to the size and associating a specific density value to each class;
- gather information on the spectral signatures of wood, sand, and vegetation by training the sensor in the laboratory;
- use other automatic classification tools than CSF to extract wood;
- validate the density estimation through other procedures than in situ visual inspection of the targeted area (decay classification, knife test, spring penetrometer, or dynamic penetrometer);
- monitor the decay of standardized logs in the laboratory to build a quantitative description of CWD mass loss in time due to weathering in the marine environment;
- take core samples of sand to investigate the carbon stock buried;
- investigate the frequency and magnitude of the wave-induced erosional (LWD exposing) and aeolian depositional (LWD burying) events to situate the volumetric sand changes within the overall wave and wind process regimes;
- determine the main factors that drive the beach-dunes system variability in the study area and examine the sand volumetric changes at the site to determine if there is a correlation with CWD deposit
- apply spatial statistics to ground the coastline temporal and spatial analysis statistically.

8.1. Coastline temporal evolution

After the discussion on the beach-dune system dynamics and the possible progression or regression of the coastline as a consequence of the complex oceanic and atmospheric forcings interaction, discussed in chapter 2.5; it arises the idea to develop, in the future, a model capable of evaluating the quantitative volumetric modification of the woody debris deposit related to the coastline evolution.

For this purpose, it is essential to highlight that this analysis requires the strong assumption that these parameters remain invariant in time:

- sea storm dynamics;
- mean sea level;
- sediments transport dynamics;
- CWD deposition rate.

The following conceptual model in Figure 37 is developed to picture the reasoning better.
It shows that CWD acts as a basal structure for the further accretion of the dunes complex, ΔV_{CWD}, in association with the potential progress of the coastline Δx.

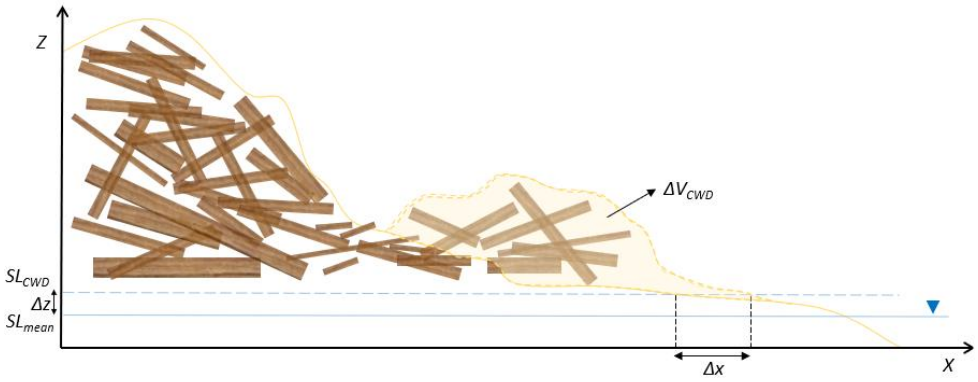

Figure 37. Conceptual model of the beach-dunes dynamics consequent to coastline evolution.

Δx is determined as the horizontal distance connecting two specific points. The "old" and the "new" interception, between the beach profile and the line from which the CWD deposition starts, correspond to a height SL_{CWD}. The influence of seawater, waves, and tide is negligible from this height.

A height, SL_{CWD}, above the mean sea water level from which the wood accumulation theoretically begins, is required. Such datum is retrieved from published data of the "Rete Mareografica Nazionale.

Specifically, Figure 38 illustrates the 2 cm resolution orthophotos of *A2* and *A3* in which, from left to right, the following profiles are reported for both areas:

- mean sea water level [m.slm] correspondent to the white dots and a value SL_{mean} = 0,48258 m.slm.
- 95 percentile sea water level [m.slm] illustrated in green. Such quantity, SL_{95} = 1,1505 m.slm, represents the value of the sea water level exceeded 95% of the times in a considered time interval of observations;
- maximum sea water level [m.slm] shown by the blue dots, equal to SL_{max} = 2,1531 m.slm;
- dune crest depicted by the red triangles.

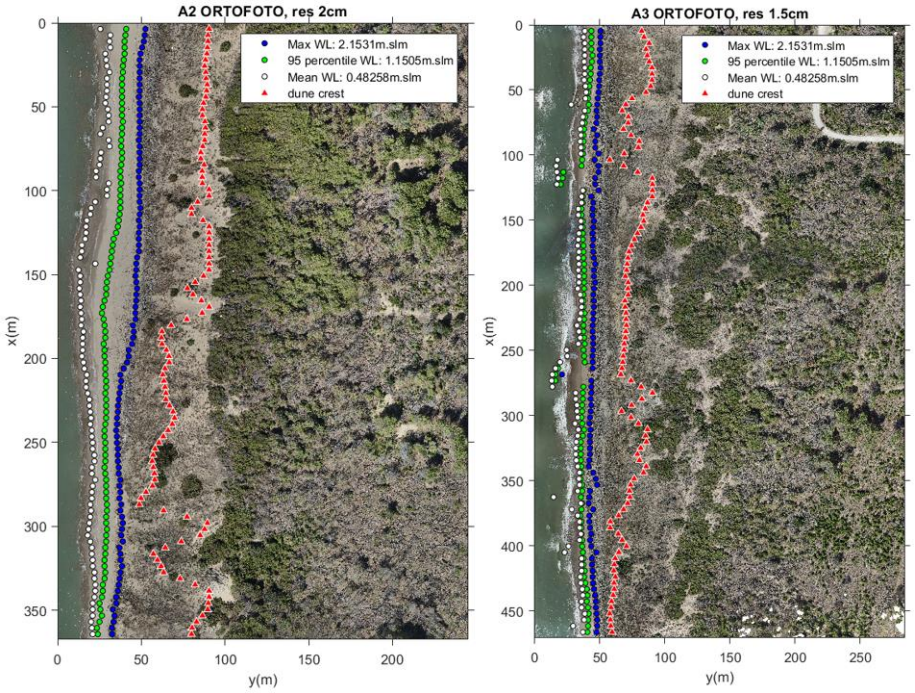

Figure 38. 2 cm resolution orthophotos of *A2* and *A3* reporting data from the "Rete Mareografica Nazionale". White dots are the mean sea water level, SL_{mean}; green dots are the 95 percentile sea water level, SL_{95}, blue dots are the maximum sea water level, SL_{max}, and red triangles represent the dune crest.

In particular, SL_{95} and SL_{max} are considered representative of the wave runup and highly relevant for the definition of SL_{CWD}.

With these data, the temporal evolution of the coastline could be studied by looking at satellite images from Google Earth Engine (GEE). This tool allows time series analysis on remotely sensed data, giving access to decades of imagery without the limitation of needing to download, organise, store, and process this information.

The volume corresponding to the horizontal progress of the coastline is approximately equal to the volume of the total CWD biomass accumulation: $\Delta Z_{CWD} \times \Delta x \times L$, with L length of the coastline considered, and height variation among years.

9. References

https://www.unep.org/

https://www.isprambiente.gov.it/contentfiles/00003500/3535-brecciaroli.pdf

https://www.parcosanrossore.org/

https://www.ces.fau.edu/nasa/module-2/how-greenhouse-effect-works.php

https://www.globalchange.gov/browse/indicators/atmospheric-carbon-dioxide

https://enterprise.dji.com/zenmuse-p1

https://enterprise.dji.com/zenmuse-l1

Rete Mareografica Nazionale:
https://www.mareografico.it/?session=0S10761218975V7369877089A&syslng=ita&sysmen=-1&sysind=-1&syssub=-1&sysfnt=0&code=STAZ&idst=1L

Aagaard T., Davidson-Arnott R., Greenwood B., Nielsen J.; *Sediment supply from shoreface to dunes: Linking sediment transport measurements and long-term morphological evolution*; Geomorphology, 60, 205–224, 2004. https://doi.org/10.1016/j. geomorph.2003.08.002

Adam P.; *Saltmarshes in a time of change*; Environmental Conservation 29, 39–61, 2002.

Andersson A. J., MacKenzie F. T. and Lerman, A.; *Coastal Ocean and carbonate systems in the high CO2 world of the Anthropocene*. Am. J. Sci. 305, 875–918, 2005.

Anthony E.J., Vanhee S., Ruz M.; *Short-term beach–dune sand budgets on the North Sea coast of France: sand supply from shoreface to dunes, and the role of wind and fetch*. Geomorphology 81, 316–329, 2006.

Armenio E., De Serio F., Mossa M., Nobile B., Petrillo, A.F.; *Investigation on coastline evolution using long-term observations and numerical modelling*; The 27th International Ocean and Polar Engineering Conference, International Society of Offshore and Polar Engineers, 25–30 June 2017, San Francisco, California, USA, 2017b.

Armenio E., De Serio F., Mossa M., Petrillo A. F.; *Coastline evolution based on statistical analysis and modeling*; Nat. Hazards Earth Syst. Sci., 19, 1937–1953, 2019. https://doi.org/10.5194/nhess-19-1937-2019

Aumont O. et al. *Riverine-driven interhemispheric transport of carbon*; Global Biogeochemical Cycles 15, 393–405, 2001.

Baltsavias E.; *A comparison between photogrammetry and laser scanning*; ISPRS J. Photogrammetry 54, 83–94, 1999.

Barry P., Coakley R.; *Accuracy of UAV photogrammetry compared with network RTK GPS*. Int. Arch. Photogrammetric Remote Sens. XL-1/W2, 27–31, 2013.

Bastviken D., Tranvik L. J., Downing J. A., Crill P. M. and Enrich-Prast A.; *Freshwater methane emissions offset the continental carbon sink*. Science 331, 50, 2011.

Battin T. J. et al; *The boundless carbon cycle*; Nature Geoscience 2, 598–600, 2009.

Bergsma E.W., Almar R.; *Coastal coverage of ESA'Sentinel-2 mission*; Advances in Space Research 65(11):2636-44, 2020.

Bianchi T. S.; *The role of terrestrially derived organic carbon in the coastal ocean: a changing paradigm and the priming effect*; Proc. Natl Acad. Sci. USA 108, 19473–19481, 2011.

Blair N. E. and Aller, R. C.; *The fate of terrestrial organic carbon in the marine environment*. Ann. Rev. Mar. Sci. 4, 401–423, 2012.

Blossier B., Bryan K. R., Winter C.; *Simple Pocket Beach Rotation Model Derived from Linear Analysis*, in: Proc. Coastal Sediments 2015, San Diego, USA, 2015.

Breithaupt J. L., Smoak J. M., Smith T. J., Sanders C. J., Hoare A.; *Organic carbon burial rates in mangrove sediments: strengthening the global budget*; Global Biogeochemistry. Cycles 26, GB3011, 2012.

Borges A. V., Delille B., Frankignoulle M.; *Budgeting sinks and sources of CO_2 in the coastal ocean: diversity of ecosystem counts*; Geophys. Res. Lett. 32, 1–4, 2005.

Brewer T.L.; *Climate Change Challenges*. Transforming U.S. Climate Change Policies. SpringerBriefs in Energy. Springer, Cham., 2022. https://doi.org/10.1007/978-3-030-99716-8_1

Brock J.C., Wright C.W., Sallenger A.H., Krabill W.B., Swift R.N.; *Basis and methods of NASA Airborne topographic mapper LiDAR surveys for coastal studies*; Journal of Coastal Research 18, 1–13, 2002.

Brown S.; Measuring carbon in forests: current status and future challenges; Environmental Pollution 116(3): 363–372, 2002. doi:10.1016/ S0269-7491(01)00212-3. PMID:11822714

Cai W. J., Dai M., Wang Y.; *Air-sea exchange of carbon dioxide in ocean margins: a province-based synthesis*. Geophysics Research Letter 33, L12603, 2006.

Cai W. J.; *Estuarine and coastal ocean carbon paradox: CO_2 sinks or sites of terrestrial carbon incineration?* Ann. Rev. Mar. Sci. 3, 123–145, 2011.

Chen J.F., Zhai W.D., Wang B., et al.; *A review of the carbon cycle in river estuary coastal ocean continuum*, Journal Marine Science; 39, pp. 11-21, 2021.

Christian E.; *Planning for the global earth observation system of systems (GEOSS)*; Space Policy; 21(2):105-9, 2005.

Ciccarelli D., Balestri M., Pagni A. M., Forino L.; *Morpho-functional adaptations in Cakile maritima Scop. subsp. maritima: Comparation of two different morphological types;* Caryologia - Firenze *-;* 63(4):411-421, 2010.

Collins W. J. et al.; *Development and evaluation of an Earth-system model - HadGEM2*. Geoscience Model Dev. Discuss. 4, 997-1062, 2011.

Copard Y., Amiotte-Suchet P. and Di-Giovanni C.; *Storage and release of fossil organic carbon related to weathering of sedimentary rocks*. Earth Planet. Sci. Lett. 258, 345–357, 2007.

Cotrim da Cunha L., Buitenhuis E. T., Le Quéré C., Giraud X., Ludwig W.; *Potential impact of changes in river nutrient supply on global ocean biogeochemistry;* Global Biogeochemical Cycles 21, GB4007, 2007.

De Serio F. and Mossa M.; *Streamwise velocity profiles in coastal currents*; Journal of Environmental Fluid Mechanics, 14, 895–918, 2014.

De Vries S., Arens S.M., De Schipper M.A., Ranasinghe R.; *Aeolian sediment transport on a beach with a varying sediment supply*; Aeolian Research, 15, 235–244; 2014. https://doi.org/10.1016/j.aeolia.2014.08.001

Debruyn W., Deronde B., Fransaer D., Henriet J., Houthuys R., Lancker V.V.; *Use of airborne hyperspectral data and laser scan data to study beach morphodynamics along the Belgian Coast;* Journal of Coastal Research 22, 1108–1117, 2006.

Degens E. T., Kempe S., Richey J. E.; *Biogeochemistry of Major World Rivers*; Wiley; 1991.

Dolan R., Hayden B.P., Felder W.; *Systematic variations in inshore bathymetry*, J. Geol., 85, 129–141, 1977.

Dolan R., Fenster M.S., Holme S.J.; *Temporal analysis of shoreline recession and accretion*, J. Coast. Res., 7, 723–744, 1991.

Donato D. C. et al.; *Mangroves among the most carbon-rich forests in the tropics*; Nature Geoscience 4, 293–297, 2011.

Douglas B.C. and Crowell M.; *Long-term shoreline position prediction and error propagation*; J. Coast. Res., 16, 145–152, 2000.

Duarte C. M., Middelburg J., Caraco N.; *Major role of marine vegetation on the oceanic carbon cycle;* Biogeosciences 2, 1-8, 2005.

Duarte C. M., Losada I. J., Hendriks I. E., Mazarrasa I., Marbà N.; *The role of coastal plant communities for climate change mitigation and adaptation*; Nature Climate Change, 2013.

Dunne J. P., Sarmiento J. L. and Gnanadesikan A.; *A synthesis of global particle export from the surface ocean and cycling through the ocean interior and on the seafloor*. Global Biogeochemical Cycles 21, GB4006, 2007.

Eamer J. B.R., Walker I. J.; *Quantifying sand storage capacity of large woody debris on beaches using LiDAR*; *ELSEVIER* Geomorphology 118, 33-47, 2010.

Eamer J. B.R., Walker I. J.; *Quantifying spatial and temporal trends in beach–dune volumetric changes using spatial statistics*; *ELSEVIER* Geomorphology 191, 94-108, 2013.

Eamer J.B.R., Walker I.J., Darke I.B.; *Geomorphic and sediment volume responses of a coastal dune complex to invasive vegetation removal: Wickaninnish Dunes, Pacific Rim National Park Reserve, British Columbia, Canada*. ResearchGate, 2013.

Eltner A., Kaiser A., Castillo C., Rock G., Neugirg F., Abel-lán A.; *Image-based surface reconstruction in geomorphometry– merits, limits and developments*, Earth Surface Dynamics, 4, 359-389, 2016. doi:10.5194/esurf-4-359-2016.

Energy Technology Perspectives. IEA, 2008

Fojutowski A., Wróblewska H., Komorowicz M., Kropacz A., Noskowiak A., Iwona Pomian I.; *Changes in the properties of English oak wood (Quercus robur L.) as a result of remaining submerged in Baltic Sea waters for two years*; Internat. Biodeter. Biodegrad. 86, 122–128, 2014.

Foster E.R. and Savage, R.J.; *Methods of Historical Shoreline Analysis*; Proc. Coastal Zone '89, ASCE, New York, USA, 1989.

François Charles, Jennifer Coston-Guarini, Jean-Marc Guarini, Sandrine Fanfard; *Wood decay at sea*; Journal of Sea Research (JSR), 2016, 114, pp.22-25. ff10.1016/j.seares.2016.05.002ff. final-01321467f

Freschet G.T., Weedon J.T., Aerts R., van Hal J.R., Cornelissen J.H.C.; Interspecific differences in wood decay rates: insights from a new short-term method to study long-term wood decomposition. J. Ecol. 100, 161–170, 2012. doi:10.1111/j.1365– 2745.2011.01896.x

Fukasawa Y.; Ecological impacts of fungal wood decay types: A review of current knowledge and future research directions. Ecological Research, 36, 910–931, 2021. https://doi.org/10.1111/1440-1703.12260

Genz F., Lessa G.C., Cirano M.; *The impact of an extreme flood upon the mixing zone of the Todos Santos Bay, Northeastern Brazil*; J. Coast. Res., 39, 707–712, 2006.

Girod L., Nuth C., Kääb A., Kohler J.; *Terrain changes from images acquired on opportunistic flights by SfM photogrammetry*, The Cryosphere 11(2):827-840, 2017; DOI: 10.5194/tc-11-827-2017.

Gomarasca M.A.; *Basics of geomatics*. Apply Geomatics **2**, 137–146, 2010. https://doi.org/10.1007/s12518-010-0029-6

Gonçalves J.A., Bastos L., Perez B., Magalhães A.; *Monitoring of beaches and sand dunes using digital aerial photography with direct georeferencing*. Int. Arch. Photogramm. Remote Sens. XXXVIII-7/B, 228–232, 2010.

Gonçalves J.A., Bastos L., Pinho J., Granja H.; *Digital aerial photography to monitor changes in coastal areas based on direct georeferencing*; Proceedings of the 5th EARSeL Workshop on Remote Sensing of the Coastal Zone, Prague, 2011.

Gonçalves J.A., Henriques R.; *UAV photogrammetry for topographic monitoring of coastal areas*; ISPRS Journal of Photogrammetry and Remote Sensing, Volume 104, Pages 101-111, 2015.

Green D.R.; *Unmanned aerial remote sensing: UAS for environmental applications*; CRC Press, 2020.

Grilliot M. J., Walker I. J., Bauer, B. O., *Airflow dynamics over a beach and foredune system with large woody debris;* Geosciences, 8(5), 147, 2018. https://doi.org/10.3390/geosciences8050147

Grilliot M. J., Walker I. J., Bauer B. O.; *Aeolian sand transport and deposition patterns within a large woody debris matrix fronting a foredune;* Geomorphology, 338, 1–15, 2019. https://doi.org/10.1016/j.geomorph.2019.04.010

Grilliot M. J., Walker I. J., Bauer B. O., *The Role of Large Woody Debris in Beach-Dune Interaction*; JGR Earth Surface, 2019.

Gülch E.; *Photogrammetric evaluation of multi-temporal fixed wing UAV imagery*. Int. Arch. Photogrammetry Remote Sensing XXXVIII-1/C22, 265–270, 2011.

Haala N.; *Comeback of digital image matching*; Photogrammetric Week. Wichmann Verlag, Heidelberg, pp. 289–301, 2009.

Haala N., Cramer M., Weimer F., Trittler M.; *Performance test on UAV-based data collection*; Int. Arch. Photogramm. Remote Sens. XXXVIII-1/C22, 7–12, 2011.

Haala N., Rothermel M.; *Dense Multi-Stereo Matching for High Quality Digital Elevation Models*. PFG Photogrammetrie, Fernerkundung, Geoinformation. 2012 (4), 331–343, 2012.

Haala N., Cramer M., Rothermel M.; *Quality of 3D point clouds from highly overlapping UAV Imagery*; Int. Arch. Photogramm. Remote Sens. XL-1/W2, 183– 188, 2013.

Harmon M. E., Fasth B., Woodall C. W., and Sexton J.; *Carbon concentration of standing and downed woody detritus: Effects of tree taxa, decay class, position, and tissue type*; Forest Ecology and Management, 291, 259–267, 2013. https://doi.org/10.1016/j. foreco.2012.11.046

Harmon M. E., Fasth B. G., Yatskov M., Kastendick D., Rock J., and Woodall C. W.; *Release of coarse woody detritus-related carbon: A synthesis across forest biomes*; Carbon Balance and Management, 15, 1, 2020. https://doi.org/10.1186/s13021-019-0136-6

Hartmann J., Jansen N., Dürr H. H., Kempe S. and Köhler P.; *Global CO_2 consumption by chemical weathering: What is the contribution of highly active weathering regions?* Glob. Planet. Change 69, 185–194, 2009.

Hartmann H., Bastos A., Das A.J., Esquivel-Muelbert A., Hammond W.M., Martínez-Vilalta J., McDowell N.G., Powers J.S., Pugh T.A., Ruthrof K.X. and Allen C.D.; *Climate change risks to global forest health: emergence of unexpected events of elevated tree mortality worldwide*; Annual Review of Plant Biology, *73*, pp.673-702, 2022.

Hesp P. A., Walker, I. J.; *Coastal Dunes. In* Aeolian Geomorphology (Vol. 11, pp. 328-355). Elsevier, 2013. https://doi.org/10.1016/B978-0-12-374739-6.00310-9

Hesp P. A., Hilton M., Konlecher, T.; *Flow and sediment transport dynamics in a slot and cauldron blowout and over a foredune, Mason Bay, Stewart Island (Rakiura), NZ*. Geomorphology, 295, 598–610, 2017. https://doi.org/10.1016/j.geomorph.2017.08.024

Höjgård-Olsen E.; *Observations of the tropical atmospheric water cycle and its variations with sea surface temperature using a constellation of satellites*; Ocean, Atmosphere. Université Paris-Saclay, 2020.

Iglhaut J., Cabo C., Puliti S., Piermattei L., O'Connor J., Rosette J.; *Structure from motion photogrammetry in forestry: A review*; Current Forestry Reports; 15;5:155-68, 2019.

IPCC; *Refinement to the 2006 IPCC Guidelines for National Greenhouse Gas Inventories, Vol. 4: Agriculture, Forestry and Other Land Use* (eds Blain, D., Agus, F., Alfaro, M. A. & Vreuls, H.) 68, 2019.

Ittekkot V., Humborg C., Rahm L. and Nguyen T. A.; *Interactions of the Major Biogeochemical Cycles: Global Change and Human Impacts;* Vol. 357 (eds Melillo, J. M., Field, C. B. and Moldan, B.) Ch. 17, 311–322, 2004.

Jaud M., Delacourt C., Le Dantec N., Allemand P., Ammann J-, Grandjean P-, Nouaille H-, Prunier C., Cuq V., Augereau E., Cocquempot L. and Floc'h F.; Diachronic UAV Photogrammetry of a Sandy Beach in Brittany (France) for a Long-Term Coastal Observatory; SPRS Int. J. Geo-Inf. 8, 267, 2019; doi:10.3390/ijgi8060267

Jordà G., Marbà N., Duarte C. M.; *Mediterranean seagrass vulnerable to regional climate warming*; Nature Climate Change 2, 821–824, 2012.

Kääb A., Girod L., Berthling, I.; *Surface kinematics of periglacial sorted circles using structure-from-motion technology*; The Cryosphere, 8, 1041-1056, doi:10.5194/tc-8-1041-2014, 2014.

Kachelreiss D., Wegmann M., Gollock M., Pettorelli N.; *The application of remote sensing for marine protected area management*; Ecol Indic 36:169–177, 2014.

Katz O. and Mushkin A.; *Characteristics of sea-cliff erosion induced by a strong winter storm in the eastern Mediterranean*, Quaternary Res., 80, 20–32, 2013.

Keijsers J.G.S., De Groot A.V., Riksen M.J.P.M.; *Vegetation and sedimentation on coastal foredunes*; Geomorphology, 228, 723–734, 2015. https://doi.org/10.1016/j.geomorph.2014.10.027

Kennedy H. et al.; *Seagrass sediments as a global carbon sink: Isotopic constraints*; Global Biogeochemical Cycles 24, GB4026, 2010.

Kennedy J., Blunden J., Alvar-Beltrán J., Kappelle M.; *2020 Global State of Climate*; World Meteorological Organization, 2021.

Krumins V., Gehlen M., Arndt S., Van Cappellen P. and Regnier P.; *Dissolved inorganic carbon and alkalinity fluxes from coastal marine sediments: model estimates for different shelf environments and sensitivity to global change*; Biogeosciences 10, 371–398, 2013.

Küng O., Strecha C., Beyeler A., Zufferey J.C., Floreano D., Fua P., Gervaix F.; *The accuracy of automatic photogrammetric techniques on ultra-light UAV imagery*; Int. Arch. Photogramm. Remote Sens. XXXVIII-1/C22, 125–130, 2011.

Laruelle G. G., Dürr H. H., Slomp C. P., Borges A. V.; *Evaluation of sinks and sources of CO_2 in the global coastal ocean using a spatially explicit typology of estuaries and continental shelves*. Geophysics Research Lett. 37, L15607, 2010.

Le Quéré C. et al.; *Trends in the sources and sinks of carbon dioxide*; Nature Geoscience 2, 831–836, 2009.

Lee D.S., Shan J.; *Combining LiDAR elevation data and IKONOS multispectral imagery for coastal classification mapping*; Marine Geodesy 28, 117–127, 2003.

Likens G. E., Mackenzie F. T., Richey J. E., Sedwell J. R., Turekian K. K.*; Flux of Organic Carbon from the Major Rivers of the World to the Oceans*; National Technical Information Service, US Department of Commerce, 1981.

Maas G.C.B., Sanquetta C.R., Marques R., Machado S.D.A., and Sanquetta M.N.I.; *Quantification of carbon in forest necromass: State of the art*; CERNE, 26(1), 98–108, 2020. https://doi.org/10.1590/01047760202026012661

Mancini F., Salvini R.; *Applications of Photogrammetry for Environmental Research*. ISPRS International Journal of Geo-Information 8(12):542, 2019. https://doi.org/10.3390/ijgi8120542

Marbà N., Duarte C. M.; *Mediterranean warming triggers seagrass (Posidonia oceanica) shoot mortality*; Global Change Biology. 16, 2366–2375, 2010.

Markku Larjavaara and Helene C. Muller-Landau; *Comparison of decay classification, knife test, and two penetrometers for estimating wood density of coarse woody debris*; Can. J. For. Res. 40: 2313–2321,2010. doi:10.1139/X10-170

Martin A. R., Doraisami M. and Thomas S. C.; *Global patterns in wood carbon concentration across the world's trees and forests*; Natural Geoscience; 11, 915–922, 2018.

Martin A. R., Domke G. M., Doraisami M. and Thomas S. C.; *Carbon fractions in the world's dead wood*; Nature Communications, 12, 889, 2021. https://doi.org/10.1038/s41467-021-21149-9

McCarthy Matthew J., Kaitlyn E. Colna, Mahmoud M. El-Mezayen, Abdiel E. Laureano-Rosario, Pablo Méndez-Lázaro, Daniel B. Otis, Gerardo Toro-Farmer, Maria Vega-Rodriguez, and Frank E. Muller-Karger; *Satellite remote sensing for coastal management: A review of successful applications;* Environmental management 60: 323-339, 2017.

McLeod E. et al.; *A blueprint for blue carbon: toward an improved understanding of the role of vegetated coastal habitats in sequestering CO_2*; Front. Ecol. Environ. 9, 552–560, 2011.

Mendonça R., Müller R.A., Clow D., et al.; *Organic carbon burial in global lakes and reservoirs*; Natural Community, 8 (1), p. 1694, 2017.

Mikhail E.M., Bethel J.S., McGlone J.C.; *Introduction to modern photogrammetry*. Wiley, New York, 2001.

Mitasova H., Drake T.G., Harmon R.S., Bernstein D.; *Quantifying rapid changes in coastal topography using modern mapping techniques and GIS*. Environmental Engineering Geoscience. 10 (1), 1–11, 2004.

Mitasova H., Overton M., Harmon R.S.; *Geospatial analysis of a coastal sand dune field evolution: Jockey's Ridge, North Carolina*; Geomorphology 72, 204–221, 2005.

Mitasova H., Overton M.F., Recalde J.J., Bernstein D.J., Freeman C.W.; *Raster based analysis of coastal terrain dynamics from multitemporal LIDAR data;* Journal of Coastal Research 25 (2), 507–514, 2009.

Mokroš M., Mikita T., Singh A., Tomaštík J., Chudá J., Wężyk P., Kuželka K., Surový P., Klimánek M., Zięba-Kulawik K., Bobrowski R.; *Novel low-cost mobile mapping systems for forest inventories as terrestrial laser scanning alternatives*; International Journal of Applied Earth Observation and Geoinformation 104:102512, 2021.

Mulholland P. J., Elwood J. W.; *The role of lake and reservoir sediments as sinks in the perturbed global carbon cycle*; Tellus 34, 490–499, 1982.

Muller-Karger F. E. et al.; *The importance of continental margins in the global carbon cycle*; Geophys. Res. Lett. 32, L01602, 2005.

Nellemann C. et al.; *Blue Carbon: A Rapid Response Assessment*; United Nations Environment Programme, 2009.

Nelson T.A., Boots B.; *Detecting spatial hot spots in landscape ecology*; Ecography 31, 556–566, 2008.

Nolan M., Larsen C., Sturm M.; *Mapping snow depth from manned aircraft on landscape scales at centimetre resolution using structure-from-motion photogrammetry*; The Cryosphere, 9,1445-1463, doi:10.5194/tc-9-1445-2015, 2015.

Oettel J., Zolles A., Gschwantner T., Lapin K., Kindermann G., Schweinzer K.M., Gossner M.M., Essl F.; *Dynamics of standing deadwood in Austrian forests under varying forest management and climatic conditions*; Journal of Applied Ecology, Volume 60, Issue 4, Pages 696 – 713, 2023.

Orth R. J. et al.; *A global crisis for seagrass ecosystems*; BioScience 56, 987-996, 2006.

Ouédraogo M. M., Degré A., Debouche C., Lisein, J.; *The evaluation of unmanned aerial system-based photogrammetry and terrestrial laser scanning to generate DEMs of agricultural watersheds*; Geomorphology, 214, 339-355, 2014.

Oyedotun, T.D.T.; *Shoreline Geometry: DSAS as a Tool for Historical Trend Analysis*, Geomorphological Techniques chapter 3, ISSN 2047-0371, 2014.

Pettorelli N., Chauvenet A.L.M., Duffy J.P., Cornforth W.A., Meillere A., Baillie J.E.M.; *Tracking the effect of climate change on ecosystem function using protected areas: Africa as a case study*. Ecol Indic 20:269–276, 2012.

Pettorelli N., Laurance W.F., O'Brien T.G., Wegmann M., Nagendra H., Turner W.; *Satellite remote sensing for applied ecologists: opportunities and challenges*. J Appl Ecol 51:839–848, 2014.

Prairie Y. T. and Duarte C. M.; *Direct and indirect metabolic CO2 release by humanity*; Bio geosciences 4, 215–217, 2007.

Přívětivý T. and Šamonil P.; *Variation in downed deadwood density, biomass, and moisture during decomposition in a natural temperate forest*; Forests, 12, 1352, 2021. https://doi.org/10.3390/f12101352

Quinton J. N., Govers G., Van Oost K., Bardgett R. D.; *The impact of agricultural soil erosion on biogeochemical cycling*; Nature Geoscience 3, 311–314, 2010.

Regnier P. et al.; *Anthropogenic perturbation of the carbon fluxes from land to ocean*; Nature Geoscience, 2013.

Reitz M.D., Jerolmack D.J., Ewing R.C., Martin R.L.; *Barchan-parabolic dune pattern transition from vegetation stability threshold*; Geophysical Research Letters 37, 5p, 2010.

Remondino F., Barazzetti L., Nex F., Scaioni M., Sarazzi D.; *UAV photogrammetry for mapping and 3D modeling – current status and future perspectives*; Int. Arch. Photogramm. Remote Sens. 63, 25–31, 2011.

Reusch T. B. H., Ehlers A., Hämmerli A., Worm B.; *Ecosystem recovery after climatic extremes enhanced by genotypic diversity*; Proc. Natl Acad. Sci. USA 102, 2826–2831, 2005.

Richey J. E.; *The Global Carbon Cycle, Integrating Humans, Climate, and the Natural World*; Vol. 17 (eds Field, C. B. and Raupach, M. R.) 329–340, Island Press, 2004.

Rinne-Garmston K. T., Peltoniemi K., Chen J., Peltoniemi M., Fritze H. and Mäkipää R.; *Carbon flux from decomposing wood and its dependency on temperature, wood N2 fixation rate, moisture and fungal composition in a Norway spruce forest*; Global Change Biology, 25(5), 1852–1867, 2019.

Room M.H., Anuar A.; *Integration of Lidar system, mobile laser scanning (MLS) and unmanned aerial vehicle system for generation of 3D building model application: A review*; InIOP Conference Series: Earth and Environmental Science (Vol. 1064, No. 1, p. 012042), IOP Publishing, 2022.

Rosnell T., Honkavaara E.; *Point cloud generation from aerial image data acquired by a quadrocopter type micro unmanned aerial vehicle and a digital still camera*. Sensors 12 (1), 453–480, 2012.

Sallenger Jr. A.H., Krabill W.B., Swift R.N., Brock J., List J., Hansen M., Holman R.A., Manizade S., Sontag J., Meredith A., Morgan K., Yunkel J.K., Frederick E.B., Stockdon H.; *Evaluation of airborne topographic LiDAR for quantifying beach changes*; Journal of Coastal Research 19, 125–133, 2003.

Saye S.E., van der Wal D., Pye K., Blott S.J.; *Beach-dune morphological relationships and erosion/accretion: an investigation at five sites in England and Wales using LiDAR data*; Geomorphology 72, 128–155, 2002.

Scarellia F.M., Sistilli F., Fabbri S., Cantelli L., Barboza E.G., Gabbianelli G.; *Remote Sensing Applications: Society and Environment* 7, 27–39, 2017.

Sendrowski A., Wohl E.; *Remote sensing of large wood in high resolution satellite imagery: Design of an automated classification workflow for multiple wood deposit types*; Earth Surface Processes and Landforms 46(12). 2021. DOI: 10.1002/esp.5179

Sendrowski A., Wohl E., Hilton R., Kramer N., Ascough P.; *Wood-Based Carbon Storage in the Mackenzie River Delta: The World's Largest Mapped Riverine Wood Deposit*; Geophysical Research Letters, Volume 50, Issue 7, 2023 https://doi.org/10.1029/2022GL100913

Shorohova E., Kapitsa E., Kuznetsov A., Kuznetsova S., Lopes de Gerenyu V., Kaganov V., Kurganova I.; *Coarse woody debris density and carbon concentration by decay classes in mixed montane wet tropical forests*; Biotropica, 54:635–644, 2022.

Shrestha R.L., Carter W.E., Sartori M., Luzum B.J., Slatton K.C.; *Airborne laser swath mapping: quantifying changes in sandy beaches over time scales of weeks to years;* Photogrammetry and Remote Sensing 59, 222–232, 2005.

Short A. D. and Trembanis A. C.; *Decadal scale patterns in beach oscillation and rotation Narrabeen beach, Australia-Time series, PCA and Wavelet analysis*; J. Coast. Res., 20, 523–532, 2004.

Sivaranjani S., Pal Panwar V.; *Agricultural Soil Sustainability and Carbon Management* - chapter 8; Carbon sequestration in agroforestry systems; Pages 207-227, 2023.

Smith S. V., Hollibaugh J. T.; *Coastal metabolism and the oceanic organic carbon balance*; Rev. Geophysics 31, 75–89, 1993.

Stallard R. F.; *Terrestrial sedimentation and the carbon cycle: coupling weathering and erosion to carbon burial*; Global Biogeochemical Cycles 12, 231–257, 1998.

Stets E. G., Striegl R. G., Aiken G. R., Rosenberry D. O. and Winter T. C.; *Hydrologic support of carbon dioxide flux revealed by whole-lake carbon budgets*. J. Geophys. Res.-Biogeosciences 114, G1, 2009.

Štroner M., Urban R., Línková L., *A New Method for UAV Lidar Precision Testing Used for the Evaluation of an Affordable DJI ZENMUSE L1 Scanner*; *Remote Sensing*, *13*(23), 4811, 2021.

Teodoro Ana C.; *Optical satellite remote sensing of the coastal zone environment - An overview;* Environment Applications of Remote Sensing. London, UK, InTechOpen: 165-196, 2016.

Thébaudeau B., Trenhaile A.S., Edwards R.J.; *Modelling the development of rocky shoreline profiles along the northern coast of Ireland*; Geomorphology, 203, 66–78, 2013.

Thieler E.R. and Danforth W.W.; *Historical shoreline mapping (I) Improving techniques and reducing positioning errors*; J. Coast. Res., 10, 549–563, 1994a.

Thieler E.R. and Danforth W.W.; *Historical shoreline mapping (II) Application of the Digital Shoreline Mapping and Analysis Systems (DSMS/DSAS) to shoreline change mapping in Puerto Rico*; J. Coast. Res., 10, 600–620, 1994b.

Tranvik L. J. et al.; *Lakes and reservoirs as regulators of carbon cycling and climate*; Limnol. Oceanogr. 54, 2298–2314, 2009.

Vallet J., Panissod F., Strecha C., Tracol M.; *Photogrammetric performance of an ultra-light weight Swinglet "UAV"*. Int. Arch. Photogrammetric Remote Sensing 63, 253–258, 2011.

Ver L. M. B., Mackenzie F. T., Lerman A.; *Biogeochemical responses of the carbon cycle to natural and human perturbations: past, present, and future*; Am. J. Sci. 299, 762–801, 1999.

Walker I.J., Davidson-Arnott R.G.D., Bauer B.O., Hesp P.A., Delgado-Fernandez I., Ollerhead J., Smyth T.A.G.; *Scale- dependent perspectives on the geomorphology and evolution of beach-dune systems*; Earth-Science Reviews, 2017. https://doi.org/ 10.1016/j.earscirev.2017.04.011

Wanninkhof R. et al.; *Global Ocean carbon uptake: magnitude, variability and trends*. Biogeosciences Discussion; 9, 10961-11012, 2012.

Warren W.G. and Olsen P.F.; *A line intersect technique for assuming logging waste*. For. Sci. 10(3): 267–276, 1964.

Waycott M. et al.; *Accelerating loss of seagrasses across the globe threatens coastal ecosystems*; Proc. Natl Acad. Sci. USA 106, 12377-12381, 2009.

Weggler K., Dobbertin M., Jüngling E. et al.; *Dead wood volume to dead wood carbon: the issue of conversion factors*; Eur J Forest Res 131, 1423–1438, 2012.
https://doi.org/10.1007/s10342-012-0610-0

Wernberg T., Thomsen M. S., Tuya F., Kendrick; *Biogenic habitat structure of seaweeds change along a latitudinal gradient in ocean temperature;* Journal of Experimental Marine Biology and Ecology 400, 264–271, 2011.

Westoby M., Brasington J., Glasser N., Hambrey M., Reynolds J.; *Structure-from-Motion photogrammetry: A low-cost, effective tool for geoscience applications*; Geomorphology, 179, 300-314, 2012.

White S.A., Wang Y.; *Utilizing DEMs derived from LIDAR data to analyse morphologic change in the North Carolina coastline*; Remote Sensing Environment 85, 39–47, 2003.

Wild M., Folini D., Schär C. et al.; *The global energy balance from a surface perspective*; Climate Dynamics 40, 3107–3134, 2013. https://doi.org/10.1007/s00382-012-1569-8

Woolard J.W., Colby J.D.; *Spatial characterization, resolution, and volumetric change of coastal dunes using airborne LiDAR: Cape Hatteras, North Carolina*; Geomorphology 48, 269–287, 2002.

Yang Gao, Junjie Jia, Yao Lu, Kun Sun, Jing Wang, Shuoyue Wang; *Carbon transportation, transformation, and sedimentation processes at the land-river-estuary continuum*; Fundamental Research, 2022.

Yoo C.I., Oh T.S.; *Beach Volume Change Using UAV Photogrammetry Song Jung Beach, Korea*; The International Archives of the Photogrammetry, Remote Sensing and Spatial Information Sciences; Volume XLI-B8, 2016.

I. Annex I

Agisoft Metashape

Processing Report A2_pre

22 June 2023

Survey Data

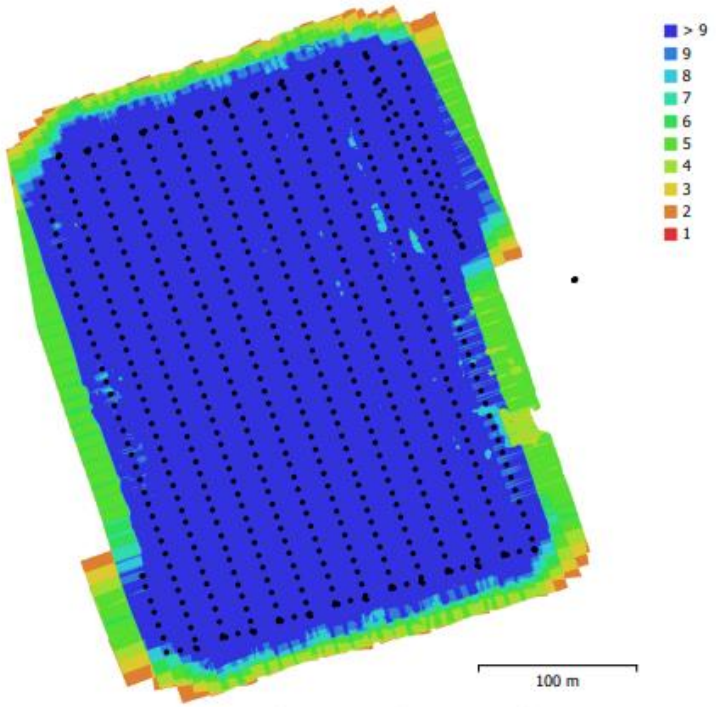

Fig. 1. Camera locations and image overlap.

Number of images:	668	Camera stations:	629
Flying altitude:	60.7 m	Tie points:	491,334
Ground resolution:	7.29 mm/pix	Projections:	1,687,423
Coverage area:	0.113 km²	Reprojection error:	3.5 pix

Camera Model	Resolution	Focal Length	Pixel Size	Precalibrated
ZenmuseP1 (35mm)	8192 x 5460	35 mm	4.39 x 4.39 µm	No

Table 1. Cameras.

Camera Calibration

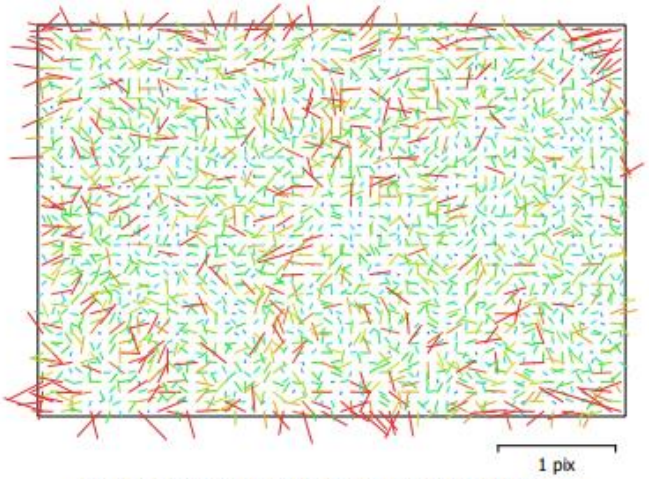

Fig. 2. Image residuals for ZenmuseP1 (35mm).

ZenmuseP1 (35mm)

668 images

Type	Resolution	Focal Length	Pixel Size
Frame	**8192 x 5460**	**35 mm**	**4.39 x 4.39 µm**

F:	8179.23		
Cx:	-29.3995	B1:	1.59175
Cy:	13.7169	B2:	-0.111127
K1:	-0.0492605	P1:	-0.00114097
K2:	0.0230771	P2:	0.000754961
K3:	-0.106671	P3:	0
K4:	0	P4:	0

Ground Control Points

Fig. 3. GCP locations and error estimates.
Z error is represented by ellipse color. X,Y errors are represented by ellipse shape.
Estimated GCP locations are marked with a dot or crossing.

Count	X error (cm)	Y error (cm)	Z error (cm)	XY error (cm)	Total (cm)
5	0.653171	0.880775	0.0605346	1.09654	1.09821

Table 2. Control points RMSE.
X - Easting, Y - Northing, Z - Altitude.

Count	X error (cm)	Y error (cm)	Z error (cm)	XY error (cm)	Total (cm)
2	1.46914	2.03652	1.89284	2.51113	3.14462

Table 3. Check points RMSE.
X - Easting, Y - Northing, Z - Altitude.

Label	X error (cm)	Y error (cm)	Z error (cm)	Total (cm)	Image (pix)
m001	-0.566861	-1.60821	0.0697659	1.70662	0.238 (11)
m003	0.233683	0.232237	-0.0809424	0.339254	0.219 (12)
m004	-0.0622625	0.0616564	0.0215484	0.0902356	0.265 (12)
m006	1.11291	1.08788	-0.0616887	1.55752	0.312 (6)
m007	-0.717473	0.226442	0.0513167	0.754107	0.181 (9)
area.legno.1					
area.legno.2					
Total	**0.653171**	**0.880775**	**0.0605346**	**1.09821**	**0.242**

Table 4. Control points.
X - Easting, Y - Northing, Z - Altitude.

Label	X error (cm)	Y error (cm)	Z error (cm)	Total (cm)	Image (pix)
m002	0.800418	-0.00416098	2.5311	2.65465	0.290 (10)
m005	-1.91731	-2.88007	0.87132	3.56793	0.228 (9)
Total	**1.46914**	**2.03652**	**1.89284**	**3.14462**	**0.262**

Table 5. Check points.
X - Easting, Y - Northing, Z - Altitude.

Digital Elevation Model

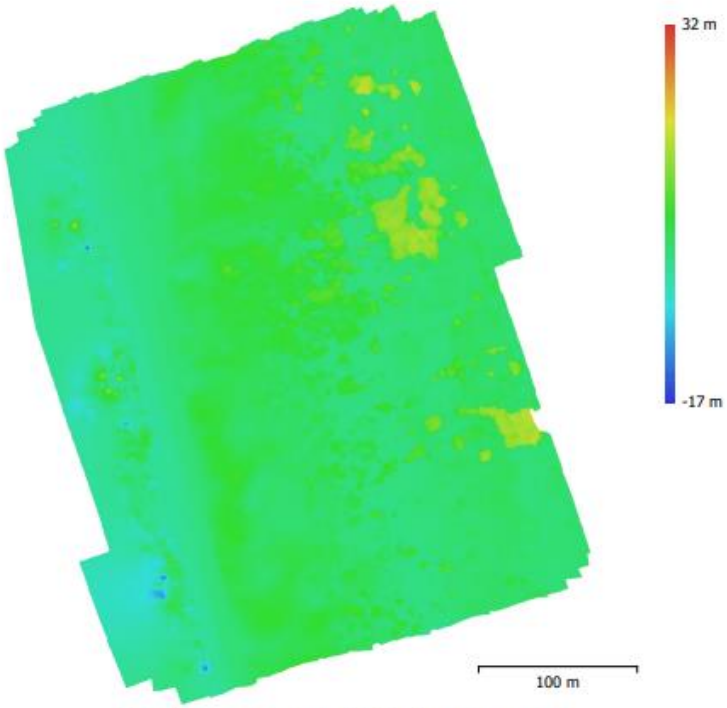

Fig. 4. Reconstructed digital elevation model.

Resolution:	2.92 cm/pix
Point density:	0.118 points/cm²

Processing Parameters

General	
Cameras	668
Aligned cameras	629
Markers	9
Coordinate system	WGS 84 / UTM zone 32N (EPSG::32632)
Rotation angles	Yaw, Pitch, Roll
Point Cloud	
Points	491,334 of 547,016
RMS reprojection error	0.163483 (3.50233 pix)
Max reprojection error	0.580828 (83.9042 pix)
Mean key point size	19.4647 pix
Point colors	3 bands, uint8
Key points	990.34 MB
Average tie point multiplicity	3.73585
Alignment parameters	
Accuracy	Low
Generic preselection	Yes
Reference preselection	Source
Key point limit	0
Tie point limit	0
Exclude stationary tie points	Yes
Guided image matching	No
Adaptive camera model fitting	Yes
Matching time	50 minutes 52 seconds
Matching memory usage	729.79 MB
Alignment time	7 minutes 55 seconds
Alignment memory usage	422.61 MB
Optimization parameters	
Parameters	f, b1, b2, cx, cy, k1-k3, p1, p2
Adaptive camera model fitting	No
Optimization time	47 seconds
Date created	2022:06:28 10:08:24
Software version	1.7.1.11797
File size	51.88 MB
Depth Maps	
Count	621
Depth maps generation parameters	
Quality	Medium
Filtering mode	Mild
Processing time	2 hours 23 minutes
Memory usage	4.20 GB
Date created	2022:06:30 15:17:04
Software version	1.7.1.11797
File size	2.10 GB
Dense Point Cloud	
Points	170,333,277
Point colors	3 bands, uint8
Depth maps generation parameters	
Quality	Medium
Filtering mode	Mild

Processing time	2 hours 23 minutes
Memory usage	4.20 GB
Dense cloud generation parameters	
Processing time	1 hours 44 minutes
Memory usage	6.48 GB
Ground points classification parameters	
Max angle (°)	3.5
Max distance (m)	0.1
Cell size (m)	0.5
Classification time	29 minutes 18 seconds
Classification memory usage	6.97 GB
Date created	2022:06:30 17:01:37
Software version	1.7.1.11797
File size	2.39 GB
DEM	
Size	14,403 x 19,824
Coordinate system	WGS 84 / UTM zone 32N (EPSG::32632)
Reconstruction parameters	
Source data	Dense cloud
Interpolation	Enabled
Processing time	8 minutes 51 seconds
Memory usage	310.45 MB
Date created	2022:09:06 08:16:34
Software version	1.7.2.12070
File size	677.46 MB
Orthomosaic	
Size	50,688 x 60,544
Coordinate system	WGS 84 / UTM zone 32N (EPSG::32632)
Colors	3 bands, uint8
Reconstruction parameters	
Blending mode	Mosaic
Surface	DEM
Enable hole filling	Yes
Enable ghosting filter	No
Processing time	4 hours 30 minutes
Memory usage	4.06 GB
Date created	2022:06:30 18:53:17
Software version	1.7.1.11797
File size	40.23 GB
System	
Software name	Agisoft Metashape Professional
Software version	1.8.3 build 14331
OS	Windows 64 bit
RAM	31.39 GB
CPU	11th Gen Intel(R) Core(TM) i7-1185G7 @ 3.00GHz
GPU(s)	None

Agisoft Metashape

Processing Report A2_pre

22 June 2023

Survey Data

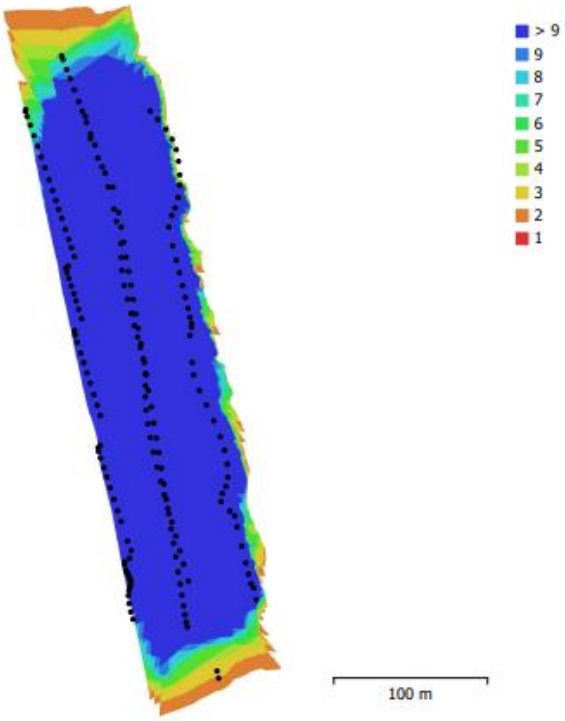

Fig. 1. Camera locations and image overlap.

Number of images:	185	Camera stations:	185
Flying altitude:	54.7 m	Tie points:	230,322
Ground resolution:	7.44 mm/pix	Projections:	718,649
Coverage area:	0.0402 km²	Reprojection error:	2.94 pix

Camera Model	Resolution	Focal Length	Pixel Size	Precalibrated
ZenmuseP1 (35mm)	8192 x 5460	35 mm	4.39 x 4.39 µm	No

Table 1. Cameras.

Camera Calibration

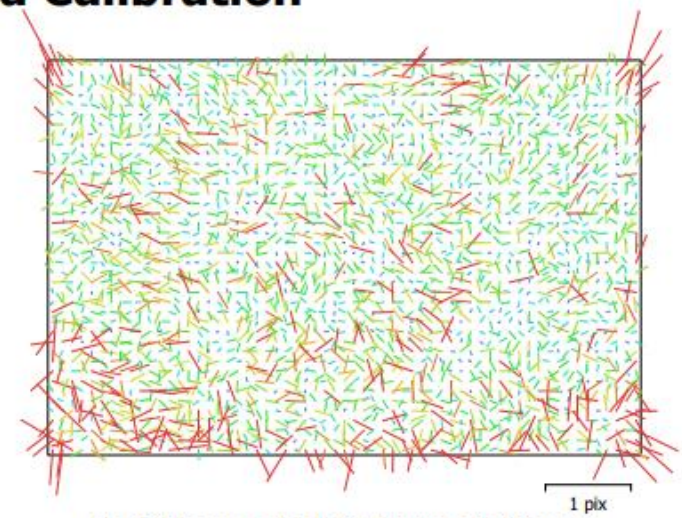

Fig. 2. Image residuals for ZenmuseP1 (35mm).

ZenmuseP1 (35mm)

185 images

Type	Resolution	Focal Length	Pixel Size
Frame	**8192 x 5460**	**35 mm**	**4.39 x 4.39 µm**

	Value	Error	F	B1	B2	K1	K2	P1	P2
F	**8181.5**	1.4	1.00	-0.97	0.10	-0.04	-0.05	0.01	-0.16
B1	**17.1331**	0.67		1.00	-0.10	-0.01	0.09	-0.01	0.28
B2	**14.5507**	0.29			1.00	0.03	-0.02	-0.85	-0.14
K1	**-0.040742**	8.7e-05				1.00	-0.94	-0.04	-0.08
K2	**-0.0344851**	0.00024					1.00	0.02	0.02
P1	**-0.000637034**	1.3e-05						1.00	0.12
P2	**0.000979454**	1.1e-05							1.00

Table 2. Calibration coefficients and correlation matrix.

Ground Control Points

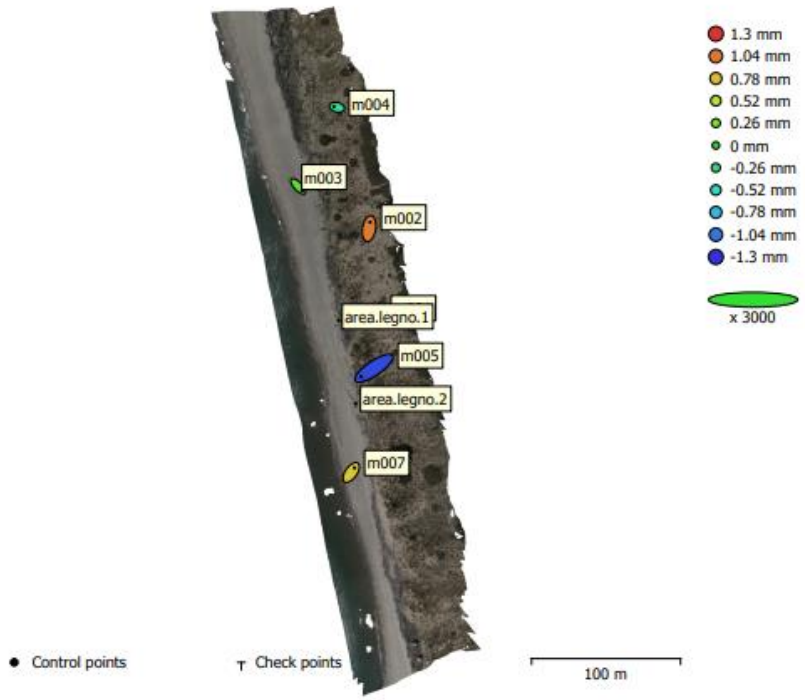

Fig. 3. GCP locations and error estimates.
Z error is represented by ellipse color. X,Y errors are represented by ellipse shape.
Estimated GCP locations are marked with a dot or crossing.

Count	X error (mm)	Y error (mm)	Z error (mm)	XY error (mm)	Total (mm)
6	2.89142	2.29984	0.740748	3.69453	3.76806

Table 3. Control points RMSE.
X - Easting, Y - Northing, Z - Altitude.

Label	X error (mm)	Y error (mm)	Z error (mm)	Total (mm)	Image (pix)
m001	3.20084	0.53215	-0.313943	3.25993	0.213 (3)
m002	0.455447	2.88662	1.02096	3.09554	0.229 (5)
m003	1.82125	-1.9232	0.145439	2.6527	0.197 (4)
m004	-1.28778	0.303304	-0.375591	1.37529	0.193 (6)
m005	-5.69743	-3.87526	-1.20678	6.99533	0.303 (6)
m007	1.50767	2.07639	0.729921	2.66781	0.159 (6)
area.legno.1					
area.legno.2					
Total	**2.89142**	**2.29984**	**0.740748**	**3.76806**	**0.222**

Table 4. Control points.

X - Easting, Y - Northing, Z - Altitude.

Digital Elevation Model

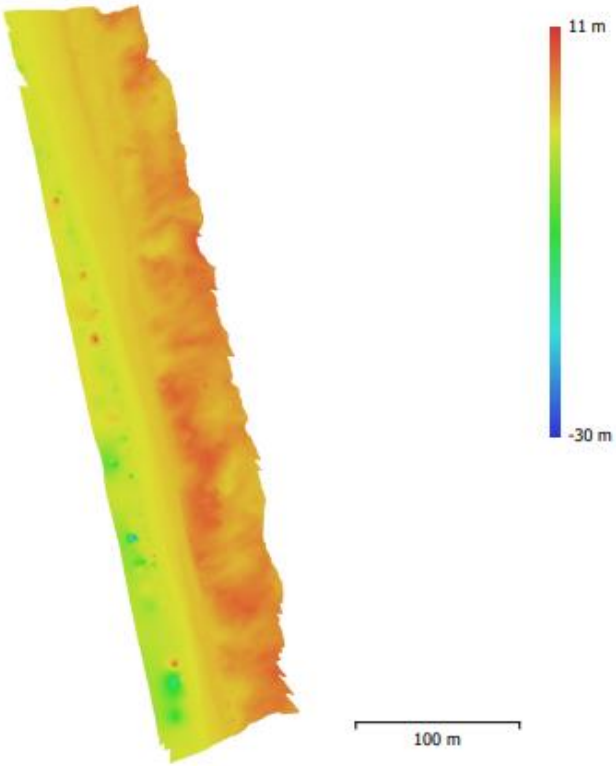

Fig. 4. Reconstructed digital elevation model.

Resolution:	2.98 cm/pix
Point density:	0.113 points/cm²

Processing Parameters

General	
Cameras	185
Aligned cameras	185
Markers	8
Coordinate system	WGS 84 / UTM zone 32N (EPSG::32632)
Rotation angles	Yaw, Pitch, Roll
Point Cloud	
Points	230,322 of 249,376
RMS reprojection error	0.14276 (2.94157 pix)
Max reprojection error	1.10694 (84.2171 pix)
Mean key point size	18.5881 pix
Point colors	3 bands, uint8
Key points	221.05 MB
Average tie point multiplicity	3.38392
Alignment parameters	
Accuracy	Low
Generic preselection	Yes
Reference preselection	Source
Key point limit	0
Tie point limit	0
Exclude stationary tie points	Yes
Guided image matching	No
Adaptive camera model fitting	Yes
Matching time	9 minutes 43 seconds
Matching memory usage	684.59 MB
Alignment time	1 minutes 34 seconds
Alignment memory usage	106.58 MB
Optimization parameters	
Parameters	f, b1, b2, k1, k2, p1, p2
Adaptive camera model fitting	No
Optimization time	11 seconds
Date created	2022:07:04 07:47:16
Software version	1.7.1.11797
File size	22.11 MB
Depth Maps	
Count	185
Depth maps generation parameters	
Quality	Medium
Filtering mode	Mild
Processing time	32 minutes 1 seconds
Memory usage	4.19 GB
Date created	2022:07:04 10:04:29
Software version	1.7.1.11797
File size	733.43 MB
Dense Point Cloud	
Points	40,870,829
Point colors	3 bands, uint8
Depth maps generation parameters	
Quality	Medium
Filtering mode	Mild

Processing time	32 minutes 1 seconds
Memory usage	4.19 GB
Dense cloud generation parameters	
Processing time	36 minutes 58 seconds
Memory usage	4.76 GB
Date created	2022:07:04 10:41:27
Software version	1.7.1.11797
File size	601.63 MB
DEM	
Size	7,333 x 17,511
Coordinate system	WGS 84 / UTM zone 32N (EPSG::32632)
Reconstruction parameters	
Source data	Dense cloud
Interpolation	Enabled
Processing time	3 minutes 44 seconds
Memory usage	289.20 MB
Date created	2022:07:04 10:45:12
Software version	1.7.1.11797
File size	232.70 MB
Orthomosaic	
Size	24,340 x 62,164
Coordinate system	WGS 84 / UTM zone 32N (EPSG::32632)
Colors	3 bands, uint8
Reconstruction parameters	
Blending mode	Mosaic
Surface	DEM
Enable hole filling	Yes
Enable ghosting filter	No
Processing time	1 hours 56 minutes
Memory usage	6.02 GB
Date created	2022:07:04 11:17:03
Software version	1.7.1.11797
File size	13.53 GB
System	
Software name	Agisoft Metashape Professional
Software version	1.8.3 build 14331
OS	Windows 64 bit
RAM	31.39 GB
CPU	11th Gen Intel(R) Core(TM) i7-1185G7 @ 3.00GHz
GPU(s)	None

Agisoft Metashape

Processing Report A2_pre

22 June 2023

Survey Data

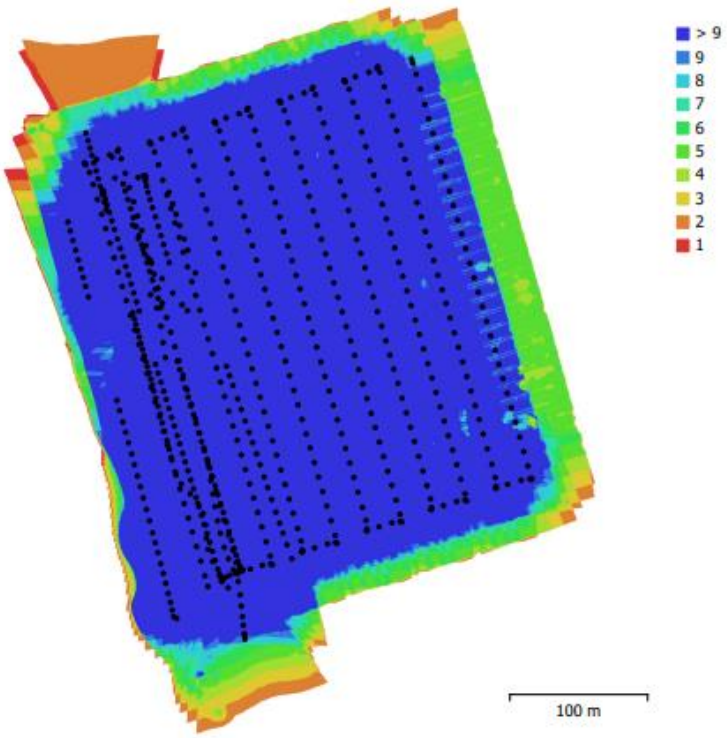

Fig. 1. Camera locations and image overlap.

Number of images:	632	Camera stations:	632
Flying altitude:	80.5 m	Tie points:	634,791
Ground resolution:	8.75 mm/pix	Projections:	2,410,422
Coverage area:	0.146 km²	Reprojection error:	4 pix

Camera Model	Resolution	Focal Length	Pixel Size	Precalibrated
ZenmuseP1 (35mm)	8192 x 5460	35 mm	4.39 x 4.39 µm	No

Table 1. Cameras.

Camera Calibration

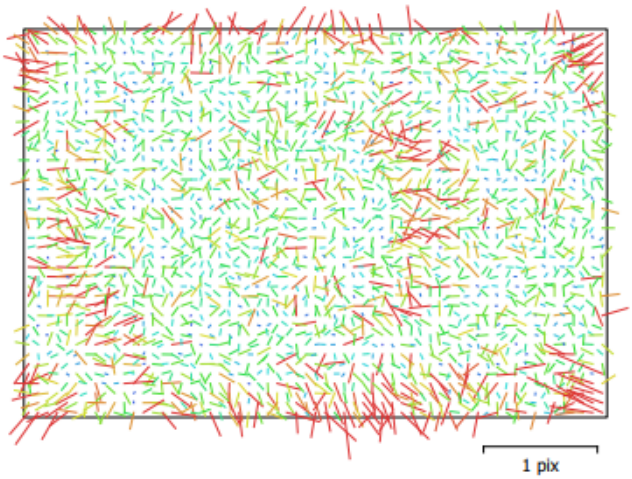

Fig. 2. Image residuals for ZenmuseP1 (35mm).

ZenmuseP1 (35mm)

632 images

Type	Resolution	Focal Length	Pixel Size
Frame	**8192 x 5460**	**35 mm**	**4.39 x 4.39 µm**

	Value	Error	F	Cx	Cy	K1	K2	K3	P1	P2
F	**8200.21**	0.26	1.00	-0.03	-0.70	-0.16	0.13	-0.13	0.01	0.29
Cx	**-30.132**	0.14		1.00	0.02	-0.01	0.02	-0.02	0.65	-0.02
Cy	**13.8977**	0.21			1.00	0.02	-0.01	0.02	0.00	-0.02
K1	**-0.0501099**	0.0001				1.00	-0.96	0.91	-0.01	-0.03
K2	**0.028288**	0.00063					1.00	-0.98	0.02	0.01
K3	**-0.119825**	0.0012						1.00	-0.02	-0.01
P1	**-0.00112615**	4.2e-06							1.00	0.01
P2	**0.000801115**	3.9e-06								1.00

Table 2. Calibration coefficients and correlation matrix.

Ground Control Points

Fig. 3. GCP locations and error estimates.
Z error is represented by ellipse color. X,Y errors are represented by ellipse shape.
Estimated GCP locations are marked with a dot or crossing.

Count	X error (cm)	Y error (cm)	Z error (cm)	XY error (cm)	Total (cm)
8	0.81572	0.590766	0.125823	1.00718	1.015

Table 3. Control points RMSE.
X - Easting, Y - Northing, Z - Altitude.

Label	X error (cm)	Y error (cm)	Z error (cm)	Total (cm)	Image (pix)
m3	-0.718458	0.184493	0.21459	0.772184	1.394 (11)
m2	-0.316699	-1.3246	-0.201186	1.37671	0.370 (9)
m4bis	0.25401	0.602255	-0.0530617	0.65578	0.887 (17)
m5	-1.17498	-0.321084	-0.0329023	1.21851	0.167 (10)
m6	0.942762	0.207036	0.0392816	0.966027	0.213 (11)
m7	-0.181987	-0.0335691	-0.133122	0.227964	0.149 (9)
m8	0.371014	0.069933	0.0727291	0.384488	0.222 (10)
m9	1.48393	0.699108	0.108053	1.64392	0.303 (14)
area.pesa.legn...					
arealegna2					
Total	**0.81572**	**0.590766**	**0.125823**	**1.015**	**0.652**

Table 4. Control points.
X - Easting, Y - Northing, Z - Altitude.

Digital Elevation Model

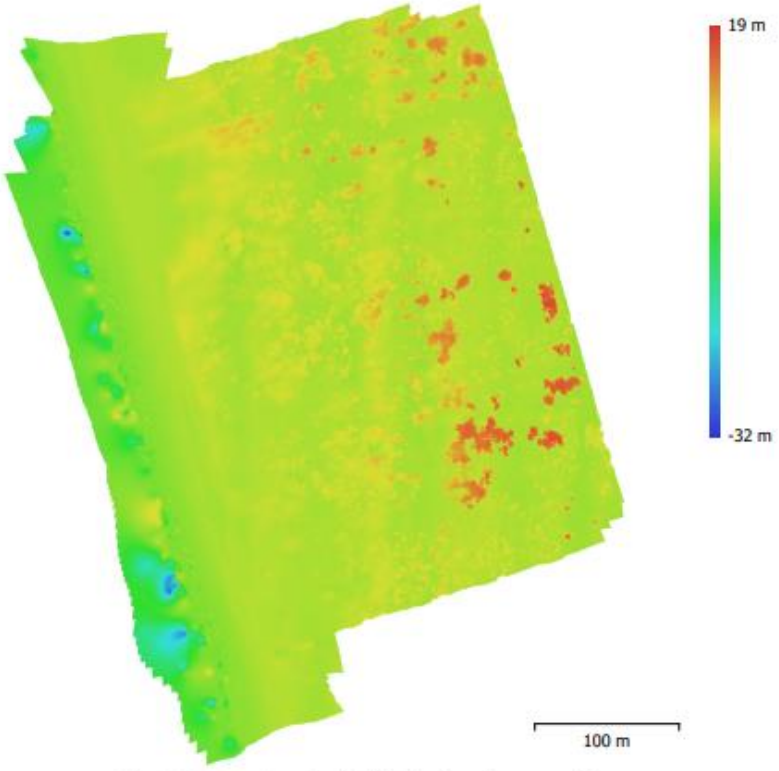

Fig. 4. Reconstructed digital elevation model.

Resolution:	3.4 cm/pix
Point density:	867 points/m²

Processing Parameters

General	
Cameras	632
Aligned cameras	632
Markers	10
Coordinate system	WGS 84 / UTM zone 32N (EPSG::32632)
Rotation angles	Yaw, Pitch, Roll
Point Cloud	
Points	634,791 of 729,052
RMS reprojection error	0.199865 (3.99658 pix)
Max reprojection error	0.895475 (170.946 pix)
Mean key point size	17.9692 pix
Point colors	3 bands, uint8
Key points	No
Average tie point multiplicity	4.47886
Alignment parameters	
Accuracy	Low
Generic preselection	No
Reference preselection	Source
Key point limit	0
Tie point limit	0
Exclude stationary tie points	No
Guided image matching	No
Adaptive camera model fitting	No
Matching time	10 minutes 49 seconds
Matching memory usage	1.50 GB
Alignment time	8 minutes 19 seconds
Alignment memory usage	602.86 MB
Optimization parameters	
Parameters	f, cx, cy, k1-k3, p1, p2
Adaptive camera model fitting	No
Optimization time	23 seconds
Date created	2022:05:06 10:34:42
Software version	1.7.2.12070
File size	66.52 MB
Depth Maps	
Count	632
Depth maps generation parameters	
Quality	Medium
Filtering mode	Mild
Processing time	2 hours 44 minutes
Memory usage	4.28 GB
Date created	2022:05:12 18:02:15
Software version	1.7.2.12070
File size	2.54 GB
Dense Point Cloud	
Points	157,908,166
Point colors	3 bands, uint8
Depth maps generation parameters	
Quality	Medium
Filtering mode	Mild

Processing time	2 hours 44 minutes
Memory usage	4.28 GB
Dense cloud generation parameters	
Processing time	1 hours 28 minutes
Memory usage	6.85 GB
Date created	2023:03:02 19:22:23
Software version	1.7.2.12070
File size	2.21 GB
DEM	
Size	16,105 x 18,981
Coordinate system	WGS 84 / UTM zone 32N (EPSG::32632)
Reconstruction parameters	
Source data	Dense cloud
Interpolation	Enabled
Processing time	3 minutes 34 seconds
Memory usage	355.62 MB
Date created	2022:05:17 12:54:10
Software version	1.7.2.12070
File size	632.06 MB
Orthomosaic	
Size	51,287 x 62,068
Coordinate system	WGS 84 / UTM zone 32N (EPSG::32632)
Colors	3 bands, uint8
Reconstruction parameters	
Blending mode	Mosaic
Surface	DEM
Enable hole filling	Yes
Enable ghosting filter	No
Processing time	57 minutes 18 seconds
Memory usage	11.92 GB
Date created	2022:05:17 13:26:43
Software version	1.7.2.12070
File size	53.72 GB
System	
Software name	Agisoft Metashape Professional
Software version	1.8.3 build 14331
OS	Windows 64 bit
RAM	31.39 GB
CPU	11th Gen Intel(R) Core(TM) i7-1185G7 @ 3.00GHz
GPU(s)	None

Agisoft Metashape

Processing Report A2_pre

22 June 2023

Survey Data

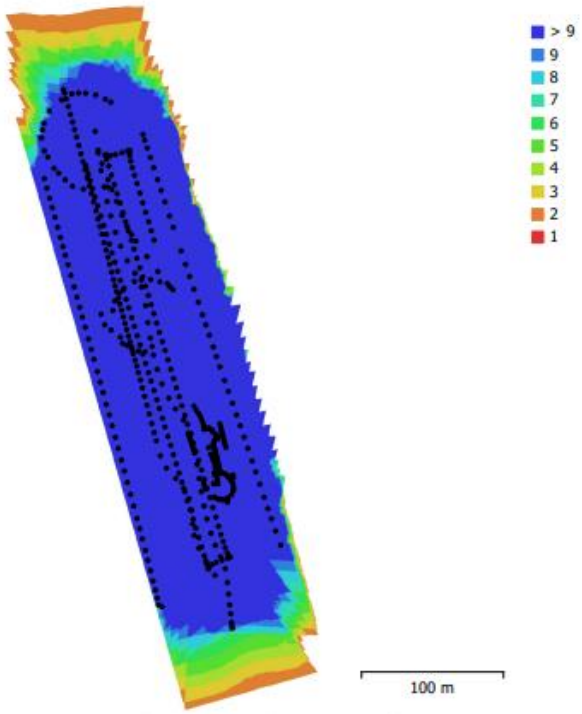

Fig. 1. Camera locations and image overlap.

Number of images:	443	Camera stations:	443
Flying altitude:	58.7 m	Tie points:	1,683,429
Ground resolution:	7.23 mm/pix	Projections:	5,944,247
Coverage area:	0.0526 km²	Reprojection error:	1.28 pix

Camera Model	Resolution	Focal Length	Pixel Size	Precalibrated
ZenmuseP1 (35mm)	8192 x 5460	35 mm	4.39 x 4.39 µm	No

Table 1. Cameras.

Camera Calibration

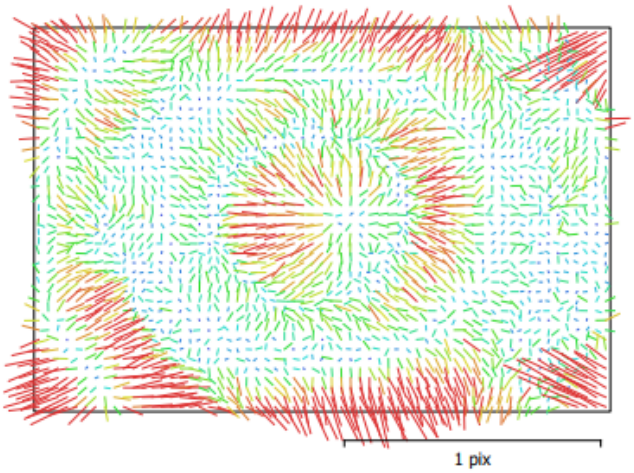

Fig. 2. Image residuals for ZenmuseP1 (35mm).

ZenmuseP1 (35mm)

443 images

Type	Resolution	Focal Length	Pixel Size
Frame	**8192 x 5460**	**35 mm**	**4.39 x 4.39 µm**

	Value	Error	F	Cx	Cy	K1	K2	K3	P1	P2
F	**8199.84**	0.058	1.00	-0.00	-0.80	-0.16	0.13	-0.12	0.04	0.26
Cx	**-29.2817**	0.03		1.00	-0.01	0.01	-0.01	0.01	0.76	-0.01
Cy	**13.6047**	0.053			1.00	0.02	-0.02	0.03	-0.03	0.02
K1	**-0.0493958**	2e-05				1.00	-0.96	0.90	0.02	-0.09
K2	**0.0258002**	0.00013					1.00	-0.98	-0.01	0.02
K3	**-0.113961**	0.00024						1.00	0.01	-0.02
P1	**-0.0011077**	9.6e-07							1.00	0.03
P2	**0.00075211**	1.1e-06								1.00

Table 2. Calibration coefficients and correlation matrix.

Ground Control Points

Fig. 3. GCP locations and error estimates.
Z error is represented by ellipse color. X,Y errors are represented by ellipse shape.
Estimated GCP locations are marked with a dot or crossing.

Count	X error (mm)	Y error (mm)	Z error (mm)	XY error (mm)	Total (mm)
3	5.46721	0.686138	0.914862	5.51009	5.58553

Table 3. Control points RMSE.
X - Easting, Y - Northing, Z - Altitude.

Label	X error (mm)	Y error (mm)	Z error (mm)	Total (mm)	Image (pix)
m3	-7.7059	0.715435	-1.28519	7.84503	0.276 (6)
m2	4.39953	0.209987	0.771657	4.47162	0.283 (12)
m4bis	3.3067	-0.925427	0.513572	3.47195	0.281 (5)
m9					
area.pesa....					
arealegna2					
Total	**5.46721**	**0.686138**	**0.914862**	**5.58553**	**0.281**

Table 4. Control points.

X - Easting, Y - Northing, Z - Altitude.

Digital Elevation Model

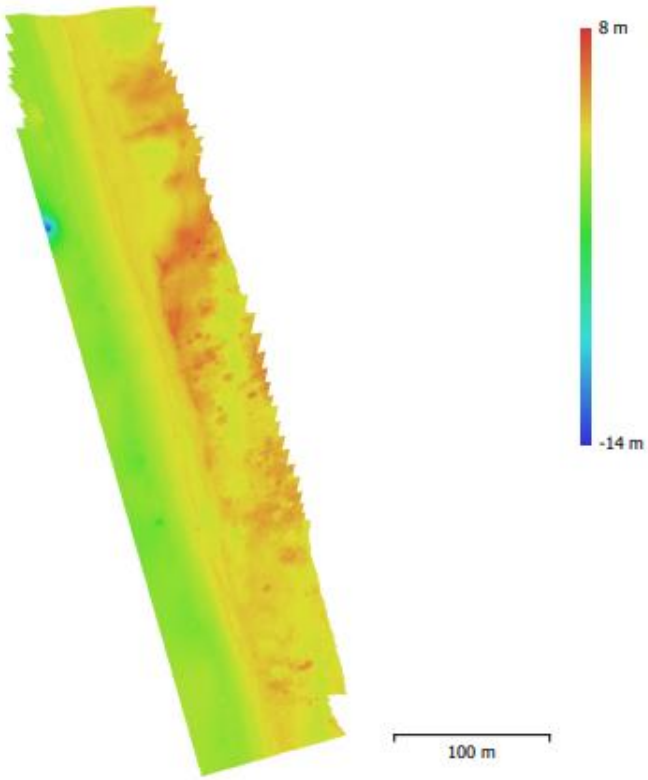

Fig. 4. Reconstructed digital elevation model.

Resolution:	2.89 cm/pix
Point density:	0.12 points/cm²

Processing Parameters

General	
Cameras	443
Aligned cameras	443
Markers	6
Coordinate system	WGS 84 / UTM zone 32N (EPSG::32632)
Rotation angles	Yaw, Pitch, Roll
Point Cloud	
Points	1,683,429 of 1,861,279
RMS reprojection error	0.115459 (1.2828 pix)
Max reprojection error	0.444278 (64.7706 pix)
Mean key point size	8.4567 pix
Point colors	3 bands, uint8
Key points	No
Average tie point multiplicity	4.11966
Alignment parameters	
Accuracy	Medium
Generic preselection	Yes
Reference preselection	Source
Key point limit	0
Tie point limit	0
Exclude stationary tie points	No
Guided image matching	No
Adaptive camera model fitting	No
Matching time	15 minutes 53 seconds
Matching memory usage	1.15 GB
Alignment time	11 minutes 26 seconds
Alignment memory usage	794.00 MB
Optimization parameters	
Parameters	f, cx, cy, k1-k3, p1, p2
Adaptive camera model fitting	No
Optimization time	26 seconds
Date created	2022:07:04 07:50:49
Software version	1.7.2.12070
File size	160.90 MB
Depth Maps	
Count	349
Depth maps generation parameters	
Quality	Medium
Filtering mode	Moderate
Processing time	1 hours 35 minutes
Memory usage	3.31 GB
Date created	2022:07:04 11:37:47
Software version	1.7.2.12070
File size	1.32 GB
Dense Point Cloud	
Points	54,471,604
Point colors	3 bands, uint8
Depth maps generation parameters	
Quality	Medium
Filtering mode	Moderate

Processing time	1 hours 35 minutes
Memory usage	3.31 GB
Dense cloud generation parameters	
Processing time	1 hours 18 minutes
Memory usage	7.23 GB
Date created	2022:07:04 12:56:07
Software version	1.7.2.12070
File size	790.20 MB
DEM	
Size	8,691 x 18,016
Coordinate system	WGS 84 / UTM zone 32N (EPSG::32632)
Reconstruction parameters	
Source data	Dense cloud
Interpolation	Enabled
Processing time	1 minutes 32 seconds
Memory usage	322.22 MB
Date created	2022:07:04 12:57:40
Software version	1.7.2.12070
File size	320.41 MB
Orthomosaic	
Size	30,508 x 68,536
Coordinate system	WGS 84 / UTM zone 32N (EPSG::32632)
Colors	3 bands, uint8
Reconstruction parameters	
Blending mode	Mosaic
Surface	DEM
Enable hole filling	Yes
Enable ghosting filter	No
Processing time	31 minutes 25 seconds
Memory usage	10.66 GB
Date created	2022:07:04 13:18:31
Software version	1.7.2.12070
File size	28.46 GB
System	
Software name	Agisoft Metashape Professional
Software version	1.8.3 build 14331
OS	Windows 64 bit
RAM	31.39 GB
CPU	11th Gen Intel(R) Core(TM) i7-1185G7 @ 3.00GHz
GPU(s)	None

II. List of Acronyms

ARPAT Agenzia Regionale per la Protezione Ambientale Toscana
CO_2 Carbon Dioxide
CSF Cloth Simulation Filter
CWD Coarse Woody Debris
DEM Digital Elevation Model
DSM Digital Surface Model
DTM Digital Terrain Model
GEE Google Earth Engine
GHGs Green House Gasses
GIS Geographical Information System
GNSS Global Navigation Satellite System
GPS Global Positioning System
GCPs Ground Control Points
GSD Ground Sampling Distance
GWP Global Warming Potential
IMU Inertial Measurement Unit
IPCC Intergovernmental Panel on Climate Change
ISPRA Istituto Superiore per la Protezione e la Ricerca Ambientale
LiDAR Light Detection and Ranging
LWD Large Woody Debris
NET Negative Emission Technologies
NFI National Forest Inventories
NRTK Network Real Time Kinematic
RGB Red Green Blue
RTK Real Time Kinematics
SfM Structure for Motion
SVM Support Vector Machine
UASs Uncrewed Aerial Systems
UNFCCC United Nations Framework Convention on Climate Change
UTM Universal Transverse Mercator

III. List of Tables

IV. List of Figures